ABSTRACT

Title of Dissertation:	DYNAMICS AND APPLICATIONS OF LONG-DISTANCE LASER FILAMENTATION IN AIR
	Andrew Goffin, Doctor of Philosophy, 2024
Dissertation directed by:	Professor Howard Milchberg, Department of Electrical and Computer Engineering

Femtosecond laser pulses with sufficient power will form long, narrow high-intensity light channels in a propagation medium. These structures, called “filaments”, form due to nonlinear self-focusing collapse in a runaway process that is arrested by a mechanism that limits the peak intensity. For near-infrared pulses in air, the arrest mechanism is photoionization of air molecules and the resulting plasma-induced defocusing. The interplay between plasma-induced defocusing and nonlinear self-focusing enables high-intensity filament propagation over long distances in air, much longer than the Rayleigh range (~4 cm) corresponding to the ~200 μm diameter filament core.

In this thesis, the physics of atmospheric filaments is studied in detail along with several applications. Among the topics of this thesis: (1) Using experiments and simulations, we studied the pulse duration dependence of filament length and energy deposition in the atmosphere, revealing characteristic axial oscillations intimately connected to the delayed rotational response of air molecules. This measurement used a microphone array to record long segments of the

filament propagation path in a single shot. These results have immediate application to the efficient generation of long air waveguides. (2) We investigated the long-advertised ability of filaments to clear fog by measuring the dynamics of single water droplets in controlled locations near a filament. We found that despite claims in the literature that droplets are cleared by filament-induced acoustic waves, they are primarily cleared through optical shattering. (3) We demonstrated optical guiding in the longest-filament induced air waveguides to date (~50 m, a length increase of ~60×) using multi-filamentation of Laguerre-Gaussian LG_{01} modes with pulse durations informed by experiment *(1)*. (4) We demonstrated the first continuously operating air waveguide, using a high-repetition-rate laser to replenish the waveguide faster than it could thermally dissipate. For each of the air waveguide experiments, extension to much longer ranges and steady state operation is discussed.

DYNAMICS AND APPLICATIONS OF LONG-DISTANCE LASER FILAMENTATION IN AIR

by

Andrew Goffin

Dissertation submitted to the Faculty of the Graduate School of the
University of Maryland, College Park, in partial fulfillment
of the requirements for the degree of
Doctor of Philosophy
2024

Advisory Committee:
Professor Howard Milchberg, Chair
Professor Phillip Sprangle
Professor Ki-Yong Kim
Professor Julius Goldhar
Dr. Eric Rosenthal

Dedication

To Aimee

"It is good to have an end to journey toward; but it is the journey that matters, in the end." - Ursula K. LeGuin, *The Left Hand of Darkness*

Acknowledgements

Many thanks are necessary to everyone who helped me in the completion of my Ph.D. The first, and most obvious, goes to my advisor Professor Howard Milchberg, who spent a lot of time working with me and helping me grow as a researcher. Despite getting my degree in engineering, I feel a lot more like a physicist nowadays, and I thank the environment and education he fostered while I was a member of the group. Overall, I'd say it's gone well!

Additional thanks go out to the many students and post-docs in Howard's lab who have helped me with tough (and not-so-tough) problems over the last several years. Dr. Ilia Larkin was a fantastic mentor and is an excellent experimentalist who taught me a lot early in my graduate career. Without him many of the projects outlined in this dissertation would simply have not happened. Drs. Linus Feder, Bo Miao, Sina Zahedpour, and Daniel Woodbury were all also helpful mentors for variety of projects I've been able to work on during my time here. My fellow Small Lab researchers Lucas Railing and Manh Le provided steady hands and lots of time on the Legend when needed! Additionally, the other undergraduate and graduate students who worked on these projects with me with these projects, Jesse Griff-McMahon, Andrew Tartaro, and Gregory Babiç, were quick learners who were essential to finishing these projects. Jesse developed large portions of YAPPE, which ended up being my bread-and-butter for a large portion of this work. Special thanks also go out to Dr. Scott Hancock, who helped me a ton with my research and led a lot of interesting projects in his own right while also being a good friend outside of the lab. And of course, every other graduate student and post-doc in the lab should not go unnoticed, as they all contributed to this thesis in

some way: Dr. Anthony Zingale, Dr. Fatholah Salehi, Dr. Jaron Shrock, Stefan Waczynski, Ela Rockafellow, Nishchal Tripathi, Frederica Liu, and Ari Sloss.

Of course, I would be remiss to not thank my family for their support through this process and, of course, my entire life. I wouldn't be completing this degree without all that you have done for me. The WINGS crew often gave me something to look forward to going back to New Jersey and have been a group I could lean on for well over a decade now. The Graduate Labor Union (formerly Fearless Student Employees) gave me spiritual fulfillment both by fighting the good fight and by sharing good times at Town Hall. And final thanks to my lovely fiancée Dr. Aimee Malzahn, who I cannot say enough about, and is easily the most intelligent and compassionate person that I know.

Table of Contents

List of Figures

List of Abbreviations

TEM – Transverse Electromagnetic

LG – Laguerre-Gaussian

DC – Direct Current

GRIN – Gradient Index

SPM – Self-Phase Modulation

FWHM – Full Width Half Maximum

O_2 – Molecular Oxygen

N_2 – Molecular Nitrogen

OFI – Optical Field Ionization

MPI – Multi-Photon Ionization

NIR – Near Infrared

ADK – Ammosov-Delone-Krainov (ionization)

MIR – Mid Infrared

LWIR – Long Wave Infrared

STOV – Spatiotemporal Optical Vortex

RF – Radio Frequency

LIBS – Laser-Induced Breakdown Spectroscopy

UPPE – Unidirectional Pulse Propagation Equation

NLSE – Nonlinear Schrödinger Equation

SVEA – Slowly Varying Envelope Approximation

CW – Continuous Wave

CMOS – Complementary Metal Oxide Semiconductor

BPM – Beam Propagation Method

YAPPE – Yet Another Pulse Propagation Effort

SHG – Second Harmonic Generation

Chapter 1 Introduction

1.1 Motivation

As the fields of free-space optics and laser directed energy have grown, so has the desire for improved laser transmission through the atmosphere. In realistic atmospheric conditions, the presence of aerosols and turbulence will distort and scatter a beam. In addition, diffraction spreads the beam as it propagates, substantially decreasing signal strength with distance. As such, it is desirable to clear aerosols and confine light with high transmission efficiency, while allowing temporal gating of laser light if necessary. For such applications, high-energy laser pulses are appealing, as lasers are precisely timed and positioned, and their high-energy can induce air density variations through optical absorption heating the air to clear aerosols and confine light.

However, high-energy laser propagation is itself limited by effects such as diffraction, turbulence, aerosol scattering, and dispersion. Each of these effects limit how long it is possible to propagate high intensities and, therefore, over what distance air heating is possible. To accomplish long-distance air heating, linear optics is not sufficient. Nonlinear optical effects, particularly nonlinear self-focusing, permit laser-induced atmospheric manipulation over long distances that would otherwise be impossible. By utilizing these nonlinear effects with high-peak-power pulses and the resulting process of filamentation, we can generate long-distance high-intensity structures with much lower average power. Filaments also access much more efficient mechanisms of depositing energy than linear

absorption, causing higher air temperatures than would otherwise be possible without nonlinear effects. These concepts are the basis of the work in this thesis.

1.2 Linear & Nonlinear Optics

1.2.1 Maxwell's Equations and Material Response

Electromagnetic fields in media are described by Maxwell's equations [1]:

$$\vec{\nabla} \cdot \vec{D} = 4\pi\rho_f \tag{1.1a}$$

$$\vec{\nabla} \cdot \vec{B} = 0 \tag{1.1b}$$

$$\vec{\nabla} \times \vec{E} = -\frac{1}{c}\frac{\partial \vec{B}}{\partial t} \tag{1.1c}$$

$$\vec{\nabla} \times \vec{H} = \frac{1}{c}\left(4\pi\vec{J_f} + \frac{\partial \vec{D}}{\partial t}\right) \tag{1.1d}$$

In Eqs. (1.1a-d), the electric field $\vec{E}$ and displacement field $\vec{D}$ are related through the constitutive relation $\vec{D} = \vec{E} + 4\pi\vec{P}$ with bound charge density $\vec{P}$. Similarly, the magnetic flux density $\vec{B}$ and magnetic field $\vec{H}$ are related through the constitutive relation $\vec{B} = \vec{H} + 4\pi\vec{M}$ with bound current density $\vec{M}$. The free charge density and free current density are denoted by ρ_f and $\vec{J_f}$, respectively, and $c = 2.998 \times 10^{10}$ cm/s is the vacuum speed of light.

In a non-magnetic dielectric material, $\rho_f = 0$, $\vec{J_f} = 0$, and $\vec{B} = \vec{H}$. With these conditions, Maxwell's equations can be combined to form a modified wave equation dependent on $\vec{E}$ and $\vec{P}$:

$$\vec{\nabla}^2\vec{E} + 4\pi\vec{\nabla}\left(\vec{\nabla} \cdot \vec{P}\right) = \frac{1}{c^2}\left(\frac{\partial^2 \vec{E}}{\partial t^2} + 4\pi\frac{\partial^2 \vec{P}}{\partial t^2}\right) \tag{1.2}$$

In vacuum, $\vec{P} = 0$, and Eq. (1.2) produces the wave equation for an electromagnetic wave traveling at speed of light c. In a linear, isotropic, nondispersive material, $\vec{P} = \chi\vec{E}$ with a constant susceptibility χ, which leads to the following equation:

$$\vec{\nabla}^2\vec{E} = \frac{1 + 4\pi\chi}{c^2}\frac{\partial^2\vec{E}}{\partial t^2} = \frac{n^2}{c^2}\frac{\partial^2\vec{E}}{\partial t^2} \tag{1.3}$$

Where $n = \sqrt{1 + 4\pi\chi}$ is the index of refraction of the medium. The velocity of an electromagnetic wave propagating through a dielectric is slowed by the refractive index, now traveling at speed c/n. In the case of a dispersive material, the susceptibility is the electronic impulse response of the medium $\chi(t)$ such that $\vec{P}(t) = \int_{-\infty}^{t}\chi(\tau)\vec{E}(t-\tau)d\tau$. For this analysis, it is simplest to take the Fourier transform of both sides of Eq. (1.2) and use the convolution property of the Fourier transform to get:

$$\vec{\nabla}^2\hat{E} = -\frac{\omega^2}{c^2}\big(1 + 4\pi\hat{\chi}(\omega)\big)\hat{E} \tag{1.4}$$

Where $\hat{E}(\vec{r},\omega) = \mathcal{F}\{\vec{E}(\vec{r},t)\}$ and $\hat{\chi}(\omega) = \mathcal{F}\{\chi(t)\}$. By comparison with the Fourier Transform of Eq. (1.3), Eq. (1.4) shows a frequency-dependent index of refraction, $n(\omega) = \sqrt{1 + 4\pi\hat{\chi}(\omega)}$, which relates to the Fourier transform of the material's dielectric impulse response $\chi(t)$.

If a material is anisotropic (but linear and non-dispersive), the susceptibility becomes a second-order tensor: $\vec{P} = \bar{\bar{\chi}}\cdot\vec{E}$. This by itself does not substantially

simplify Eq. (1.2), but if we assume a uniaxial material where $\bar{\bar{\chi}} = \begin{pmatrix} \chi_o & 0 & 0 \\ 0 & \chi_o & 0 \\ 0 & 0 & \chi_e \end{pmatrix}$, then we get a wave equation for each vector component of $\vec{E}$:

$$\vec{\nabla}^2 E_x = \frac{1 + 4\pi\chi_o}{c^2} \frac{\partial^2 E_x}{\partial t^2} \tag{1.6a}$$

$$\vec{\nabla}^2 E_y = \frac{1 + 4\pi\chi_o}{c^2} \frac{\partial^2 E_y}{\partial t^2} \tag{1.6b}$$

$$\vec{\nabla}^2 E_z = \frac{1 + 4\pi\chi_e}{c^2} \frac{\partial^2 E_z}{\partial t^2} \tag{1.6c}$$

Eqs. (1.6a-c) give two unique refractive indices depending on the electric field polarization; the "ordinary" index $n_o = \sqrt{1 + 4\pi\chi_o}$ and "extraordinary" index $n_e = \sqrt{1 + 4\pi\chi_e}$, each with unique phase velocities c/n_o and c/n_e, respectively. Because different polarizations experience different refractive indices, anisotropic materials exhibit birefringence, which is the refractive splitting of different electromagnetic polarizations. Birefringent effects are used to control laser polarization with wave plates, modulate laser phase with spatial light modulators [2], and efficiently generate different wavelengths of light through phase matching in nonlinear optical media [3].

1.2.2 The Paraxial Equation and Free-Space Modes

In vacuum, we can take the Fourier transform of both sides of Eq. (1.2) and write the Helmholtz equation:

$$\vec{\nabla}^2 \hat{E} = -\frac{\omega^2}{c^2} \hat{E} = -k^2 \hat{E} \tag{1.7}$$

Where $k = \omega/c$ is the electromagnetic wave's wavenumber. We introduce an auxiliary field $\hat{A}$ such that $\hat{E}(x,y,z) = \hat{A}(x,y,z)e^{ikz}$ and rewrite Eq. (1.7) using $\vec{\nabla}^2 = \vec{\nabla}_\perp{}^2 + \frac{\partial^2}{\partial z^2}$:

$$\vec{\nabla}_\perp{}^2 \hat{A} + 2ik\frac{\partial \hat{A}}{\partial z} + \frac{\partial^2 \hat{A}}{\partial z^2} = 0 \tag{1.8}$$

The paraxial approximation assumes that $\hat{A}$ varies slowly in z relative to the wavelength of the wave $\lambda = 2\pi/k$, mathematically stated as $\left|k\frac{\partial \hat{A}}{\partial z}\right| \gg \left|\frac{\partial^2 \hat{A}}{\partial z^2}\right|$. In such a case, we get the paraxial Helmholtz equation:

$$\vec{\nabla}_\perp{}^2 \hat{A} + 2ik\frac{\partial \hat{A}}{\partial z} = 0 \tag{1.9}$$

Eq. (1.9) has many classes of solutions depending on the coordinate basis. In cartesian coordinates, $\vec{\nabla}_\perp{}^2 = \frac{\partial^2}{\partial x^2} + \frac{\partial^2}{\partial y^2}$, and the solutions are *Hermite-Gaussian* modes (denoted TEM_{mn}) [4]:

$$\hat{A}_{mn}(x,y,z) = \frac{w_0}{w(z)} H_m\left(\frac{\sqrt{2}x}{w(z)}\right) H_n\left(\frac{\sqrt{2}y}{w(z)}\right) e^{-\frac{x^2+y^2}{w^2(z)}} e^{-\frac{ik(x^2+y^2)}{2R(z)}} e^{i\psi(z)} \tag{1.10}$$

In Eq (1.10), w_0 is the waist at $z = 0$, H_m is the m^{th} order Hermite polynomial, $\psi(z) = (m+n+1)\arctan(z/z_R)$ is the Gouy phase, and $w(z) = w_0\sqrt{1+(z/z_R)^2}$ and $R(z) = z(1+z_R^2/z^2)$ are the z -dependent beam waist and phase radius of curvature, respectively. The Rayleigh length of a beam is $z_R = \pi w_0^2/\lambda$, which corresponds to the distance where a $(m,n) = (0,0)$ Hermite-Gaussian mode becomes is $\sqrt{2}\times$ larger in diameter. This $(m,n) = (0,0)$ Hermite-Gaussian mode is the famous Gaussian mode:

$$\hat{A}_{00}(x,y,z) = \frac{w_0}{w(z)} e^{-\frac{x^2+y^2}{w^2(z)}} e^{-\frac{ik(x^2+y^2)}{2R(z)}} e^{i\arctan\left(\frac{z}{z_R}\right)} \tag{1.11}$$

Hermite-Gaussian modes in general are electric field maxima (or "lobes") separated by π phase discontinuities, with m maxima in the x dimension and n maxima in the y dimension.

In cylindrical coordinates, $\vec{\nabla}_\perp{}^2 = \frac{\partial^2}{\partial r^2} + \frac{1}{r}\frac{\partial}{\partial r} + \frac{1}{r^2}\frac{\partial^2}{\partial \phi^2}$, which leads to a different set of solutions called *Laguerre-Gaussian* (denoted LG_{pl}) modes [4]:

$$\hat{A}_{pl}(r,\phi,z) = \frac{1}{w(z)}\left(\frac{\sqrt{2}r}{w(z)}\right)^{|l|} L_p^{|l|}\left(\frac{\sqrt{2}r}{w(z)}\right) e^{-\frac{r^2}{w^2(z)}} e^{-\frac{ikr^2}{2R(z)}} e^{il\phi} e^{i\psi(z)} \tag{1.12}$$

When $(p, l) = (0,0)$ this is also a Gaussian mode. $L_p^{|l|}$ is the generalized Laguerre polynomial and $\psi(z) = (|l| + 2p + 1)\arctan\left(\frac{z}{z_R}\right)$ is the Gouy phase. Laguerre-Gaussian modes are notable when $l \neq 0$ as they carry orbital angular momentum [5] and have an on-axis null, each due to the associated phase vortex $e^{il\phi}$. This feature provides Laguerre-Gaussian modes with their characteristic "donut" shape, which proves to be exceptionally useful in air waveguide generation later in this thesis, particularly Chapter 4.

1.2.3 Kerr Self-Focusing

In Eq (1.3), it was assumed that the material polarization $\vec{P}$ is linear in the electric field $\vec{E}$ by a scale factor called the material's susceptibility χ: $\vec{P} = \chi\vec{E}$. In nonlinear media, however, $\vec{P}$ can be any arbitrary function of $\vec{E}$, which can be written as an infinite-order polynomial through Taylor's Theorem [6]. The general

polynomial form of $P(E)$, assuming linear polarization and an isotropic, non-dispersive, medium, is as follows:

$$P(E) = \sum_{n=1}^{\infty} \chi^{(n)} E^n \tag{1.13}$$

In this series, $\chi^{(n)}$ is the nth order susceptibility, generalizing from the linear (or first order) susceptibility of linear optics. In Eq (1.13), $\chi^{(1)}$ is the linear susceptibility χ, and we treat $\vec{E}$ as a scalar field E due to its linear polarization and the symmetry of the medium. Typically, the dominant nonlinear terms are the lowest-order terms, in particular $\chi^{(2)}$ and $\chi^{(3)}$. The second-order nonlinearity itself has numerous applications. For example, the propagation of a time-harmonic electric field through a $\chi^{(2)}$ medium causes second harmonic generation. Also, birefringence can be induced in a $\chi^{(2)}$ medium using a DC field through a phenomenon known as the Pockels Effect, allowing electronic polarization control of a time-harmonic field [6].

Air is a centrosymmetric medium, so $\chi^{(2)} = 0$ and $\chi^{(3)}$ is the dominant nonlinear term. Assuming that the electric field is time-harmonic with angular frequency ω, it can be written as $E(t) = \frac{1}{2}E_0(e^{i\omega t} + e^{-i\omega t})$. If we use this form of the field with the third-order nonlinearity (assuming an isotropic medium and linear polarization), we get the following equation for $P^{(3)}$, the third-order polarization:

$$P^{(3)} = \frac{1}{8}\chi^{(3)}E_0^3\left(e^{i\omega t} + e^{-i\omega t}\right)^3 \tag{1.14}$$

$$P^{(3)} = \frac{1}{4}\chi^{(3)}E_0^3(3\cos(\omega t) + \cos(3\omega t)) \tag{1.15}$$

Note that there are two terms here: the first at frequency ω and the second at the frequency 3ω. The second term corresponds to third-harmonic generation, where the third-order nonlinear effect generates an electric field at frequency 3ω. The first term is often called the "self-phase modulation" or "Kerr self-focusing" term, where the third-order nonlinearity generates additional bound charge density at frequency ω. We are only interested in Kerr self-focusing for this section, so let us ignore the third harmonic generation and add in the $\chi^{(1)}$ polarization term.

$$P = \left(\chi^{(1)} + \frac{3}{4}\chi^{(3)}E_0^2\right)E_0\cos(\omega t) \tag{1.16}$$

The expression in parentheses is an effective susceptibility χ_{eff}, which is a function of the electric field amplitude E_0. We can use χ_{eff}, the fact that in air $\frac{3}{4}\chi^{(3)}E_0^2 \ll \chi^{(1)}$, and the definition of the index of refraction n, to do the following calculation:

$$n = \sqrt{1 + 4\pi\chi_{eff}} \tag{1.17}$$

$$n = \sqrt{1 + 4\pi\chi^{(1)} + 4\pi\frac{3}{4}\chi^{(3)}E_0^2} \tag{1.18}$$

$$n \cong \sqrt{1 + 4\pi\chi^{(1)}} + 4\pi\frac{3}{8\sqrt{1 + 4\pi\chi^{(1)}}}\chi^{(3)}E_0^2 \tag{1.19}$$

Now, let us take $n_0 = \sqrt{1 + 4\pi\chi^{(1)}}$ to be the linear index of refraction and rewrite the electric field in terms of optical intensity $I = \frac{cn_0}{8\pi}E_0^2$:

$$n = n_0 + \frac{12\pi^2}{n_0^2 c}\chi^{(3)}I \tag{1.20}$$

We therefore define the nonlinear index of refraction n_2:

$$n_2 = \frac{12\pi^2}{n_0^2 c}\chi^{(3)} \tag{1.21}$$

In a $\chi^{(3)}$ medium there is an intensity-dependent index of refraction, where the nonlinear index n_2 determines the strength of the intensity dependence.

The presence of an intensity-dependent index causes Kerr self-focusing. This effect is like that caused by a gradient index (or GRIN) lens, where the GRIN lens focuses a beam by increasing the index of refraction radially inwards as opposed to using a curved glass surface. A gaussian beam is more intense in the center than the outside of the beam, which due to the nonlinear index of refraction leads to a similar transverse index gradient with a higher index in the center and lower index towards the outside. Just like the GRIN lens, this causes the beam to focus. However, instead of the beam collapsing to a geometrically determined focal plane, the beam focuses either until its size is so small that diffraction prevents further focusing or until another defocusing effect arrests collapse and creates a filament, as will be discussed in Sec. 1.3.

1.2.4 Self-Phase Modulation and Supercontinuum

Because the index of refraction in a $\chi^{(3)}$ medium is a function of intensity, and laser pulses vary intensity with time, the index in a $\chi^{(3)}$ medium will also vary with time. Since the laser pulse generates the index shift to modulate its own phase, this phenomenon is called "self-phase modulation" or SPM. SPM causes spectral broadening:

$$\phi(t,z) = k_0 \int \Delta n dz - \omega_0 t = k_0 n_2 \int I(t,z) dz - \omega_0 t \tag{1.22}$$

$$-\frac{\partial \phi}{\partial t} = -k_0 n_2 \int \frac{\partial I}{\partial t} dz + \omega_0 = \omega(t,z) \tag{1.23}$$

Eq (1.23) shows that new frequencies are generated around the central frequency ω_0 due to the temporally varying intensity $I(t)$. Frequencies further from ω_0 are generated over the course of propagation as the effect accumulates through the integral in the first term. This accumulation of spectral broadening is a key feature of propagation through $\chi^{(3)}$ media, and the resulting spectrum is called a "supercontinuum". As such, Kerr media are often used to generate broad spectra [7] and, using these spectra, extremely short pulses [8]. However, to output a shorter pulse one must compensate for the chirp that occurs during supercontinuum generation, which is shown in Eq (1.23) as a temporally dependent frequency. Fig. 1.1(a) plots calculated spectral broadening in air at a fixed intensity of $I = 10$ TW/cm^2 at several different locations, not including other propagation effects (such as self-focusing, dispersion, etc.). Over 75 cm of propagation the pulse bandwidth increases from 35 nm to ~90 nm. Fig. 1.1(b) plots the transform-limited pulse for a given spectrum at each propagation location, showing that the generated supercontinuum can be compressed into much shorter pulses, down from 50 fs to ~13fs. Without dispersion compensation, however, these pulses will remain 50 fs FWHM, but with a broader spectrum and substantial chirp from SPM.

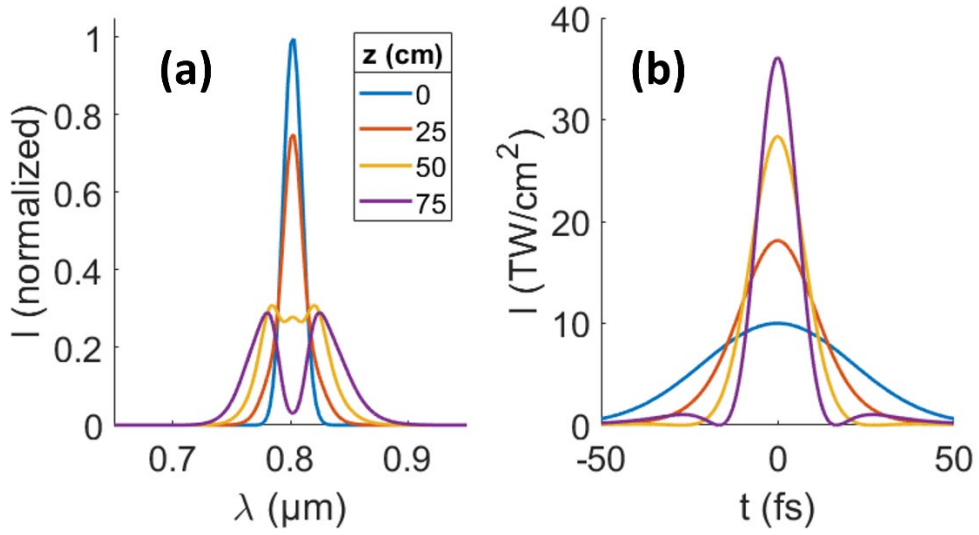

Figure 1.1 (a) Spectral broadening during propagation in air, only accounting for phase accumulation from SPM, starting with central wavelength 800 nm and FWHM bandwidth 35 nm. **(b)** Transform limited pulse at each z location.

1.2.5 Delayed rotational self-focusing

For ultrashort pulses in air, the excitation of molecular rotations in N_2 and O_2 is a second source of self-focusing. When a laser pulse interacts with these molecules, it induces a dipole moment $\vec{p}$ in the molecules which then experience a torque ($\sim\vec{p}\times\vec{E}$) towards laser polarization alignment. In a quantum mechanical framework, this is modelled as the excitation of a superposition of higher-energy molecular rotational states which, on average, are better aligned with laser polarization. This set of rotational states have a higher effective refractive index than the initial, thermal, distribution of states due to the higher average alignment with the laser polarization. The equation for effective susceptibility in local time ξ due to rotations is given by [9]:

$$\chi_{rot}(\xi) = N_{N_2}\Delta\alpha_{N_2}\left[\langle\cos^2\theta\rangle_{N_2} - \frac{1}{3}\right] + N_{O_2}\Delta\alpha_{O_2}\left[\langle\cos^2\theta\rangle_{O_2} - \frac{1}{3}\right] \qquad (1.24)$$

Where $\langle \cos^2 \theta \rangle_X$ is the average alignment of molecular species X in the current distribution of rotational states, $\Delta\alpha_X$ is the molecular anisotropy of species X equaling the difference in polarization between the two molecular axes (for linear molecules like N_2 and O_2), and N_X is the number density of species X. $\langle \cos^2 \theta \rangle_X$ can be calculated from a density matrix formalism of the molecular ensemble which results in Eq (1.25) [9]:

$$\langle \cos^2 \theta \rangle = \frac{1}{3} + \frac{2\Delta\alpha}{15\hbar} \sum_{j=0}^{j_{max}} \frac{j(j-1)}{2j-1} \left(\frac{\rho_{jj}^0}{2j+1} - \frac{\rho_{j-2,j-2}^0}{2j-3} \right) \times \int_{-\infty}^{\xi} sin\{(\omega_j - \omega_{j-2})(\xi' - \xi)\} |E(\xi)|^2 d\xi' \quad (1.25)$$

Where ρ_{jj}^0 corresponds to the initial value of density matrix element ρ_{jj}, $\omega_j = U_j/\hbar$ is the energy of rotational state j, and $E(\xi)$ is the laser electric field in the frame of reference local to the pulse, $\xi = t - z/v_g$ for group velocity v_g. As such, the evolution of molecular alignment depends on the initial distribution of rotational states and the convolution of the electric field with sines corresponding to the rotational energy transitions. A thermal distribution of rotational states will always have an average alignment $\langle \cos^2 \theta \rangle = 1/3$, causing $\chi_{rot} = 0$ as would be expected with no laser field present. Because the rotational response is sinusoidal, and therefore periodic, an electric field impulse will excite a set of rotational states that will periodically realign and lead to another instance of molecular alignment. This alignment revival period, which occurs after roughly 8 ps for N_2, has been used to enhance air absorption of light [10] and enhance or destroy the self-focusing of follow-up filamenting pulses [11,12].

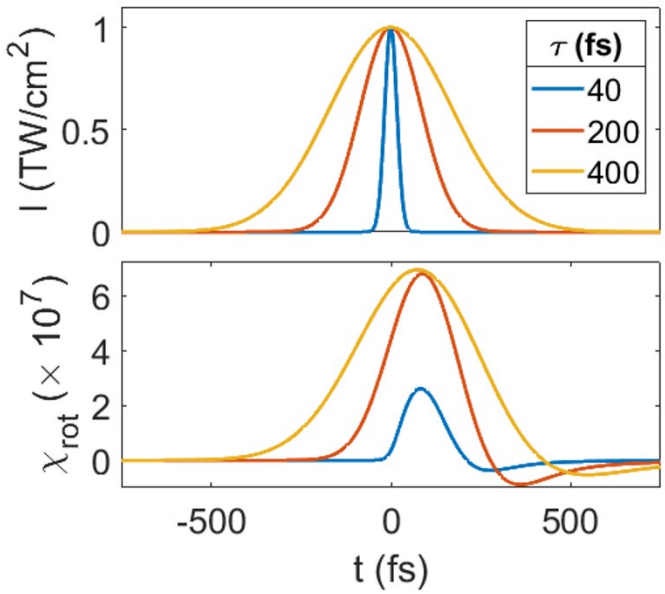

Figure 1.2 *Top:* Gaussian pulses with different FWHM pulse durations τ. *Bottom:* Corresponding rotational susceptibilities $\chi_{rot}(t)$ for each pulse duration.

Due to the molecules' rotational inertia, molecular alignment is not instantaneous; the characteristic time scale for molecular alignment is ~100 fs for air temperatures ~300 K. For this reason, while the Kerr (or electronic) self-focusing effect is instantaneous on femtosecond pulse time scales, rotational self-focusing is delayed, which manifests as the convolution integral in Eq (1.25). This means that pulses much shorter than 100 fs experience very little additional self-focusing from molecular rotations and, by contrast, pulses much longer than 100 fs experience molecular self-focusing near-instantaneously on the pulse time scale. Fig. 1.2 shows this effect by plotting the pulse intensities in a figure above their corresponding rotational susceptibilities $\chi_{rot}(t)$. At $\tau = 40$ fs FWHM, χ_{rot} is substantially delayed and does not overlap strongly with the pulse in question,

whereas at $\tau = 400$ fs the overlap with χ_{rot} is high and χ_{rot} itself reaches a higher peak due to the higher pulse fluence driving stronger alignment. This phenomenon leads to a pulse-duration-dependent self-focusing effect where longer pulses experience stronger self-focusing than shorter pulses.

1.2.6 Plasma Defocusing and Ionization

At high intensities in air, laser pulses will generate plasma by freeing electrons from neutral air constituents. This plasma then refracts the laser pulse after forming due to the free electron response to the laser field. The index of refraction for low-temperature plasmas can be written as follows:

$$n = \sqrt{1 - \frac{\omega_p^2}{\omega^2}} \tag{1.26}$$

Where the plasma frequency is $\omega_p = \sqrt{4\pi N_e e^2/m_e}$, plasma electron density is N_e, and optical frequency is ω. Since $n < 1$ for any physical value for N_e, the plasma creates a lower index of refraction at the center, high-intensity, portion of the beam than at the periphery where there are almost no free electrons. This creates a defocusing effect, opposite of Kerr and rotational self-focusing.

Laser pulses primarily generate electrons through two mechanisms: (1) optical field ionization (or OFI) and (2) avalanche ionization. OFI can be described with two limiting cases of multi photon ionization (or MPI) [13] and tunneling ionization. MPI occurs when the energy of multiple photons surpasses the bound electron energy with an electric field too weak to substantially perturb the bound electron potential, illustrated in the left panel of Fig. (1.3a). By contrast, tunneling ionization occurs when the electric field sufficiently perturbs the bound electron

potential to cause a high probability of the electron tunneling through the potential well, shown in the right panel of Fig. (1.3a). The transition between these two limiting cases occurs when the Keldysh parameter, $\gamma = \frac{\omega}{E}\sqrt{2U_I}$, equals one [13]. For low Keldysh parameters, the electric field E is high relative to the ionization energy U_I and photon energy ω, and therefore the bound electron potential is substantially perturbed and tunneling ionization occurs. For high Keldysh parameters, E is low relative to U_I and ω, which leads to MPI since the potential well remains relatively undisturbed. In the case of NIR atmospheric filaments, $\gamma \sim 1-2$, so neither limiting case is appropriate. Instead, a "strong field" model can be used [14], which is valid across all Keldysh parameters. In cases where $\gamma \leq 0.5$, ADK ionization, a generalization of tunneling ionization, is also an appropriate model [15].

Fig. (1.3b) shows the difference in ionization rates for MPI, ADK, and strong field ionization. Strong field ionization approaches ADK at low Keldysh parameters, $\gamma < 1$, as tunneling ionization becomes the dominant effect. At high Keldysh parameters, ADK severely underestimates the ionization rate, while strong field ionization tracks MPI, albeit with some deviation. This illustrates the transition between MPI and tunneling ionization and demonstrates how strong field ionization can be well-applied in both regimes.

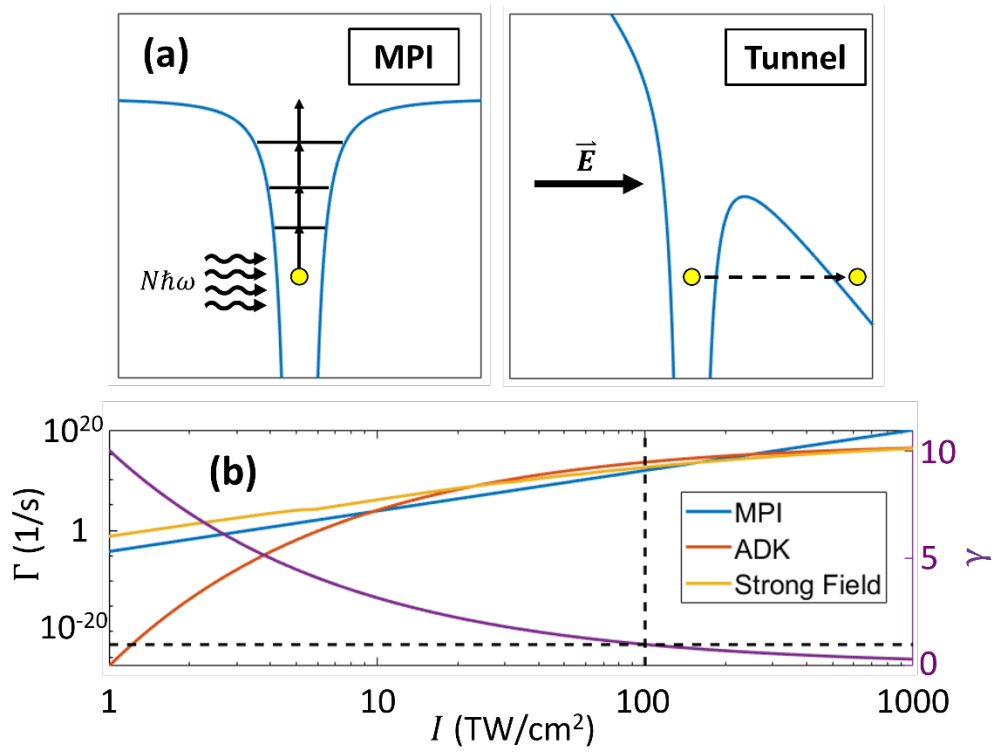

Figure 1.3 (a) Illustration of MPI (left) and tunneling ionization (right) **(b)** MPI, ADK, and strong field ionization rates for different intensities in O_2 at $\lambda_0 = 800$ nm. The purple curve plots the Keldysh parameter γ for each intensity, with the black dashed lines marking $\gamma = 1$.

Avalanche (or collisional) ionization occurs when existing free electrons are accelerated by the laser pulse and collide with neutral species, freeing bound electrons. The collisional ionization rate depends on the electron-neutral collision rate and free electron kinetic energy. When electrons are freed via OFI into a cold plasma, the free electron kinetic energy is mostly determined by the ponderomotive energy from the laser, which is the maximum kinetic energy an electron has over the course of a laser oscillation. The ponderomotive energy, $U_P = \left(\frac{e^2\lambda_0^2}{16\pi^2 c m_e}\right) E^2$, is dependent on the laser central wavelength λ_0 and electric field amplitude E. Since U_P is higher for longer wavelengths, avalanche ionization tends to be prominent at

MIR and LWIR wavelengths [16]. However, picosecond NIR pulses can also generate substantial avalanche despite their relatively low ponderomotive energy [17] due to having a high intensity longer than the electron-neutral collision timescale (~0.5 ps in 1 atm air) [18,19]. For this reason, avalanche ionization can be a relevant mechanism for NIR-pulse-generated plasma electron densities for long enough pulses.

1.3 Filamentation

For high laser peak powers, $P \sim U/\tau$ with laser energy U and pulse duration τ, self-focusing is stronger than diffraction at all points as the pulse focuses. This leads to pulse collapse until the onset of *collapse arrest*, where a physical mechanism causes additional defocusing to offset the runaway self-focusing. The power necessary for runaway self-focusing and collapse arrest is called the critical power P_{crit} (sometimes denoted P_{cr}). In the case of NIR femtosecond pulses, and in most other regimes, the collapse arrest mechanism is OFI-induced plasma defocusing. However, there are unique regimes where collapse may be arrested by different mechanisms such as carrier shock formation and third-harmonic walkoff for femtosecond MIR and LWIR pulses [20,21] or group velocity dispersion in dispersive media [22]. The collapse-arrest-induced defocusing and self-focusing effects form a dynamic balance that leads to a long-distance high-intensity optical structure called a *filament*.

The critical power $P_{crit} = \frac{\alpha \lambda_0^2}{8\pi n_0 n_2}$ [23] is related to the central wavelength λ_0, nonlinear index of refraction n_2, linear index of refraction n_0, and a factor α that

depends on the initial beam mode. For a Ti:Sapphire laser Gaussian mode in air, $\alpha = 3.77$, $n_2 \approx 7.94 \times 10^{-20}$cm^2/W [24], $n_0 \approx 1$, and $\lambda_0 = 800$ nm, so $P_{crit} =$ 12 GW. However, in practice, because n_2 only includes the electronic nonlinearity and not the rotational nonlinearity, the power needed to form a filament can be as low as 2-3 GW, depending on the pulse duration [25]. For typical laser pulse energies in the millijoule range, this requires either few-picosecond or femtosecond pulses for filament formation.

At collapse arrest, the filament forms a core-reservoir structure. In the core (diameter $d_{core} \approx 200$ μm at $\lambda_0 = 800$ nm in air), the intensity $I_{core} < 10^{14}$ W/cm^2 is high enough to generate a low-density plasma $N_e \approx 10^{16} - 10^{17}$ cm^{-3} that balances self-focusing in the core. The reservoir surrounding the core is lower intensity and generates essentially no plasma while still self-focusing and feeding energy into the filament core. Energy flow from the reservoir to core is necessary to maintain filament propagation, and destruction or blockage of the reservoir also functionally ends filamentation [26,27]. The core and reservoir are separated by a pair of oppositely-wound ring phase vortices called spatiotemporal optical vortices (or STOVs) created due to the extreme spatiotemporal phase shear between the two regions induced by nonlinear self-focusing and plasma in the filament [26]. Energy flow between the core and reservoir can be described using STOV-induced energy flow, where the STOV phase requires focusing in front of the +1 STOV and behind the -1 STOV, while requiring defocusing between the two STOVs (STOVs labelled in Fig. 1.4) [26]. The reservoir size is proportional to the initial beam size, and since the strength of diffraction depends on the size of a beam, larger beams produce

larger reservoirs which allow longer filaments [28], as demonstrated up to kilometer scale [29,30]. The core-reservoir structure also makes filaments robust against blockages; if the core is blocked off it will be refueled by the reservoir due to the natural energy flow present in a filament in a process called self-healing [31,32]. Filament refocusing cycles are facilitated by the reservoir, where it refills the filament core due to self-focusing after plasma defocusing decreases the core intensity. This refocusing occurs behind the initial filamenting pulse, leading to a pulse splitting phenomenon where there are multiple temporally separated pulses on-axis [33]. Refocusing cycles can also be explained by STOV-induced energy flow between the core and reservoir, as shown in [34]. The refocusing cycle process, core-reservoir structure, and STOV structure are illustrated in Fig. 1.4.

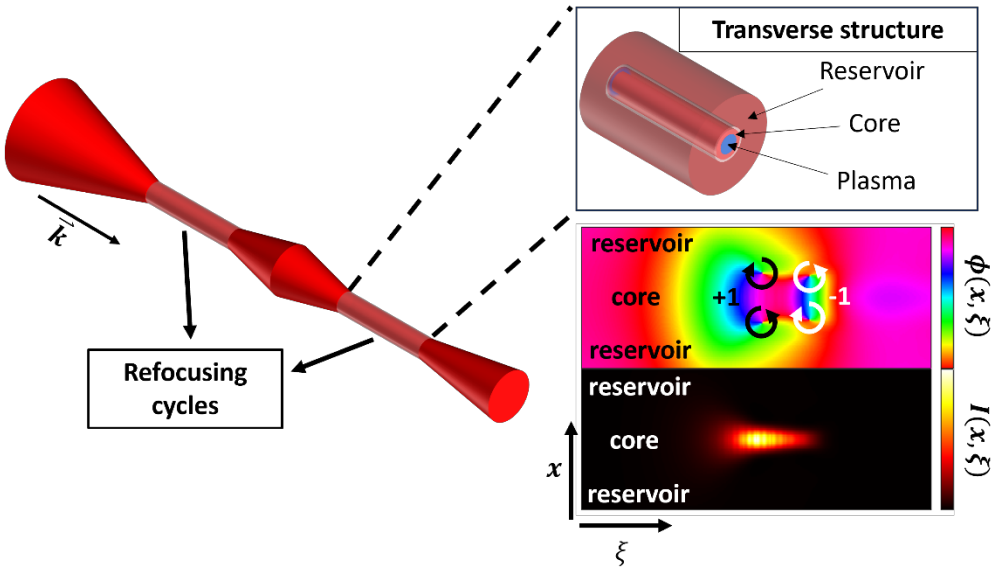

Figure 1.4 *Left:* Illustration of the filamentation. Regions of high ionization are labelled as the "refocusing cycles". The propagation direction is labelled by $\vec{k}$. *Top right:* The core-reservoir transverse structure of the filament is illustrated in the top right section, with the plasma contained in the filament core and the reservoir and core separated by a null (due to STOV

formation [26]). *Bottom right:* Depiction of filament STOVs in the $x - \xi$ plane through the center of the filament. The x axis (transverse space) is vertical and the ξ axis (local time) is horizontal. Each STOV is a ring phase vortex shown as point vortices on either side of the filament core which are connected by a full ring phase discontinuity surrounding the core. The +1 and -1 STOVs each have opposite phase windings at all transverse locations. The ring STOVs in the top phase plot surround the high-intensity core, depicted in the bottom intensity plot.

The extreme optical nonlinearities present during filamentation mean that many nonlinear phenomena can be generated with filaments, including white light (supercontinuum) generation [35], THz and RF generation via the filament plasma [36,37], cavity-free N_2^+ lasing [38–40], laser-induced water condensation [41], and laser-induced breakdown spectroscopy (or LIBS) [42,43].

1.3.1 Filament-Induced Hydrodynamics

As the filament propagates, it deposits energy into the air in its wake. Energy deposition occurs through mechanisms such as OFI, excitation of molecular rotations [9], and inverse Bremsstrahlung heating [44]. This energy is repartitioned after plasma recombination (~10 ns) [45] and molecular rotational decoherence (~100 ps) [46], each much faster than the acoustic timescale of air ($d_{core}/2c_s \approx$ 300 ns, with speed of sound $c_s \approx 300$ m/s). This thermalization instantly heats the air and develops into a pressure spike along the length of the filament [47]. The pressure equilibrates by radially shooting out a single-cycle acoustic wave, leaving behind a long-lasting density depression also called a "density hole". The density hole diffuses over tens of milliseconds until the density and temperature return to ambient levels [47]. Fig. 1.5 shows interferometric data of a laser-induced acoustic wave and density hole from [47], with the color scale representing the index shift experienced by the interferometric probe $\Delta n = 2.77 \times 10^{-4} \Delta N_g / N_{atm}$ for gas

number density shift ΔN_g and atmospheric density $N_{atm} \approx 2.5 \times 10^{19}$ cm^{-3}. The single-cycle acoustic wave is best seen in the 0.2 µs and 0.9 µs panels as a circular index shift that propagates radially around the low-density center. By 60 µs the acoustic wave is no longer in view but the density hole is still present, just larger and shallower than it started due to thermal diffusion. In [47] the filament was strongly lens-assisted, causing a smaller plasma channel with higher electron densities, so the density hole is deeper than a typical collimated filament's while also having a shorter lifetime. This is a trend that holds for all filament applications; lens-assisted filaments are shorter and smaller with higher peak energy deposition, whereas filaments generated by collimated beams are longer with lower peak energy deposition.

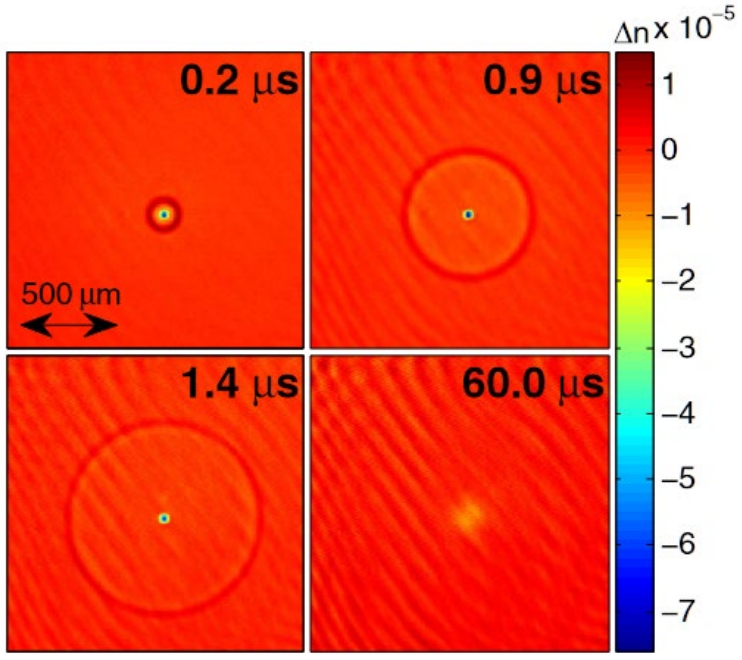

Figure 1.5 Air hydrodynamics after filament heating. The density variations are shown as index shifts Δn experienced by a probe pulse. [47]

Filament-induced heating will produce on-axis temperature spikes around $\Delta T \approx 100$ K upon thermalization (corresponding to an energy deposition per unit length of $\partial_z \mathcal{E}_{dep} \approx 4$ μJ/cm). This rapid, efficient, and long-lasting heating means that filaments can be effectively used for modulating air density and the generation of single-cycle acoustic waves. Filament-induced heating has been used for, or used to explain, applications as varied as guided electrical discharges [48,49], fog clearing [50–52], single-shot acoustic filament measurements [53], and air waveguiding [54–56].

1.3.2 Repetition Rate Effects

Filament-induced density holes persist for millisecond timescales, which for 10 Hz laser systems means that the density holes diffuse to ambient density between laser pulses. However, for faster repetition rates, subsequent laser pulses will propagate through the density depression leftover from the previous pulse before the prior depression can fully diffuse, meaning that the heating from prior pulses will affect the pulses arriving later. This leads to a repetitive heating effect where several pulses can build up to a deeper density hole than is possible from a single laser pulse. Since the density hole never fully diffuses between laser pulses, there is a density depression always present along the filament path with the depth of the depression varying between pulses due to diffusion. Given the millisecond timescale lifetime of density holes, repetition rates >100 Hz are required to observe cumulative effects.

Because there is a temperature gradient present for periods of time longer than thermal timescales of the density hole, at high repetition rates buoyancy causes a

net lower density above the density hole and a net higher density below the density hole [57]. This density gradient causes downward filament deflection for single filaments, which does not occur at low repetition rates [57]. While high-repetition-rate cumulative heating can lead to deeper density holes, which is often desirable, this buoyancy-induced deflection must be accounted for when necessary. Modelling in other work [58] shows that 100 Hz – 200 Hz repetition rates are necessary for buoyant effects for a 2.7 mJ, 100 fs FWHM pulse ($P \sim 6P_{crit}$), below which thermal diffusion will decrease air temperature to near-ambient levels before it can rise due to buoyancy.

1.3.3 Multifilamentation

For beams containing just a few P_{crit}, single filamentation will occur as described earlier in Sec. 1.3. However, if the beam contains very high peak powers $P \gg P_{crit}$, it will undergo a process of multifilamentation where multiple filaments form simultaneously [59,60]. The location of filaments in a multifilamenting beam is seeded by amplitude and phase variations in the beam and is, therefore, seeded by noise in Gaussian beams leading to shot-to-shot variations in filament location. Additionally, the number of filaments will increase as the power in the beam also increases.

Since filament location in a multifilamenting beam is dependent on the initial beam profile, different modes will seed multifilaments differently. For example, a Gaussian beam will tend to have more filaments towards the center of the beam but will largely be seeded by noise [61,62]. In a plane wave, the wavenumber of maximal growth is $k_{\perp} = 2\sqrt{\pi I/P_{crit}}$ [61,62], giving an average distance between

filaments of $\sim\sqrt{P_{crit}/\pi I}$. Thus, as the number of filaments (related to P/P_{crit}) goes up, the filaments also bunch up near the center of a Gaussian beam. If a Gaussian beam goes through an amplitude mask, filament locations will be regularized, but their length will be limited by diffraction through the mask [63]. Filaments can also be separated by phase, which can be used to decrease diffractive effects limiting filament length. A Hermite-Gaussian mode will generate one filament in each lobe of the beam before generating more in each lobe at much higher powers [54,64]. A Laguerre-Gaussian mode, with a spiral phase vortex, will seed filaments in the highest-intensity part of the ring. This process guarantees a ring filament structure, as shown in Fig. 1.6 and in [65,66]. The exact dynamics of LG multifilamentation are essential for air waveguiding and are discussed in detail in Chapter 4.

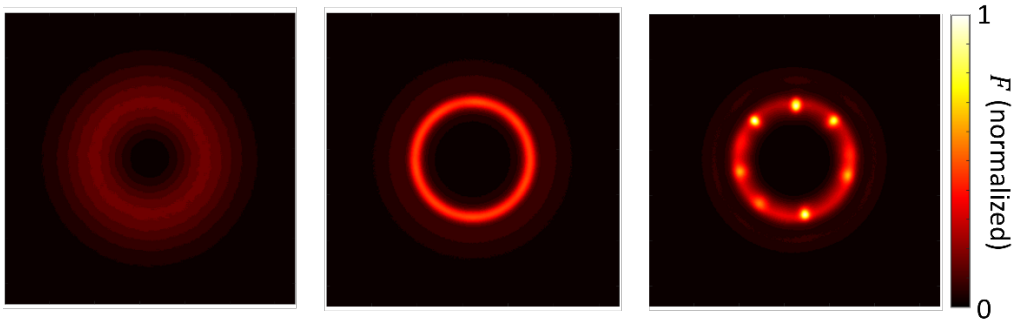

Figure 1.6 Transverse fluence profiles of filamenting LG_{01} beams simulated using UPPE (see Sec. 1.4.2 and [67]) from the initial beam (left), through initial self-focusing and ring narrowing (middle) until filament nucleation (right)

1.4 Modeling Filament Propagation

Throughout this thesis, simulation tools are used to supplement experimental results. Simulating filament propagation is non-trivial as the base equations are nonlinear partial differential equations, and due to the strong optical nonlinearities in filament propagation simulations require high fidelity. There are two main

equations used to model filamentation: the Nonlinear Schrödinger Equation (NLSE) and the Unidirectional Pulse Propagation Equation (UPPE).

1.4.1 Nonlinear Schrödinger Equation (NLSE)

The NLSE models nonlinear pulse propagation under the slowly varying envelope approximation (SVEA): $\left|\frac{d^2A}{dz^2}\right| \ll \left|k_0 \frac{dA}{dz}\right|$. The traditional NLSE, only including Kerr self-focusing, is [6]:

$$\frac{dA}{dz} = \frac{i}{2k_0}\nabla_\perp^2 A + ik_0 n_2 |A|^2 A \tag{1.27}$$

When including other nonlinear effects, such as ionization and molecular rotations, and some temporal effects, one can write a generalized NLSE [33]:

$$\frac{dA}{dz} = \frac{i}{2k_0}\nabla_\perp^2 A - i\frac{k''}{2}\frac{d^2A}{dt^2} + ik_0 n_2 |A|^2 A + \alpha n_2 n_0 \int_0^t R(t-\tau)|A(\tau)|^2 d\tau - i\frac{k_0}{2n_0}\frac{N_e}{N_{crit}}A \tag{1.28}$$

In Eq (1.28), the second term on the right corresponds to dispersion, the fourth term delayed rotational self-focusing with strength $\alpha n_2 n_0$, and the fifth term is plasma defocusing. This equation is also coupled with an ionization model, like MPI, to calculate electron density N_e. The NLSE and its derivatives have been used in many filamentation papers [68,69], but the SVEA is a severe limitation of the model. Although it is reasonably satisfied for pulses at the start of propagation (assuming said pulses are tens of femtoseconds long), it is not satisfied during filamentation, where supercontinuum generation leads to a broader spectrum and much shorter pulse features. For this reason, a solver that does not utilize the SVEA is necessary to properly model filamentation.

1.4.2 Unidirectional Pulse Propagation Equation (UPPE)

UPPE [67], in contrast with the NLSE, is derived from Maxwell's Equations with the unidirectional pulse approximation. The scalar form of UPPE, as described in this section, also assumes a linearly polarized beam. UPPE in 3D+1 (3D space + 1D time) space is a system of ordinary differential equations of the form:

$$\frac{\partial}{\partial z}A_{k_x,k_y}(\omega,z) = i2\pi Q_{k_x,k_y}(\omega)P_{k_x,k_y}(\omega,z)e^{-i\left(k_z-\frac{\omega}{v_g}\right)z} \tag{1.29}$$

In Eq. (1.29), $A_{k_x,k_y}(\omega,z)$ is the 3D inverse Fourier transform of the spacetime auxiliary field $A_{k_x,k_y}(\omega,z) = \mathcal{F}^{-1}_{x,y,\xi}\{E(x,y,\xi,z)e^{-ik_z\Delta z}\}$, where $\xi = t - z/v_g$ is time in the pulse frame of reference (traveling at the group velocity of the pulse's central frequency v_g) and Δz is the simulation step size. The transverse spatial frequencies (k_x, k_y) index a system of ordinary differential equations which are solved numerically. $P_{k_x,k_y}(\omega,z)$ is the nonlinear polarization of the medium, including Kerr self-focusing, rotational nonlinearities [9], ionization dynamics, and a plasma response. Including these nonlinearities, $P_{k_x,k_y}(\omega,z)$ can be written as:

$$P_{k_x,k_y}(\omega,z) = \mathcal{F}^{-1}_{x,y,\xi}\left\{\frac{4}{3\pi}n_0 n_2 Re\{E\}^3 + \frac{i4\pi e^2}{m_e\omega(\tau_c^{-1}-i\omega)}N_e E + \chi_{rot}E\right\} \tag{1.30}$$

The first term in Eq (1.30) corresponds to the full third-order electronic response (including third harmonic generation and the Kerr effect), the second term corresponds to the plasma response including electron-neutral collisions with collision time τ_c, and the third term is the rotational response. The other variables in Eq (1.29) are defined as follows: ω is the angular frequency, v_g is the group velocity of the medium at the pulse's central frequency, $k_z = ((\omega/v_g)^2 - (k_x^2 +$

$k_y^2))^{1/2}$ is the longitudinal spatial frequency, and $Q_{k_x,k_y}(\omega) = \omega/ck_z$. To recover the field in the spacetime domain, the auxiliary field is converted back to the electric field $E_{k_x,k_y}(\omega, z) = A_{k_x,k_y}(\omega, z)e^{ik_z\Delta z}$, and a 3D Fourier transform is performed on the electric field, $E(x, y, \xi, z) = \mathcal{F}_{k_x,k_y,\omega}\left\{E_{k_x,k_y}(\omega, z)\right\}$.

A cylindrically symmetric 2D+1 form of UPPE can also be derived, commonly used to model filamentation of Gaussian beams. The only differences for 2D+1 UPPE are that the two-dimensional spatial-frequency space (k_x, k_y) is reduced to a radial-frequency space k_r, and that conversions from r to k_r and back are performed using Hankel transforms [70] instead of Fourier transforms. Otherwise, these two models are identical.

1.5. Outline

This dissertation will first go over the impact of pulse duration on filament propagation in Chapter 2. Results show that pulse duration strongly affects both filament peak energy deposition and filament length, with variations largely being explained using molecular rotations and collisional ionization. A new filamentary phenomenon is also discussed, where pulses longer than ~200 fs FWHM generate periodic refocusing cycles due to molecular rotations and STOV dynamics.

Chapter 3 studies fog clearing using filamentation and shows the first direct measurement of the impact of a filament-induced acoustic wave on a water droplet, demonstrating a negligible amount of acoustic drag on the droplet. This result is corroborated with hydrocode simulations and extrapolations are made to estimate the results of stronger filament energy deposition.

In Chapter 4 there will be a discussion of long-distance air waveguiding using a multifilamenting LG_{01} beam. This chapter will demonstrate experimental guiding over 50m, a >60× improvement on previous work, and corroborate these results with simulation. Multifilamentation of LG_{01} beams will also be explained in detail, and UPPE simulations are used to show the seeding of filamentation for LG_{01} modes.

Chapter 5 discusses the generation of "quasi-steady-state" air waveguides, where the repetition rate of the filamenting pulse is increased so it replenishes the waveguide before it thermally dissipates. In this chapter waveguide lifetime will be thoroughly discussed, and how waveguide lifetime is related to the size of an air waveguide and the number of filaments generated.

Chapter 6 will be devoted to discussing the next steps for this research, including demonstrating the ability of air waveguides to be used in foggy and turbulent atmospheres, guiding high-average-power beams, and extending quasi-steady-state air waveguides to long distances.

Chapter 2 Impact of Pulse Duration on Atmospheric Filamentation

2.1 Introduction

Other work has shown that filament length can be extended by increasing initial beam size [28], increasing pulse energy [71], and improving beam collimation [72]. In Chapter 4, for example, long-distance air waveguiding was achieved by increasing the size of the beam and, therefore, increasing the Rayleigh range of the filament reservoir. However, filament length is also impacted by pulse duration. Results in Chapter 4 (see Fig. 4.3) show that a longer filament pulse duration increases filament length for pulse durations up to at least ~300 fs FWHM. This result necessitates a study of how precisely pulse duration impacts filament propagation in air, as does the increasing prominence of high-average-power kW Yb laser systems with narrower bandwidth, and therefore longer bandlimited pulses, than Ti:Sapphire [73,74].

Prior work on picosecond filamentation has studied tightly focused, $P \gg P_{crit}$ single filaments [17,75], while for long-distance applications an understanding of collimated or weakly-focused filamentation at peak powers below the multifilamentation threshold (only a few P_{crit}) [23] is necessary. Other work studying single filament length maintained a constant energy across pulse durations [71,76], which causes the "strength" of the filament (in terms of number of critical powers) to be different for each pulse duration. Some of these projects also correlate measured plasma fluorescence brightness with filament strength, but since energy deposition is the relevant parameter for many applications [48–

50,52,54–56] it would be beneficial to measure that directly. For these reasons, in this project we use a microphone array to measure longitudinally-resolved energy deposited by filaments across many pulse durations to measure changes in axial filament structure with pulse duration.

Nonlinear self-focusing in air has two components of relevance: instantaneous Kerr (or electronic) self-focusing and delayed self-focusing from O_2 and N_2 molecular rotations [9]. For the former, each time slice of the pulse focuses itself, whereas for the latter self-focusing is delayed by a characteristic time scale t_{rot}~100 fs in air [77]. The instantaneous Kerr effect strength is characterized by n_2. By contrast, the strength of the delayed rotational effect is related to the induced rotational susceptibility and its overlap with the self-focusing pulse. We can compute an effective rotational nonlinear index $n_{2,rot}$ from the induced rotational susceptibility $\chi_{rot}(t)$ by computing a normalized integral of the rotational susceptibility and pulse intensity $I(t)$ [25]:

$$n_{2,rot}(\tau) = \frac{\int \chi_{rot}(t) I(t) dt}{2 \int I^2(t) dt} \tag{2.1}$$

Which we then add to the standard Kerr n_2 to compute a pulse-duration-dependent critical power [78] $P_{crit}(\tau) = 3.77\lambda^2/8\pi n_{2,eff}(\tau) n_0$, where $n_{2,eff}(\tau) = n_2 + n_{2,rot}(\tau)$ as previously used in [24].

2.2 Experiment

For this experiment, we generate pulses using a Ti:Sapphire ($\lambda_0 = 812$ nm, $\Delta\lambda \sim 25$ nm) chirped-pulse amplification system with a minimum full-width-half-maximum (FWHM) pulse duration of $\tau = 45$ fs. The pulse compressor is a

diffractive grating pair where grating spacing is controlled by a motorized actuator. To change the pulse duration, we adjust the grating spacing to apply the needed linear chirp for the desired pulse duration. After the compressor we also measure shot-to-shot energy of the pulse with a calibrated CCD camera. After compression, we down-collimate the pulse with an off-axis reflective telescope to $w_0 \sim 1.4$ mm and with a slight focus $\sim f/1500$ to stabilize collapse location [53] and limit filament length to lab scales. We also run all pulses at peak power $P = 5.5P_{crit}(\tau)$ to compare dynamics for equivalent self-focusing strengths. Values of $n_{2,eff}(\tau)$ for different pulse durations are plotted in Fig. 2.1(a), and the pulse peak powers to maintain $P = 5.5P_{crit}(\tau)$ are plotted in Fig. 2.1(b). For our peak experimental pulse duration $\tau = 2$ ps, this corresponds to $\varepsilon_{pulse} \sim 30$ mJ.

The shot-to-shot longitudinal energy deposition is measured using a microphone array, seen in Fig. 2.1(c) and previously used in [53,55]. The microphone array consists of 64 microphones with a 2 cm spacing, each synchronized using a microcontroller hub. The microphones sample at 44.1 kHz, and therefore are impulsively driven by the MHz-frequency filament-generated acoustic wave. The strength of the impulse is directly proportional to the filament energy deposition per unit length at that location. The array is parallel to the filament axis and every microphone is 3 mm radially from the filament axis. For filament length and total energy deposition measurements, traces are stitched together starting from different z locations to cover the entire filament length. A Helium cell is also used to measure filament energy deposition for microphone calibration [26,79]. This calibration technique is described in detail in Appendix A1.

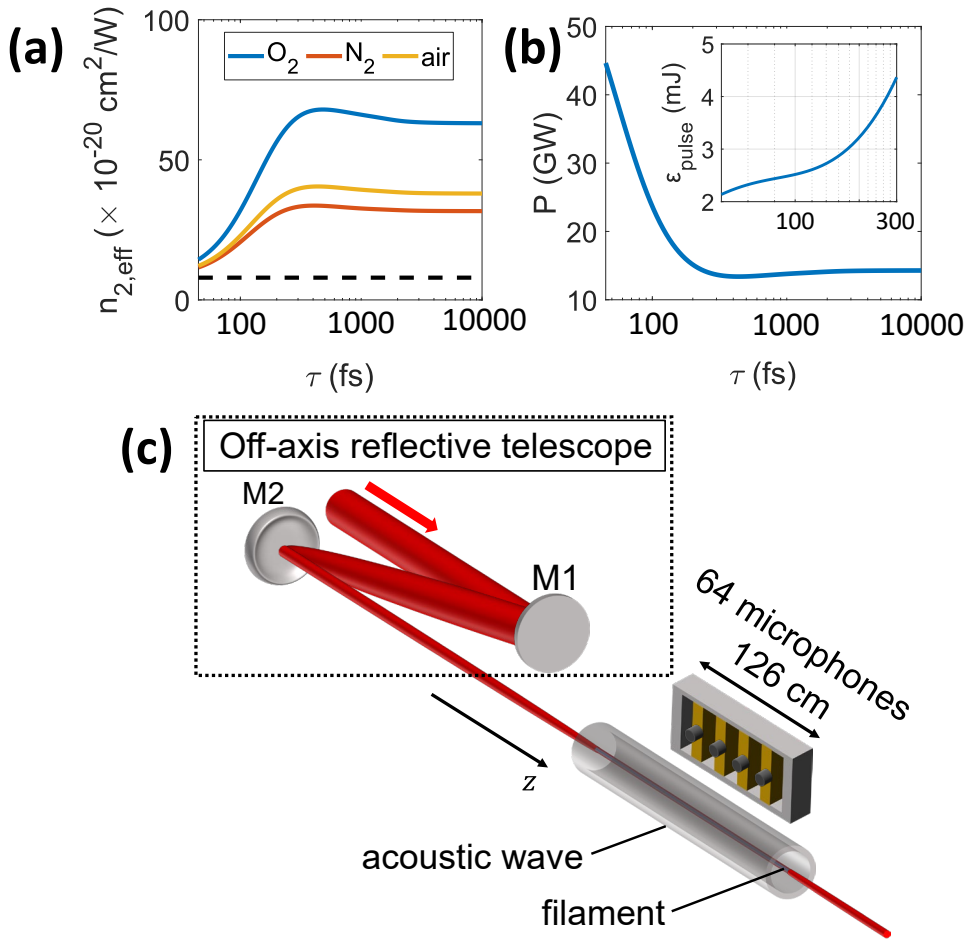

Figure 2.1 (a) $n_{2,eff}$ for 1 atm of O_2 (blue curve), 1 atm of N_2 (orange curve), and 1 atm of air (yellow curve, $n_{2,rot}(\tau)$) for the full range of pulse durations. The black dashed line corresponds to the electronic nonlinear index of air, $n_2 \approx 7.9 \times 10^{-20}$ cm^2/W [25]. **(b)** Operating pulse powers for all experimental pulse durations, chosen to keep $P = 5.5P_{crit}(\tau)$ when including the effects of molecular rotations. Inset: Pulse energies from 45 fs to 300 fs. **(c)** The microphone array experimental diagram. M1 (f = +75cm) and M2 (f = -25cm) are curved dielectric mirrors used to form the 3× down-collimating telescope.

These experiments are supplemented with an in-house pulse propagation tool called YAPPE (Yet Another Pulse Propagation Effort), based on UPPE (Unidirectional Pulse Propagation Equation) [67]. YAPPE allows us to simulate nonlinear atmospheric propagation and compute energy deposition from three different loss mechanisms: photoionization losses, molecular rotational deposition, and electron-neutral collisions. Simulations all use experimentally measured pulse

energies and durations, using $w_0 = 0.14$ cm and focal length $f = 400$ cm ($\sim f/1500$). The measured pulse energy only varies slightly from the fixed value $P = 5.5P_{crit}(\tau)$, so simulations are conducted in the "ideal" case (no chirp, $P = 5.5P_{crit}(\tau)$). Appendix A2 contains a discussion of precisely how YAPPE results are used to calculate energy deposition.

2.3 Results

2.3.1 Filament Length

Fig. 2.2(a) plots the simulated deposition and the stitched microphone trace for a $\tau = 500$ fs pulse. This figure shows a phase slippage between oscillations in experiment and simulation due to a slight difference in oscillation period, which can be explained by modelling uncertainties as discussed in Appendix A3. In Fig. 2.2(b), the filament length Δz_{fil} is plotted for all pulse durations. The filament length is defined as the total length over which we see energy deposition above $\partial_z \varepsilon_{dep} = 1.2$ μJ/cm, approximately half of the lowest peak deposition (at $\tau = 175$ fs), marked in Fig. 2.2(a). Here we can see that filament length increases with pulse duration, with a 5.5× increase from 45 fs to 2 ps. The filament length increase is due to two effects: (1) the enhanced self-focusing strength as pulse duration increases out to $\tau \sim 400$ fs, and (2) longer pulses supporting more refocusing cycles, as will be shown in Section 2.3.3. Our simulations predict a flattening in filament length for picosecond pulses due to the filaments having lower peak plasma densities, and therefore lower energy deposition. Plasma density decreases due to longer pulses needing lower intensity for substantial ionization, because of the

increase in collisional ionization with longer pulses. For this reason, there is little gain in filament length from increasing pulse duration beyond $\tau \sim 2$ ps. Fig. 2.2(c) is a plot of filament length per unit pulse energy ($\Delta z_{fil}/\varepsilon_{pulse}$), which is a metric to determine an optimal pulse duration for filament length in terms of energy cost. The optimal pulse durations are $\tau \sim 200 - 300$ fs, with $2.25{-}3\times$ filament elongation compared to 45 fs for only $\sim 1.5 - 2\times$ more pulse energy. This maximum is related to the change in $n_{2,eff}$ with pulse duration (see Fig. 2.1(a)), which peaks around $200 - 300$ fs as the pulse duration becomes much longer than the molecular rotational response time. For shorter pulses, higher peak powers are required due to the weaker self-focusing, driving down $\Delta z_{fil}/\varepsilon_{pulse}$. For longer pulses, the increase in filament length is less substantial because $n_{2,eff}$ no longer increases, and $\Delta z_{fil}/\varepsilon_{pulse}$ begins to decrease. Up until $\tau \sim 600$ fs, $\Delta z_{fil}/\varepsilon_{pulse}$ remains larger than ~ 20 cm/mJ, the value at 45 fs. While filament length still increases up until $\tau \sim 2$ ps, the energy cost per unit length substantially increases for pulses longer than 600 fs.

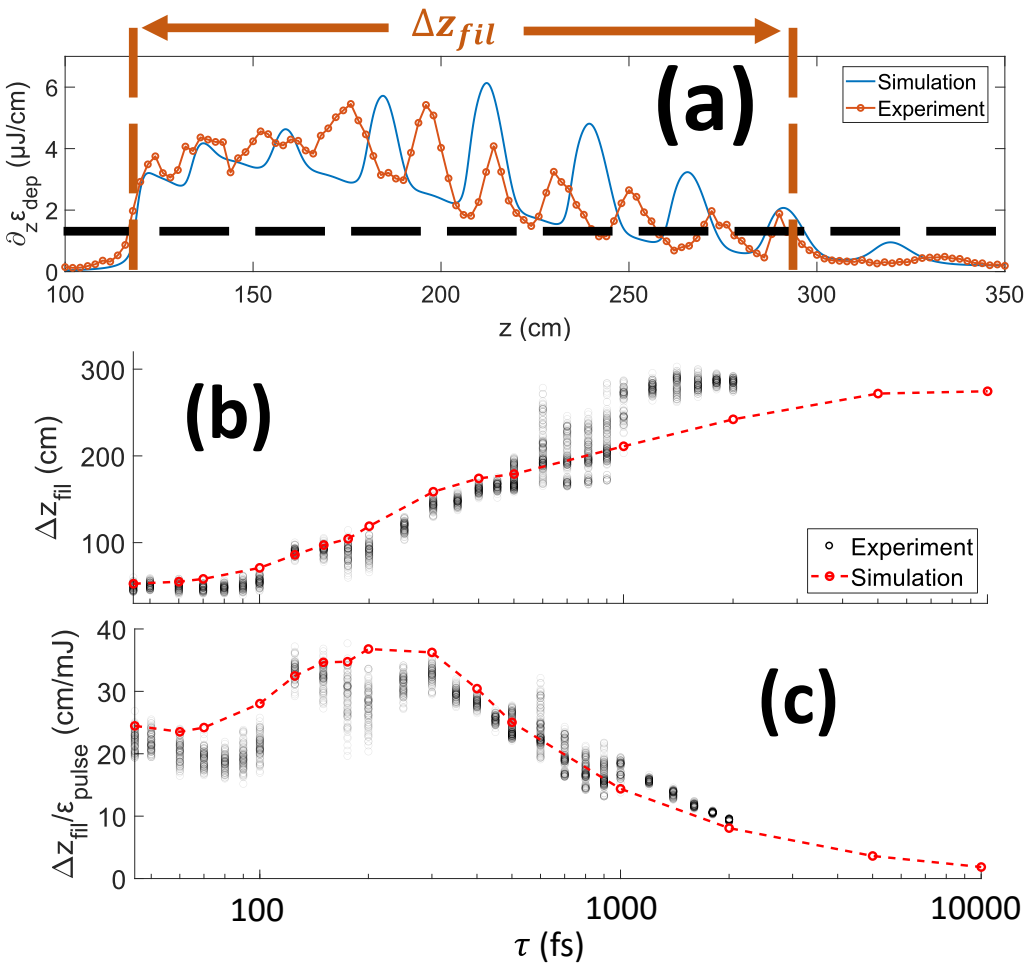

Figure 2.2 (a) A stitched microphone trace plotted with simulated deposition at $\tau = 500$ fs. The dashed black line corresponds to the filament threshold, $\partial_z \varepsilon_{dep} = 1.2$ μJ/cm, and the experimental filament length is labeled Δz_{fil}. **(b)** Filament length across pulse durations. Each black circle corresponds to the calculated Δz_{fil} for a single set of stitched microphone traces, 100 traces per pulse duration. The red dashed line traces simulated filament lengths at $P = 5.5P_{crit}$, with the red circles marking simulated values of Δz_{fil}. **(c)** Filament length per unit pulse energy for each pulse duration.

2.3.2 Peak Energy Deposition

Additionally, we use this data to see how pulse duration impacts energy deposition strength. Fig. 2.3(a) plots the peak energy deposition $\partial_z \varepsilon_{dep}$ for different pulse durations. A minimum in $\partial_z \varepsilon_{dep}$ occurs at $\tau \sim 175$ fs, due to the strong delayed rotational self-focusing peaking after the pulse intensity peak which limits the electron density in the filament and lowers peak energy deposition. Fig. 2.3(b)

demonstrates this by plotting the on-axis filament intensity $I(t)$ and self-focusing nonlinear index $\Delta n(t) = \sqrt{1+\chi_{rot}(t)} - 1 + n_2 I(t)$ versus time for several axial locations just after collapse arrest. For $\tau = 45$ fs, instantaneous Kerr self-focusing dominates and, therefore, the strongest parts of the pulse experience the strongest self-focusing. By contrast, for $\tau = 175$ fs, the peak of self-focusing effect is behind the pulse intensity maximum. This phenomenon limits the filament clamped intensity due to the weaker self-focusing at the intensity peak and, therefore, the peak deposition of the filament. As the pulse duration grows far past the rotational response time, molecular alignment overlaps more with the intensity peak of the pulse and the rotational nonlinearity becomes stronger due to the higher fluence, increasing the peak deposition due to the larger electron densities generated with the stronger self-focusing in the high-intensity region. This is also shown in Fig. 2.3(b) for $\tau = 300$ fs, where the rotations contribute more to the index shift at the intensity peak leading to a slightly higher index, and the delayed self-focusing strength is generally higher. Peak deposition increases with pulse duration for experimental data past 175 fs, although longer pulses are studied through simulation and show a more complicated pulse duration dependence. The drop in simulated $\partial_z \varepsilon_{dep}$ at $\tau = 10$ ps is due to the increased avalanche ionization – collapse arrest occurs at a lower intensity and with less photoionization due to avalanche, leading to a lower peak deposition. The spike in simulated peak $\partial_z \varepsilon_{dep}$ at $\tau = 5$ ps is due to a short spike in deposition that does not reflect an overall higher deposition. In Fig. 2.3(c) we plot the total energy deposition per unit pulse energy. The percentage of pulse energy deposited strictly decreases with pulse

duration, indicating that we cannot improve energy deposition efficiency using longer pulses even through increased electron-neutral collisions, since collisional ionization decreases the peak intensity in the filament which decreases the total deposition.

The match between experimental and simulation results indicates that the experimental chirp strength is not a significant factor in air over these distances, at least for these filament properties. For a propagation length of 5m, one would anticipate (for $\lambda_0 = 800$ nm and air group velocity dispersion of 0.02 fs^2/mm [80]) ~100 fs^2 of accumulated second-order dispersion, enough to only change a pulse duration of 45 fs by less than a femtosecond, so the applied chirp to longer pulses would dominate the dispersion accumulated through air. To analyze the impact of pulse chirp, we ran a set of simulations with a 22 nm bandwidth (bandwidth-limited 45 fs pulse) and added dispersion coefficients from second to fourth order consistent with a grating pair compressor to generate longer pulses. This set of runs differ from our bandlimited simulation with an average 3.4% change in Δz_{fil} and 3.8% change in $\partial_z \varepsilon_{dep}$ and a maximum 10% decrease in Δz_{fil} (at $\tau = 200$ fs) and 20% increase in $\partial_z \varepsilon_{dep}$ (at $\tau = 2$ ps), all while keeping the same approximate collapse location and deposition structure. This small variation indicates that chirp does not substantially change our simulation results, and the bandlimited simulations are sufficient.

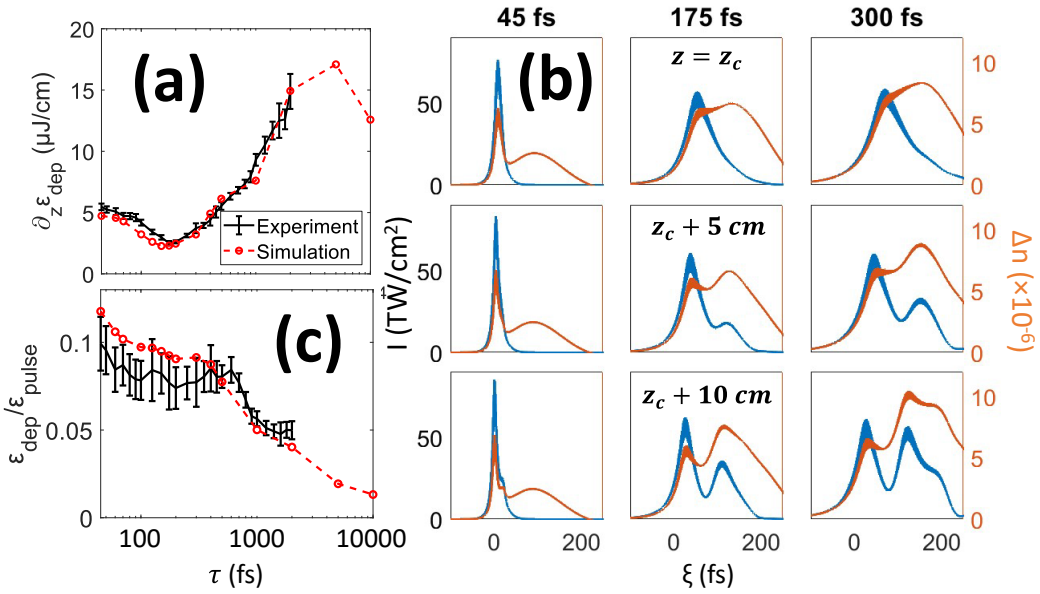

Figure 2.3 (a) Peak $\partial_z \varepsilon_{dep}$ for each pulse duration. Error bars are the shot-to-shot standard deviation of peak $\partial_z \varepsilon_{dep}$. The dashed red line is the simulated peak deposition, red circles marking simulated values of $\partial_z \varepsilon_{dep}$. **(b)** Simulated on-axis intensities and self-focusing nonlinear index of refraction for three different pulse durations, one for each column, just after filament collapse arrest. **(c)** Fraction of pulse energy deposited ($\varepsilon_{dep}/\varepsilon_{pulse}$) for each pulse duration, experimental and simulated. The experimental error bars correspond to the total uncertainty from microphone noise, shot-to-shot deposition variance, and shot-to-shot pulse energy variance.

2.3.3 Periodic Refocusing Cycles

In our experiments we observe the appearance and growth of longitudinal oscillations with increasing pulse duration. Although similar oscillations have been observed in prior simulation work with only a delayed self-focusing [81], they have not been observed in atmospheric settings from increasing pulse duration, and their cause has not been determined. Fig. 2.4(a) shows our measurements for three pulse durations showing oscillation growth, with a roughly fixed period for all pulse durations around 22 cm. To explain the oscillations measured with our microphone array, we look in more detail at simulation results. Fig. 2.4(b) shows the simulated on-axis temporal intensity for a $\tau = 400$ fs pulse at several propagation distances on the top row with the on-axis nonlinear phase curvature underneath. The on-axis

nonlinear phase curvature, $\partial_r^2 \phi_{nl}(\xi, z) = \partial_r^2 \{k_0 \int_0^z \Delta n_{nl}(r, \xi, z) dz'\}|_{r=0}$, is calculated from the effective index of refraction of each nonlinear effect $\Delta n_{nl}(r, \xi, z)$ integrated over the propagation direction z. This figure shows refocusing cycles occurring at a fixed temporal location correlated with a strong focusing phase curvature due to the rotational nonlinearity, supported by a leading pulse train from the previous refocusing cycles. The pulse then splits once it reaches ionization due to the strong plasma index gradient. The front half of the pulse then joins the leading pulse train, contributing to rotational self-focusing for the next cycle. The leading pulses are maintained by STOV-induced energy flow, demonstrated in Fig. 2.4(c). Each refocusing cycle forms a new STOV pair, consistent with past work studying filament STOV formation [26]. However, none of the STOVs annihilate – the front pulse train has a build-up of +1 STOVs, and the back pulse train has the same but with -1 STOVs. This is important as STOVs dictate energy flow for each pulse; the +1 STOVs impose a focusing phase curvature in front of each pulse and a defocusing phase curvature behind each pulse, preventing the intensity from decreasing and keeping the total fluence roughly constant. As the +1 and -1 STOVs from each refocusing cycle separate, molecular rotations induced by the leading pulse train cause the region between the STOV pair to self-focus, changing the defocusing curvature to a focusing curvature. This initiates another refocusing cycle, a process described in [34]. Additionally, longer pulse durations create stronger refocusing cycles owing to the higher on-axis fluence inducing a stronger rotational response.

In Fig. 2.4(d) simulated energy deposition at $P = 5.5P_{crit}$ (computed with $n_{2,rot} = 0$) and $\tau = 400$ fs without molecular rotations is plotted alongside a simulation with rotations on. Without molecular rotations, refocusing cycles still occur and the filament length is somewhat longer. This result shows that the longer pulse duration itself drives longer filament lengths by supporting more refocusing cycles. However, without rotations the refocusing cycles are irregular. The molecular rotations themselves generate a fixed-spacing pulse train, leading to *periodic* refocusing cycles, and generate longer filaments with much lower energies.

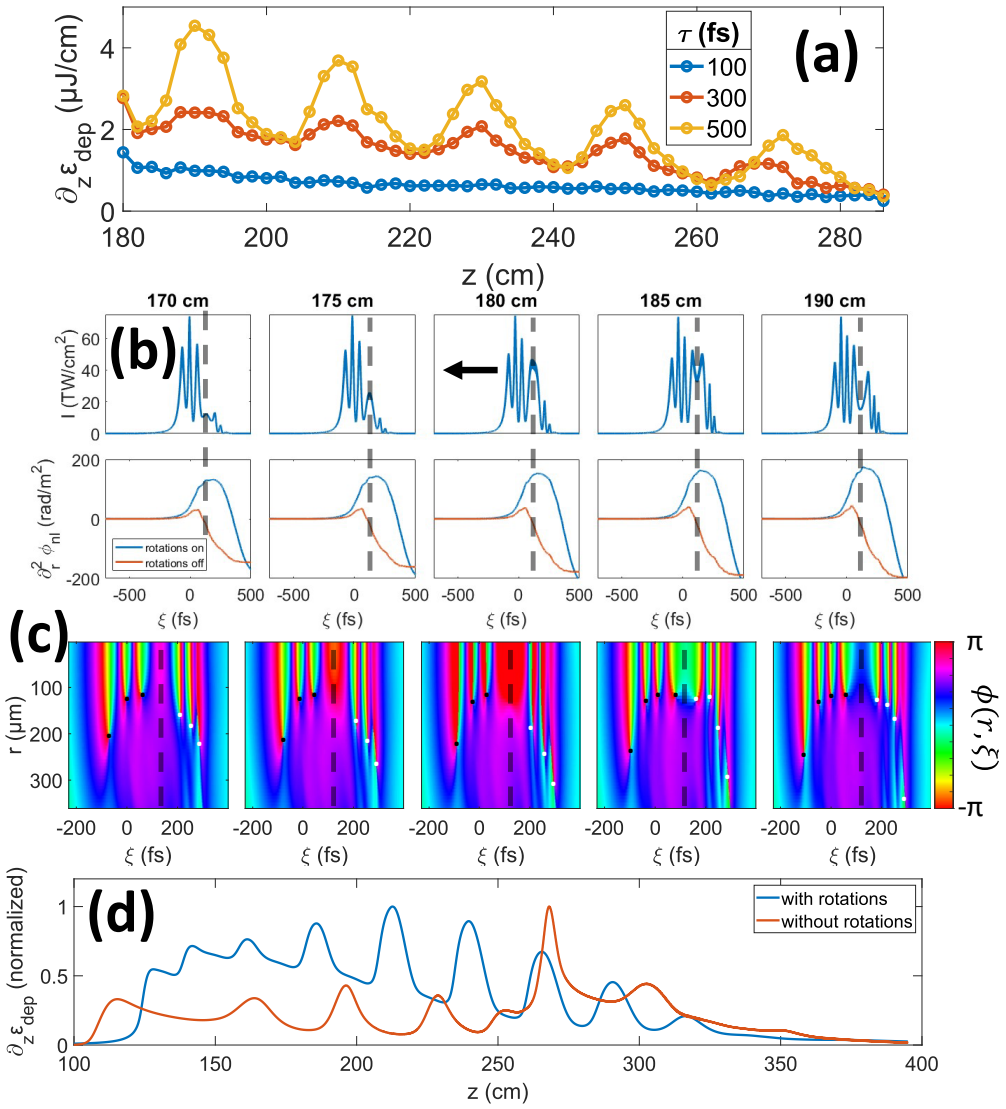

Figure 2.4 (a) Microphone traces showing oscillation growth with pulse duration. **(b)** Top row: The on-axis intensity of a simulated $\tau = 400$ fs filament. The black arrow in the panel marks pulse propagation direction, right-to-left, for all panels. Bottom row: The accumulated nonlinear phase curvature, $\partial_r^2 \phi_{nl}$, with and without the rotational nonlinearity for each z location, calculated from simulation. The grey dashed line marks the temporal location of the refocusing cycle for each z. **(c)** Figures showing phase $\phi(r, \xi)$ of the same filament in (b) mid-propagation with STOV generation. +1 STOVs are marked with black dots and -1 STOVs are marked with white dots. Each plot corresponds to the same z locations marked in the columns of (b), from 170 cm to 190 cm left-to-right, and the gray dashed line marks the same ξ location as in (b). **(d)** Plot of simulated filament energy deposition with (blue, 5.7mJ) and without (orange, 30mJ) molecular rotations turned on, each at $P = 5.5P_{crit}$, $\tau = 400$ fs. In each trace, the deposition is normalized by the maximum value to emphasize structural differences in deposition.

2.4 Conclusions

In conclusion, we find that the duration of a filamenting pulse drastically impacts the filament's longitudinal structure. Longer pulses form longer filaments because they can support more refocusing cycles, each cycle lengthening the filament. Simulations indicate that longer pulses, out to 10 ps, no longer generate notably longer filaments due to avalanche ionization arresting collapse at lower intensity. The measured $5.5\times$ increase in filament length from 45 fs to 2 ps can be used to elongate small multifilamentation structures for applications such as single-mode air waveguiding [55]. High-average-power ultrafast laser systems are practical choices for long-distance filamentation, especially for systems where 200 fs – 700 fs pulse durations are achievable so the pulse energy cost per unit length is similar to or better than that for a 45 fs pulse with higher peak energy deposition. For pulses longer than $\tau \sim 175$ fs, there is a large growth in longitudinal oscillations with a 22 cm period from a rotationally-induced periodic refocusing effect, also mediated by the STOVs generated in each refocusing cycle. We note that there is no reason to believe that these oscillations are a phenomenon specific to air; a filament in any medium with a strong delayed self-focusing nonlinearity should produce similar periodic refocusing for pulses longer than the characteristic time scale of the nonlinearity.

Chapter 3 Aerosol Clearing and Filamentation

3.1 Introduction

As discussed in Chapter 1, femtosecond filaments in air deposit energy primarily through plasma generation and rotational excitation of O_2 and N_2 [10,57]. Inverse Bremsstrahlung heating from electron-neutral collisions is negligible for the sub-picosecond pulses typically used in air filamentation [45]. Energy deposition is impulsive on the timescale of the acoustic response of air to the filament, $\tau_a \sim d_{\mathrm{core}}/2c_s \sim 300$ ns, using $c_s \sim 300$ m/s for the speed of sound in atmosphere. The impulsively heated air launches a locally cylindrical single-cycle acoustic wave, leaving behind a density depression, or "density hole", along the laser axis that lasts for several milliseconds [47,54]. The strength of the acoustic wave and depth of the density depression are each proportional to the energy deposited per unit length [28].

One important application of air filamentation is fog clearing. Prior experiments [51,52] have shown that a filament propagating in a fog chamber improves the transmission of optical pulses injected immediately afterward along the filament axis. Fog droplet clearing has also been demonstrated using a timed sequence of pump pulses which heat the air by resonantly exciting molecular rotations [82]. Such droplet clearing may have applications in optical data transmission [52] or directed energy [83]. While the physical mechanism for improved transmission has been suggested to be droplet clearing by the laser-induced acoustic wave [51,82], to date there have been no direct measurements of

this or other possible mechanisms.

In this chapter, we directly measure and simulate the dynamics of carefully positioned ~5 μm radius water droplets under the influence of optical and acoustic interactions characteristic of femtosecond filaments in air. Droplets of this size are well within the typical aerosol size distribution of fog [84,85]. We find that for filaments generated by the collapse of collimated near-infrared femtosecond pulses, the main clearing mechanism of droplets is optical shattering by the laser light. For such filaments, the single cycle acoustic wave launched by filament energy deposition leaves droplets intact and drives negligible radial displacement. We find that only for tightly focused non-filamentary pulses, where local energy deposition greatly exceeds that of a filament, can acoustic waves significantly displace aerosols.

3.2 Mechanisms for Water Droplet Clearing

We anticipate two main droplet clearing mechanisms and set up two experiments to study them. We consider a droplet "cleared" when it is either transversely displaced, largely intact, from the beam path of a subsequent pulse, or shattered into sufficiently small fragments (in the Rayleigh scattering regime) that scattering losses of a subsequent pulse would be greatly reduced. For both experiments, we used a Ti:Sapphire (λ_0 = 812 nm, pulse full width at half maximum τ = 45 fs, pulse rate 10 Hz) pump beam for generating a filament and a spatially-filtered, frequency-doubled Nd:YAG (λ_0 = 532 nm, τ ~ 7 ns, 10 Hz) probe beam to image droplets and the hydrodynamics driven by the laser-heated air. The delay of the probe relative to the pump was electronically controlled by a digital delay

box, with few nanosecond jitter insignificant compared to the displacement time of the droplet. Individual 5 ± 1.5 μm radius distilled water droplets were generated by a piezoelectric-driven 10 μm inner diameter nozzle mounted on a 3D translation stage and synchronized to the pump and probe pulses (see Fig. 3.1(a)). The nozzle was positioned above the laser axis and pointing down, so the droplets entered the laser beam by gravity. Rough positioning of the droplet with respect to the laser axis was controlled using the digital delay, with fine 2D positioning in the transverse plane controlled with the translation stage. The droplet was positioned at the longitudinal location where the filament energy deposition and acoustic wave amplitude were maximized.

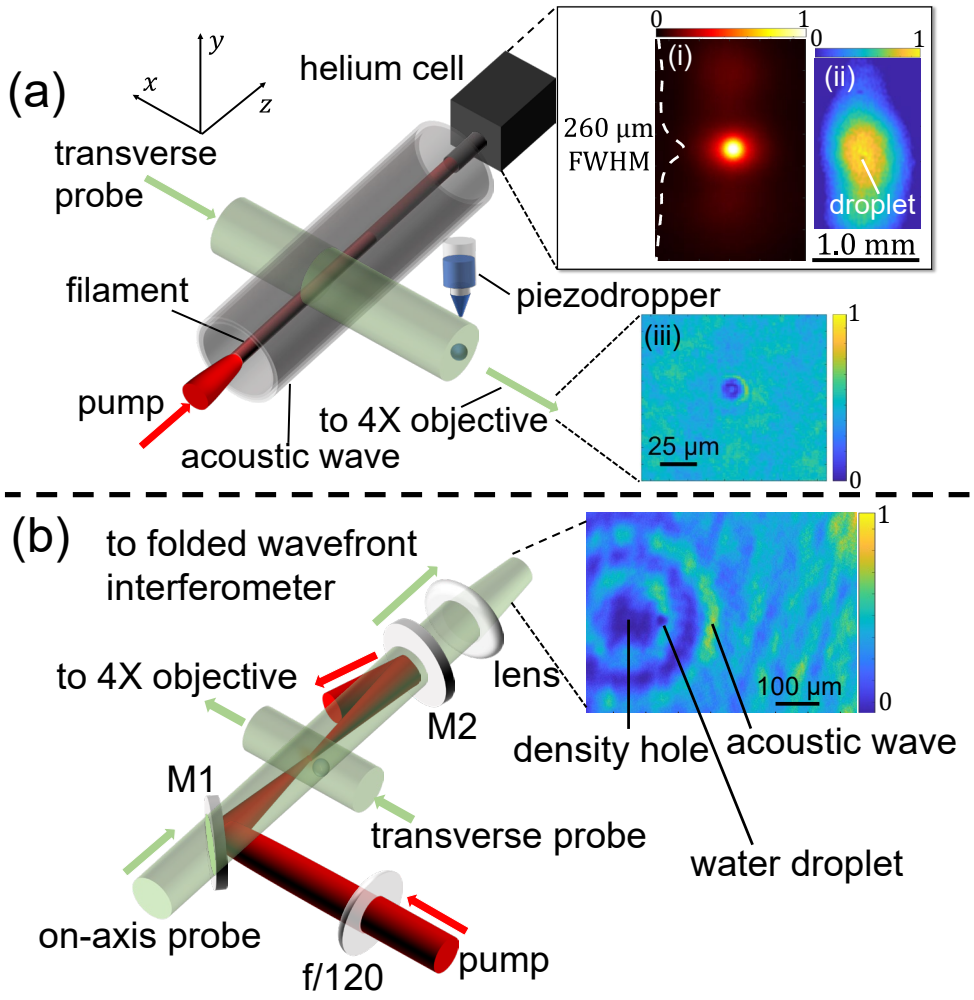

Figure 3.1 (a) Diagram of Experiment 1. A beam is down-collimated by a reflective telescope to a $w_0 = 1\ mm$ waist (e^{-2} intensity radius) to generate a filament with peak intensity $I_0 \sim 80\ TW/cm^2$ (estimated from panel (a)(i) and simulations), radiating a single-cycle acoustic wave. The filament is terminated mid-flight by a helium cell, enabling linear imaging of the filament cross section [26,79]. A piezodropper places a 5 μm radius droplet a controlled distance from the center of the filament core; the droplet interaction is imaged from the side using a λ_0 = 532 nm, 7 ns transverse probe. (i) End-on image of filament core intensity profile, using the He cell, with the y lineout plotted. (ii) End-on image of the droplet in a low-power beam. (iii) Side-image of an unperturbed 5 μm radius droplet. All colormaps are in arbitrary units. **(b)** Diagram of Experiment 2. A dielectric mirror (M1) is used to co-propagate the pump and on-axis probe, and a second dielectric mirror (M2) filters out the pump to image the probe. The peak intensity for this $f/120$ focusing geometry is $I_0 \sim 160\ TW/cm^2$ at the highest pump energy. Inset: End-on image showing the density hole, radial acoustic wave, and water droplet. The colormap is in arbitrary units.

In Experiment 1 (Fig. 3.1(a)), the pump beam is a filament generated using a near-collimated beam, where self-focusing is not assisted by a focusing optic (in

contrast to [51,52]). The collimated beam configuration is most likely to be used for long range filament applications in the field. The goal in this experiment was to observe the relative contributions of radial droplet displacement and droplet shattering to clearing by a filament without lens assistance.

To generate single filaments in the lab, a 2.8 mJ pump pulse was down-collimated by a reflective telescope to a $w_0 = 1$ mm waist (e^{-2} intensity radius). The filament was terminated mid-flight ~40 cm after collapse and immediately after interaction with the droplet by an abrupt ~4 mm air-to-helium transition in the 1/2" diameter nozzle of a slowly outflowing helium cell [26,79], maintained at a slight positive pressure to the ambient air. Helium cell termination of the filament enabled end-on imaging of the filament intensity profile and calibration of the droplet position with respect to the center of the filament. The intensity profile was further attenuated by wedges in and after the helium cell to ensure linear propagation for imaging. Insets of Fig. 3.1(a) show images from the helium cell: an end-on image and lineout of a filament core (with $d_{\mathrm{core}} \sim 260$ μm, in good agreement with propagation simulations for these conditions [67]), and an image of an unfilamented lower energy beam with a droplet 50 μm away from the beam axis. A side-imaging system with 4 × magnification (see Fig. 3.1(a) and (b)) used the transverse λ_0 = 532 nm probe beam to image filament-droplet interaction dynamics.

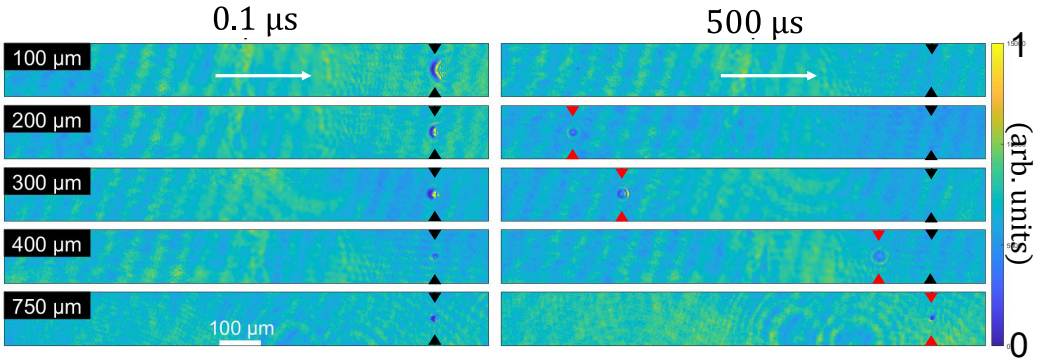

Figure 3.2 Shadowgrams of filament-induced dynamics for ~5 µm radius droplets placed at varying radial distance (labels at left) from the center of the filament core. The filament propagates from left to right (white arrows). The two columns show droplet images at 0.1 µs and 500 µs after filament arrival. The black arrows mark the initial droplet axial location, while the red arrows mark the droplet location (if a droplet is still present) 500 µs after the filament interaction. As the droplet is moved closer to the beam axis, the images at 0.1 µs show droplet distortion and far side cavitation, while the 500 µs images show axial droplet displacement toward the laser and the complete disintegration of droplets placed closer than ~200 µm from the core centre.

Figure 3.2 shows a sequence of side-shadowgrams at 0.1 µs and 500 µs after the filament of the droplet interaction as the droplet is translated closer to the filament core center from directly above. The 500 µs delay is chosen to match that for optimal transmission of a pulse following the filament in a prior fog clearing experiment [52]. It is seen from the 0.1 µs-delay panels that at ~750 µm from the center the droplet is unaffected, but as the droplet is moved closer, it increasingly deforms and cavitates owing to mass ejection from its far side (away from the laser). In the corresponding 500 µs delay panels, the droplet is seen to have reformed its shape and moved along the optical axis *toward* the laser, owing to a momentum boost from the mass ejection. At less than 200 µm (150 µm) from the core in the vertical (horizontal) direction, the droplet has completely disintegrated; in the 500 µs panel, there is no evidence of probe scattering by droplet fragments. The

vertical-horizontal asymmetry originates from slight asymmetry of the filament cross section, as seen in Fig. 3.1(a)(i). At no droplet position is there any evidence of *radial* droplet displacement away from the filament, which is what one would expect if the cylindrical acoustic wave contributed significantly to droplet clearing [51]. Since droplet shattering occurs at the edge of the filament core but well inside the reservoir radius ($w_0 \sim 1$ mm), with cavitation and mass expulsion occurring on the far side of the droplet, we conclude that laser light from the filament reservoir is focused by the droplet, with strong heating on the far side. This scenario has been discussed in [86], where the geometric focus of a droplet with $ka = 2\pi a/\lambda \gg 1$ ($ka \sim 40$ for radius $a = 5$ μm droplets) leads to a radius-independent ~7.6 × intensity enhancement [86] at the far side, promoting cavitation and mass expulsion. Optical breakdown in water droplets has also been simulated in ref. [87], which shows the same focusing effect with additional free electrons generated on the front face of the droplet at filament core intensities (> 10 TW/cm^2).

To verify that the laser fluence in the filament reservoir is sufficient to initiate breakdown and plasma formation in a droplet, we simulated filamentary propagation with a unidirectional pulse propagation code [67,88] using our experimental parameters. We determined the radius at which the filament intensity dropped below 1.3 TW/cm^2; this is our estimated damage threshold based on a water ionization breakdown intensity of 10 TW/cm^2 [89] and the 7.6 × intensity enhancement from droplet focusing. We saw in these simulations that the filament reservoir fluence fell below 1.3 TW/cm^2 at a radial position of 580 μm from the beam axis. This is significantly larger than the measured shattering radius, but water

breakdown occurs in both shattered *and* deformed droplets. It is worth noting that we see significant deformation out to 400 μm and no deformation at 750 μm in Fig. 3.2, so that that our results match well with this breakdown estimate.

The goal of Experiment 2 was to observe droplet clearing effects using a laser intensity profile resembling the most intense part of the filament core (~100 μm, or approximately half the core diameter) where laser energy is deposited from plasma generation. The setup, shown in Fig. 3.1(b), uses an $f/120$ lens-focused pulse so that the beam waist diameter ($2w_0$ ~ 100 μm) matches this. With little to no laser flux radially outside $\sim w_0$, any droplet clearing from that region would not be directly optically-driven; a strong candidate would be clearing by the laser-induced acoustic wave. In the experiment, the pulse energy ε_{pump} was adjusted in the range $100 - 500$ μJ in order to match and exceed the energy deposition per unit length, $\partial_z \varepsilon_{dep}$, of a real filament core, and thus launch an acoustic wave of at least equal amplitude. The energy deposition was measured interferometrically using a portion of the λ = 532 nm pulse transmitted through the λ = 800nm mirror M1 and directed along the pump beam axis. This on-axis probe picks up a phase shift $\Delta\Phi(\mathbf{r}_\perp)$ from the long-lasting air density depression left by pump heating, as described in [28]. The energy deposition per unit length is given by [28] $\partial_z \varepsilon_{dep} = -c_\mathrm{v} T_0 \rho_0 k^{-1} L^{-1} (n-1)^{-1} \int d^2\mathbf{r}_\perp \Delta\Phi(\mathbf{r}_\perp)$, where the integral is over the cross section of the density hole, the simulated [67] axial FWHM of air heating is $L \sim 2$ cm (less than the confocal parameter of $2z_0 \sim 2.8$ cm owing to the strongly nonlinear heating), $c_\mathrm{v} = 0.72$ kJ/(kg K) is the isochoric specific heat of air [90], $T_0 = 297$ K is the ambient air temperature, $\rho_0 = 1.23$ kg/m^3 is the air mass

density [91], $k^{-1} = 84.7$ nm is the inverse wavenumber of the probe, and $(n - 1) = 2.8 \times 10^{-4}$ is the air index of refraction increment [92].

Energy deposition $\partial_z \varepsilon_{dep}$ vs. ε_{pump} is plotted in Fig. 3.3(a). For ε_{pump} = 450 μJ, $\partial_z \varepsilon_{dep}$ exceeds by ~40% our prior measurements of maximum deposition of 3.5 μJ/cm in a real filament [28]. Therefore, near the focus in Experiment 2, the launched acoustic wave for ε_{pump} = 450 μJ is stronger than an acoustic wave from a real filament; we use this experiment to determine an upper bound on acoustically-induced droplet displacement.

The droplet initial and final positions, R_{init} and R_{final}, were imaged using the transverse λ_0 = 532 nm, τ ~ 7 ns probe pulse. To enable sensitive detection of potentially small laser-induced position changes, every other pump pulse was blocked for collection of a droplet image with pump absent. These were then binned based on the droplet's blocked-pump position (R_{init}) with respect to the pump axis. The mean droplet displacement ($\overline{\Delta R}_{drop} = \bar{R}_{final} - \bar{R}_{init}$) after 500 μs delay is plotted in Fig. 3.3(b) as a function of ε_{pump} for R_{init} in the range $100 - 110$ μm, which encompasses the slight shot-to-shot variations in initial droplet location. The overbars represent a mean over ~100 shots at each point. For $\varepsilon_{pump} = 450$ μJ , the droplet is shattered by the beam focus for $R_{init} < 100$ μm. Figure 3.3(c) plots $\overline{\Delta R}_{drop}$ vs. $\bar{R}_{init}$ at 500 μs delay for $\varepsilon_{pump} = 450$ μJ. In both Fig. 3.3(b) and (c), the error bars represent the displacement variance $\pm \Delta R_{var}$ over the ~100 shots at each point. The red bands in these panels are results from a hydrocode-simulation of acoustically-driven droplet displacement (to be discussed in Sec. 3.3.1).

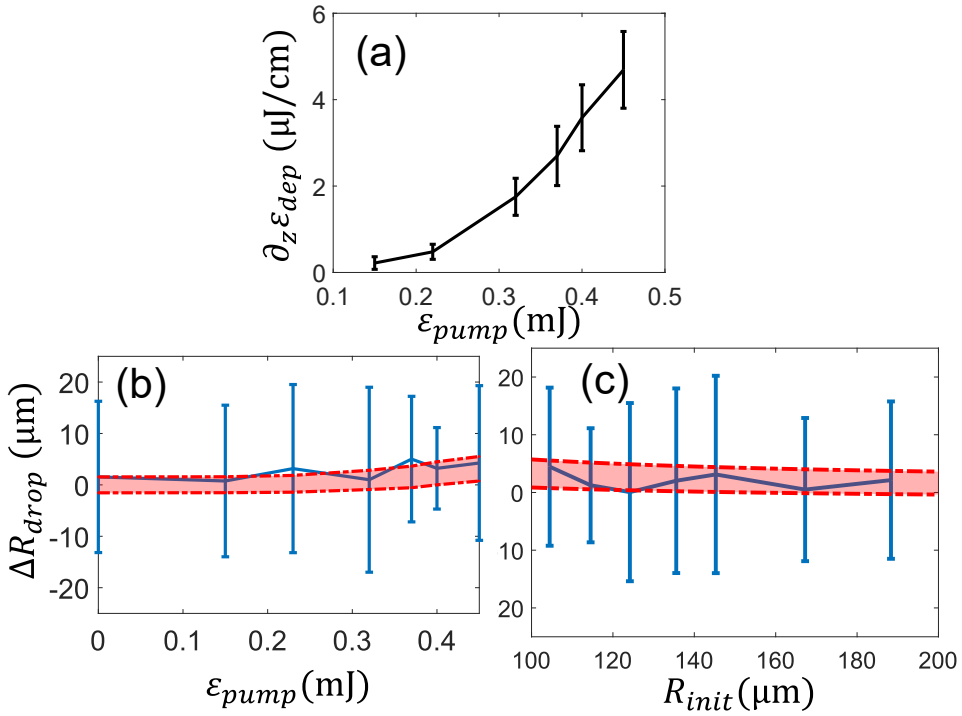

Figure 3.3 (a) Energy deposition per unit length $\partial_z \varepsilon_{dep}$ vs. pump energy ε_{pump}. **(b)** Droplet displacement ΔR_{drop} as a function of pump energy for initial position $R_{init} = 100\ \mu m - 110\ \mu m$. The blue trace is the mean displacement $\overline{\Delta R}_{drop}$ and the error bars represent variance over 100 shots at each point. The red region is ΔR_{drop} from simulations (see Sec. 3.3.1). **(c)** ΔR_{drop} vs. R_{init} for $\varepsilon_{pump} = 450$ μJ. Each value of R_{init} plotted corresponds to the average at that point, with standard deviation < 4.5 μm.

Both Fig. 3.3(b) and 3.3(c) show a very weak trend of increasing droplet displacement for increasing ε_{pump} and decreasing R_{init}. In both cases, however, the maximum $\overline{\Delta R}_{drop}$ of ~5 μm is small compared to both ΔR_{var} and the variation of initial droplet positions. Even if we consider a maximum acoustic clearing displacement of $\Delta R_{var} \sim 20$ μm, this is still insufficient for acoustic droplet clearing by a real filament: for $R_{init} = 100$ μm, the displaced droplet would still be well within the filament's optical shattering radius (150-200 μm), as discussed earlier for Experiment 1. We therefore conclude that in a real filament, the intense core alone would not generate an acoustic wave of sufficient strength to clear a

~5 μm radius water droplet typical of fog.

3.3 Simulations and High-Deposition Clearing

3.3.1 Hydrocode simulations

Our experimental results for acoustic droplet clearing were compared with a 1D+time cylindrically symmetric hydrocode. Because energy deposition by a filament is impulsive [47,57], we assume that the initial excitation of the air is a heated region with radial temperature profile $\Delta T(r, t = 0) = \Delta T_{peak} \exp(-2(r/r_h)^2)$, where $r_h = 60$ μm (unless otherwise stated) and $\Delta T_{peak} = 2(\pi r_h^2 \rho_0 c_v)^{-1} \partial_z \varepsilon_{dep}$ is given by the measured energy deposition of Fig. 3.3, and plotted versus $\partial_z \varepsilon_{dep}$ in Fig. 3.4(a). The simulation then computes the gas evolution and the resulting drag and pressure gradient forces on the droplet.

The hydrocode solves (using [93]) the fluid conservation equations

$$\frac{\partial \xi_i}{\partial t} + \frac{1}{r} \frac{\partial}{\partial r} r(\xi_i v + \phi_i) = 0 \tag{3.1}$$

where the ξ_i are the conserved densities and the ϕ_i are their forced fluxes. Here, $\xi_1 = \rho(r, t)$ is the air mass density, $\xi_2 = \rho v(r, t)$ is the momentum density, and $\xi_3 = \epsilon + \rho v^2/2$ is the energy density, where the air is taken as an ideal gas of internal energy density $\epsilon(r, t) = 3(\rho/m) k_B T(r, t)/2$ and pressure $P(r, t) = 2\epsilon/3$, with an average molecular mass $m = 0.8 m_{N2} + 0.2 m_{O2}$. The corresponding source fluxes are $\phi_1 = 0$, $\phi_2 = P + \tau$, and $\phi_3 = (P + \tau)v + q$, where $\tau =$

$\frac{4}{3}\eta(T)\,\partial v/\partial r$ is the shear stress and $q = -\kappa(T)\,\partial T/\partial r$ is the thermal flux. Here, η is the dynamic viscosity and κ is the thermal conductivity of air [94].

The output of the fluid simulation is then used to compute the acoustically-driven motion of a spherical water droplet of radius a, mass M and radial position R, where the force F_{drop} on the droplet is taken as the sum of the local pressure gradient and drag force from the acoustic wave:

$$M\frac{d^2R}{dt^2} = F_{drop}$$
$$F_{drop}(t) = \pi a^2\left(\frac{\partial P}{\partial r} + 0.5C_d\rho\left[\frac{dR}{dt} - v\right]^2 \mathrm{sgn}(v - \frac{dR}{dt})\right) \tag{3.2}$$

Here, $p = p(R(t),t)$, $v = v(R(t),t)$, $\rho = \rho(R(t),t)$ are the fluid pressure, velocity, and density evaluated at the droplet position $R(t)$. The drag coefficient C_d is a strong function of the Reynolds number ($Re = 2a\rho v\eta^{-1}$) of the flow around small droplets. We consider two drag regimes: $Re \leq 0.2$, for which $C_d = 24/Re$ follows Stokes' Law [94], and $Re > 0.2$, for which $C_d = 21.12/Re + 6.3/\sqrt{Re} + 0.25$ is a fit between the static C_d = 0.47 for $Re > 1000$ and Stokes' Law [94]. We note that $Re > 1000$ is unreachable with the droplet sizes and air /droplet velocities in this chapter.

The simulation results are shown in the red bands overlaid on the experimental results in Figs. 3.3(b) and (c), showing excellent overlap, and verifying that filament-induced acoustic clearing of ~5 μm radius water droplets is negligible.

The bands plot the simulated droplet displacement incorporating experimental shot-to-shot variations in energy deposition and initial droplet position R_{init}, and the uncertainty in droplet size. The energy deposition fluctuations were accounted for by initiating the hydrocode simulations by varying ΔT_{peak} for each ε_{pump} in Fig. 3.3(a). The variation in droplet displacement owing to measurement uncertainty in droplet radius a was accounted for by simulating the smallest and largest a within a standard deviation of the mean. Additionally, the mean displacement $\overline{\Delta R}_{drop}$ at ε_{pump} = 0 was added to the upper bound and subtracted from the lower bound of the simulated range since any acoustic displacement would add onto that detected (but not acoustic-induced) movement.

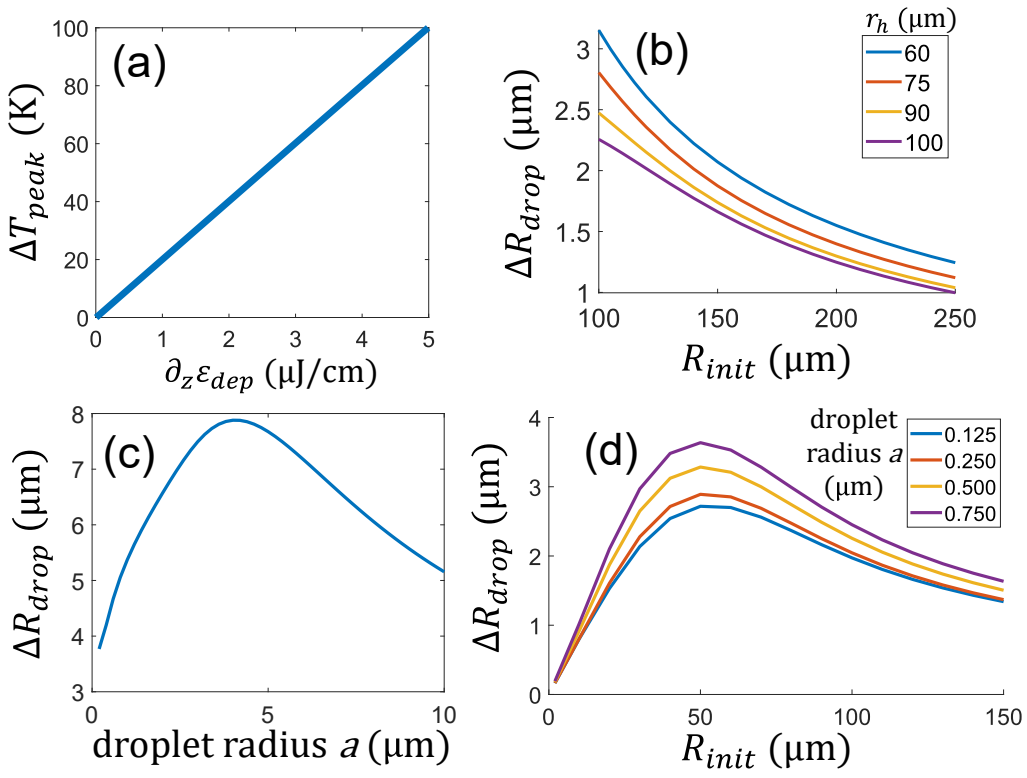

Figure 3.4 (a) Peak temperature rise vs. laser energy deposited per unit length $\partial_z \varepsilon_{dep}$. **(b)** Droplet displacement ΔR_{drop} at 500 µs delay for droplet radius $a = 5\ \mu m$, $\partial_z \varepsilon_{dep} = 4.8\ \mu J/cm$ for various r_h (heated region radius) labelled in the legend. **(c)** ΔR_{drop} at 500 µs delay versus droplet radius a for $\partial_z \varepsilon_{dep} = 4.8\ \mu J/cm$, initial droplet position $R_{init} = 50\ \mu m$, and $r_h = 60\ \mu m$. **(d)** ΔR_{drop} at 500 µs delay versus R_{init} for $r_h = 60\ \mu m$ and droplet radii a = 0.125 µm, 0.25 µm, 0.5 µm, 0.75 µm and $\partial_z \varepsilon_{dep} = 4.8\ \mu J/cm$. ΔR_{drop} decreases for $R_{init} < \sim 50\ \mu m$ because the acoustic wave reaches its maximum amplitude just inside the heated region.

To assess whether the radius of the filament-heated region can affect droplet movement, we performed additional simulations varying r_h, the $1/e^2$ radius of the initial temperature profile. A wider heated region may apply, for example, when laser energy is deposited through rotational excitations [10,82] outside of the highest intensity region of the filament core where optical field ionization primarily occurs. Simulation results plotted in Fig. 3.4(b) for an $a = 5$ µm droplet show that a fixed energy deposition $\partial_z \varepsilon_{dep}$ over a larger radius r_h has reduced effect on droplet displacement, as one might expect from the reduced radial pressure gradient and lower peak fluid velocity. In all cases, the droplet displacement is negligible.

One possibility of interest is whether the acoustic wave can displace much smaller droplets, such as the fragments generated by optical shattering. Figure 3.4(c) plots droplet displacement as a function of droplet radius for $\partial_z \varepsilon_{dep} =$ 4.8 µJ/cm ($\Delta T_{peak} \sim 100$ K from Fig. 3.4(a)) and $R_{init} = 50$ µm (a near-in position where a droplet would normally be optically shattered), where it is seen that the greatest displacement is for droplets with radii in the ~5 µm range of our experiment. While smaller droplets accelerate more due to their smaller masses and larger drag coefficients, overriding the decrease in drag from their lower cross-sections, they also experience a stronger drag deceleration from the background air.

This leads to the overall decrease of ΔR_{drop} as droplet radius decreases below ~5 μm. For droplet radii beyond ~5 μm, ΔR_{drop} decreases because of larger droplet inertia and reduced drag coefficient.

If the initial water droplet is shattered into fragments in a range of radii at different radial positions, Fig. 3.4(d) shows their possible displacements, neglecting the initial fragment velocity upon shattering (which is in all directions [95]). Here, the heated region radius is $r_h = 60$ μm. The smallest fragment simulated (radius $a = 0.125$ μm) is similar to the upper bound radius (0.135 μm) of laser-shattered water droplet fragments estimated in ref. [95]. For fragments of that size, ΔR_{drop} is negligible, and remains small for all fragments in Fig. 3.4(d), ranging to the larger droplets of Fig. 3.4(c). Therefore, we conclude that acoustic clearing is insignificant even for droplet fragments generated by optical shattering.

3.3.2 High-Deposition Experiment

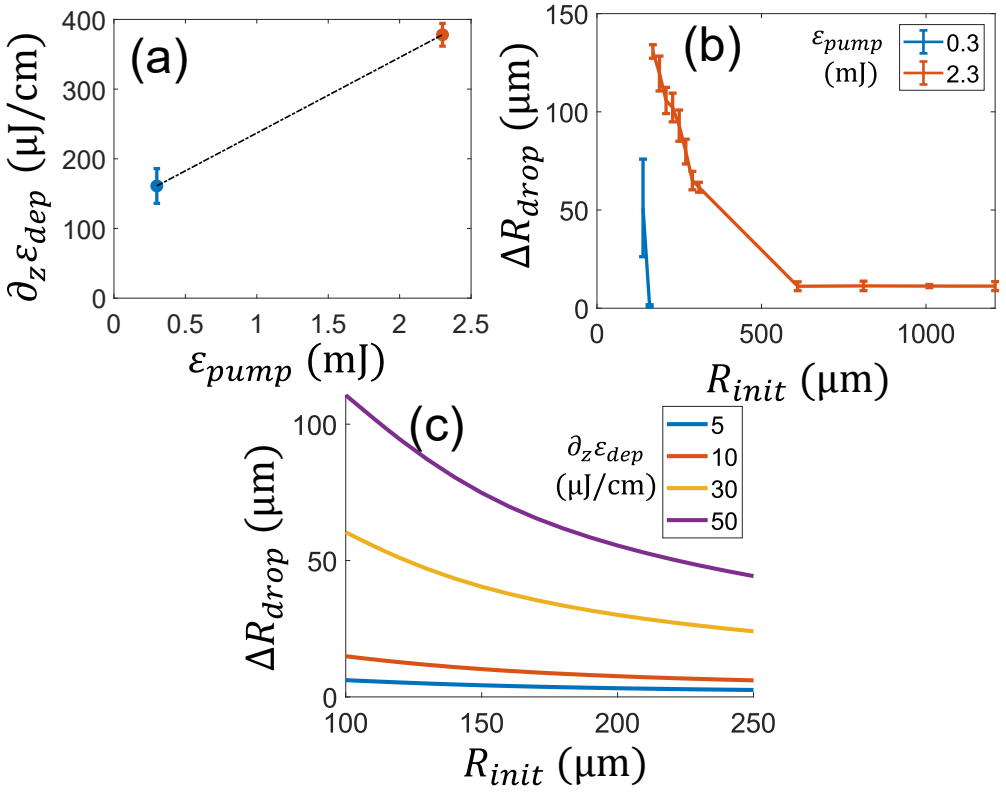

Figure 3.5 (a) Peak energy deposition per unit length for each pump pulse energy. For $\varepsilon_{pump} = 0.3$ mJ, $L \sim 1$ mm, and for $\varepsilon_{pump} = 2.3$ mJ, $L \sim 5$ mm [67]. **(b)** Droplet displacement for each pump energy after 105 μs delay. **(c)** Droplet displacement after 500 μs simulated by the hydrocode for $r_h = 60\ \mu m$ and droplet diameter a ~ 10 μm, for the energy depositions labelled in the legend.

Although there is negligible acoustic clearing of water droplets from a collimated filament, there are non-filamentary conditions where acoustic clearing can be significant. We studied this by using a setup identical to Experiment 2 (Fig. 3.1(b)) except with $f/10$ focusing instead of $f/120$ and with larger water droplets of radius $a \sim 12.5$ μm. This setup produces a smaller heated region (for $\varepsilon_{pump} =$ 2.3 mJ, simulation [67] gives $r_h \sim 45$ μm and $L \sim 5$ mm) with significantly higher energy deposition and higher ΔT_{peak}. In Fig. 3.5(a) the measured $\partial_z \varepsilon_{dep}$ is plotted for two values of ε_{pump}, with absorption of ~380 μJ/cm ($\Delta T_{peak} \sim 5000$ K) at

ε_{pump} = 2.3 mJ, roughly ~100 × higher than $\partial_z \varepsilon_{dep}$ in a filament. In Fig 3.5(b), the measured ΔR_{drop} at 105 μs delay is plotted vs. R_{init}. The displacement driven by a 2.3 mJ pulse is significant, with the droplet moving radially from ~170 μm to ~300 μm. For results more directly comparable to a filament, Fig. 3.5(c) plots results from the hydrocode using a $a = 5$ μm radius droplet and $r_h = 60$ μm as in Fig. 3.3, but higher $\partial_z \varepsilon_{dep}$. The results show that a heated region with the same spatial profile as a filament but with 10 × higher energy deposition can radially displace droplets significantly. For example, when $R_{init} = 150$ μm and $\partial_z \varepsilon_{dep} = 50$ μJ/cm, the droplet displacement is $\Delta R_{drop} = 75$ μm. However, in the deposition range for a filament ($\partial_z \varepsilon_{dep} < 5$ μJ/cm), droplet displacement is only ΔR_{drop} ~4 μm. This result shows that acoustic clearing is constrained mainly by the limited laser energy deposition in a near-IR femtosecond filament generated by collapse of a collimated beam.

We note that there may be self-guided propagation regimes in which acoustic clearing is more effective. For example, our recent simulations of self-guided propagation of 1 Terawatt, $\lambda \sim 10$ μm, 3.5 ps pulses in air [88], show that peak values of $\partial_z \varepsilon_{dep}$ greater than ~100 μJ/cm are achievable from avalanche ionization and heating of ambient sub-micron aerosols by the self-guided pulse. This scenario may apply to recent experiments demonstrating self-guiding of long wavelength infrared pulses over tens of meters [96].

3.4 Conclusions

Self-guiding of short powerful pulses in the atmosphere has been proposed as a

method for clearing atmospheric aerosols in fog for pulses that propagate after them, for applications including optical communications and directed energy. Our experiments and simulations show that for single filaments generated by collimated near-infrared femtosecond pulses, clearing of ~5 μm radius water droplets, typical of fog, is caused mainly by optical shattering for droplets closer than ~200 μm from the filament axis. Under these conditions, the filament reforms and continues to propagate and shatter droplets, clearing a path for a follow-on laser pulse or beam. "Clearing" in this case means reduced scattering losses of the follow-on beam owing to the much smaller radii of the shattered droplet fragments, a transition from Mie scattering to Rayleigh scattering. Droplets outside the shattering radius (>200 μm) undergo varying levels of distortion and cavitation as laser light is internally focused in the droplet, with heating and mass ejection on the far side driving the surviving portion of the droplet back toward the laser, but not cleared from the optical path. Detailed scattering losses from optically shattered droplets would need to be explored experimentally to reach a definitive conclusion on this method's clearing efficacy. We did not consider energy losses from droplet shattering, which by some estimates [97] would make fog clearing with a single near-IR filament over long distances impractical.

We find that acoustic forces are largely ineffective as a droplet clearing mechanism by near-infrared femtosecond filaments, mainly because the filament energy deposition of $< 5\ \mu J/cm$ cannot drive an acoustic wave of sufficient amplitude to move a $5\ \mu m$ droplet more than $\sim 10\ \mu m$ at best. Filament-induced acoustic waves are of little help clearing even the small droplet fragments generated

by optical shattering—these experience offsetting drag forces by the ambient air.

Other fog clearing systems may be worth exploring. Long wavelength infrared (LWIR) filaments with few picosecond pulses [88,96] have large cross-sectional areas and high energies, and heat the air via avalanche ionization and collisional heating. This could lead to larger droplet shattering regions and greater energy deposition for acoustic clearing. LWIR pulses may also induce plasma-free droplet shattering [86], potentially decreasing laser energy losses. Finally, the resonant excitation of molecular rotations using pulse trains [10,82] can deposit energy per unit length exceeding that from plasma generation in a typical near-IR filament, increasing the acoustic wave amplitude and potentially enhancing clearing.

Chapter 4 Long-Distance Air Waveguiding

4.1 Introduction

Whereas Chapter 3 focused on filamentation for fog clearing applications, we now turn to multifilamentation for the purpose of long-distance air waveguiding. The length of the filament, Δz_{fil} , is usually considered to be the axial extent over which the filament core remains sufficiently intense for a particular application, with Δz_{fil} typically orders of magnitude greater than the effective Rayleigh range $z_0 \sim \pi(d_{core}/2)^2/\lambda$ associated with filament core diameter $d_{\mathrm{core}} < \sim 200$ μm, where λ is the laser central wavelength. For collapse and filamentation of a nearly collimated beam of diameter d_{beam}, the filament length is governed by the confocal parameter of the overall beam, $\Delta z_{fil} \sim 2z_0 \sim 2\pi(d_{beam}/2)^2/\lambda$ [28], or $\Delta z_{fil} \sim z_0$ if the filament-forming beam starts at its waist as in our experiments. Therefore, filaments generated by centimeter diameter beams can be several hundred meters long; such extended distances are of high interest for applications.

While femtosecond filaments in air can deliver high peak intensity over extended distances, leading to many of the applications cited earlier, the energy in a filament core is self-limited to approximately the millijoule level: $\varepsilon \sim I_{\mathrm{core}} d_{\mathrm{core}}^2 \tau < \sim 1$ mJ, using the parameters from above and pulse duration $\tau \sim 100$ fs. For example, a laser with a 1 kHz repetition rate could deliver only ~1 W of average power in a single filament core. From the perspective of high average power applications, this is a severe limitation.

There is one aspect of filamentation, however, that can be harnessed to enable delivery of very high average laser powers over extended distances in air: its ability to imprint, via localized air heating, very long-lived optical waveguide structures [54]. This occurs using the filament air-heating process described in Chapter 1 to imprint an air pressure spike extending for the full length of the filament. The pressure spike launches a single-cycle cylindrical acoustic wave which radially propagates away after a few microseconds, leaving a long lifetime density depression, or "density hole", on axis [47,57]. The density hole lasts several milliseconds, characteristic of the thermal diffusion timescale of air. An array of such holes can form a guiding structure for a secondary laser pulse.

In our work first demonstrating the principle of the air waveguide [54], we showed that an array of 4 filaments, generated by the 4 lobes of a TEM_{11} beam, could form an air waveguide structure in two timescale regimes. In the short timescale "acoustic" regime, lasting several hundred nanoseconds, the on-axis collision of the acoustic waves from the 4 filaments forms an increased air density waveguide core. The acoustic waves then propagate away over several microseconds leaving 4 density holes. In the long timescale "thermal" regime, lasting up to several milliseconds, the density holes merge circumferentially by thermal diffusion to form an effective "moat" or cladding around the unperturbed air at the centre of the beam. The central unperturbed air forms the air waveguide core. The 4-lobed TEM_{11} mode was formed by an effective binary phase mask, where alternating segments impose a relative spatial phase shift of π. The resulting

waveguides were 70 cm long and guided an injected probe pulse with spot size ~150 μm.

In this chapter, we demonstrate optical guiding in the longest thermal regime air waveguides generated by far, 45 m in length. From the confocal parameter scaling of filament length discussed above, this required filamentation of a beam with d_{beam}~6 mm. At the same time, to form an effective air waveguide cladding, such a beam should form a sufficient number of filaments on its periphery to ensure circumferential coverage. To accomplish this, we took a different approach from the use of binary phase masks [54]; here we use a smooth Laguerre-Gaussian LG_{01} mode to initiate random filamentation in the donut ring. While a n-segment binary phase mask can, in principle, seed filaments at each of the n beam lobes imposed by the mask, in practice it is difficult to ensure that the lobes have equal energy and locally smooth phase fronts. By contrast, we demonstrate a method to produce a high energy, high quality Laguerre-Gaussian LG_{01} "donut" or "phase vortex" mode so that filamentation is seeded with low level intensity or phase noise that is more uniformly distributed across the mode. Unlike with a binary phase mask, the number of filaments automatically scales with beam size provided that the local laser fluence remains constant, ensuring circumferential coverage of the generated cladding. Furthermore, an LG beam propagates as a single mode with a well-defined Rayleigh range, the distance over which its peak intensity drops by a factor of two owing to diffraction. By contrast, a beam generated by a high order binary phase mask is highly multimodal with much greater diffractive spreading. In prior work, multi-filamentation of Laguerre-Gaussian vortex beams has been studied

theoretically and experimentally in [65,66,98], showing that filaments form on a ring at the radius of highest intensity. In addition, filament arrays have been generated with amplitude or phase masks [63,99].

4.2 LG_{01} Beam Requirements for Air Waveguide Generation

The electric field of a LG_{01} vortex mode is $E_{01}(r,\varphi,z) = \sqrt{eF_0}\,(w_0/w(z))(\sqrt{2}r/w(z))e^{-i2\tan^{-1}(z/z_0)}\,e^{-ikr^2/2R(z)}e^{-(r/w(z))^2}e^{i\varphi}$, where F_0 is the peak fluence (J/cm^2) in the mode's ring, and where $w(z) = w_0(1 + (z/z_0)^2)^{1/2}$, $R(z) = z(1 + (z_0/z)^2)$, and $z_0 = \pi w_0^2/\lambda$ are the mode's spot size, phasefront curvature, and Rayleigh range, respectively, where w_0 is the spot size ($1/e$ field radius) at the beam waist ($z = 0$). The mode's peak fluence lies on a ring of diameter $d_{ring} = \sqrt{2}\,w(z)$. Because the LG_{01} beams of this experiment are highly collimated (propagation range $z < z_0$), we consider $d_{ring} \cong \sqrt{2}\,w_0$ and $z_0 \cong \pi d_{ring}^2/2\lambda$ for making estimates when designing waveguides, analogous to the beam diameter d_{beam} referenced in the introduction.

An interesting aspect of vortex beam filamentation is that the beam ring self-focuses to a narrow shell before filaments nucleate, as borne out by our measurements and simulations shown later. This contrasts with a non-vortex beam where filaments can grow throughout the beam cross section. For an LG beam, filaments are thus located on a well-defined ring, ideal for air waveguide generation. This suggests that for fixed F_0, the number of filaments will scale as the ring circumference ($\propto d_{ring}$). Indeed, for peak laser fluence F_0 in the LG_{01} pulse of energy ε_{LG}, the number of filaments formed is

$$n_{fil} \sim 1.2\,(\varepsilon_{LG}/\varepsilon_{cr})^{1/2} = 1.8\,(F_0/\varepsilon_{cr})^{1/2}\,d_{ring} \qquad (4.1)$$

where $\varepsilon_{cr} \sim P_{cr}\tau$ and $P_{cr} \sim \lambda^2/2\pi n_0 n_{2,eff}$ [100] are the critical energy and power for self-focusing collapse for a small section of the LG_{01} ring containing energy ε_{cr}, and where Eq. (4.1) is adapted from ref. [66]. The critical power ranges over $P_{cr} = 13\ \text{GW} - 3\ \text{GW}$ for laser pulsewidths $\tau = 45 - 300$ fs used in these experiments. This stems from the pulsewidth dependence of the effective nonlinear refractive index, $n_{2,eff} \sim 0.8 - 3.8 \times 10^{-19}\ \text{cm}^2/\text{W}$ in this range, owing to the delayed molecular rotational nonlinearity [77]. For example, for one set of our experimental parameters chosen for generating long waveguides with good azimuthal filament coverage ($d_{ring} = 0.45$ cm, $\varepsilon_{LG} = 90$ mJ, $F_0 = 0.21\ \text{J/cm}^2$, $\tau = 100$ fs), the expected number of filaments is $n_{fil} \sim 20$.

Considering the air waveguide as a step index fibre with V parameter [101] $V = (2\pi a/\lambda)(n_{co}^2 - n_{cl}^2)^{1/2}$ enables an estimate of the cladding air density reduction needed for guiding. Here $a = d_{ring}/2$ is the waveguide core radius and the core and cladding refractive indices are $n_{co} = n_0 + \delta n_{co}$ and $n_{cl} = n_0 + \delta n_{cl}$ respectively (n_0 is the unperturbed air refractive index), with $\delta n_{cl}/n_0 \ll 1$ and $\delta n_{co} = 0$ for a thermal waveguide. The condition for guiding of a lowest order mode is then $V \approx \sqrt{2}\pi(d_{ring}/\lambda)|\delta n_{cl}|^{1/2} > 2.405$ [54], so that the minimum air index reduction in the cladding is $|\delta n_{cl}| \sim 10^{-8}$. This extremely small index decrement is reflective of the large waveguide core size $a \sim 2$ mm, but it is unrealistic: it is significantly smaller than the index fluctuation associated with our measured lab air turbulence level of $C_n^2 = 6.4 \times 10^{-14}\ (\text{m}^{-2/3})$ [53], which gives

$|\delta n_{turb}| \sim 10^{-7}$ across the air waveguide core. If we impose the conservative condition $|\delta n_{cl}| = 10\,|\delta n_{turb}|$ so that the cladding moat depth greatly exceeds the turbulence fluctuation level, the relative air density reduction in the cladding (or refractive index contrast) should be $|\Delta N_{cl}|/N_0 = |\delta n_{cl}|/(n_0 - 1) > \sim 0.4\%$.

Under our conditions, the maximum relative depth of a filament-induced density hole after recombination and thermalization is $\Delta N_h^{max}/N_0 \sim 1 - T_0/T_h \sim 0.25$, where $T_0 \sim 300\text{K}$ is ambient air temperature and $T_h \sim 400\text{K}$ is the typical peak temperature of the density hole [57]. The hole depth slowly declines by thermal diffusion according to $\Delta N_h(t)/N_0 \sim (\Delta N_h^{max}/N_0)(1 + 4\alpha t/R_0^2)^{-1}$, where $\alpha = 0.20\ \text{cm}^2/\text{s}$ is the thermal diffusivity of air and $R_0 \sim 100\ \mu\text{m}$ is the initial density hole radius [57]. Thus, the depth of a density hole will decline from 0.25 to 0.004 over a time $t \sim 10$ ms, giving a good estimate of our thermal waveguide cladding lifetime, as we will see from later comparison with experiment.

The remaining question is whether there is adequate azimuthal cladding coverage by the thermally diffusing density holes. This is what determines the LG_{01} mode energy needed for the filaments leading to cladding formation. After $\sim 1\ \mu\text{s}$ of delay, the density hole widens by thermal diffusion [57], giving $R_h \sim R_0(1+4\alpha t/R_0^2)^{1/2} \sim 1$ mm by $t = 10$ ms, so the density hole spacing Δx_{fil} should be ~ 1 mm at most. For example, for $d_{ring} = 4.5$ mm, the number of

filaments needed around the LG_{01} ring is $n_{fil} \sim \pi d_{ring}/\Delta x_{fil} \sim 15-25$ for $\Delta x_{fil} \sim 0.5-1$ mm, which is consistent with the earlier estimate using $\varepsilon_{LG} \sim 90$ mJ. This informs the energies used in the experiments, as discussed below.

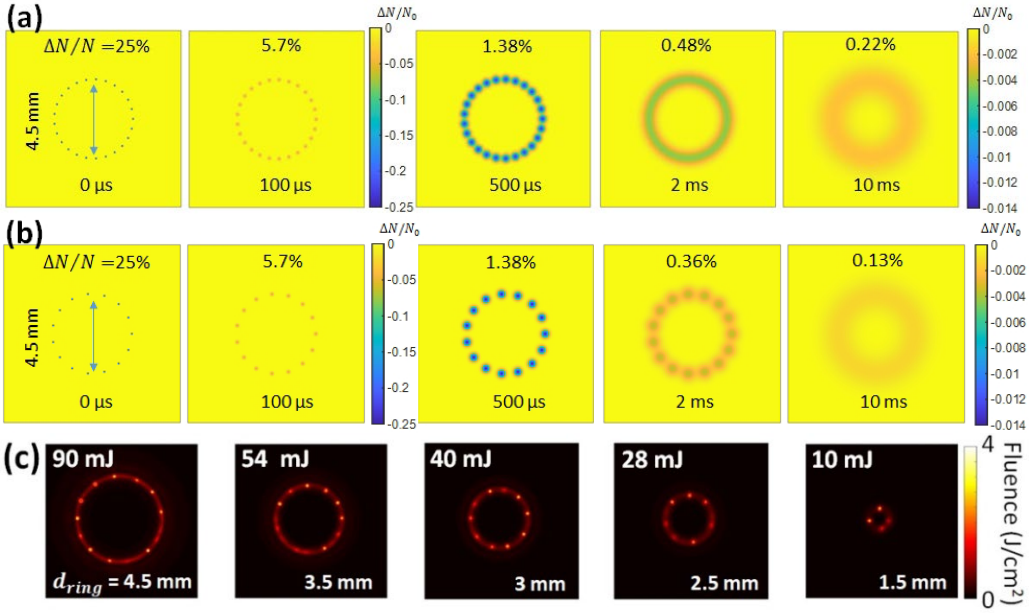

Figure 4.1 (a) Thermal response of air to a ring array of 25 filament-initiated density holes of initial depth $|\Delta N|/N_0 = 0.25$ and peak temperature increase $\Delta T = 100K$. With increasing delay the density holes merge by thermal diffusion to form a nearly continuous cladding moat around the central unperturbed air density core. **(b)** same as (a), except for 15 filament-initiated density holes. **(c)** 3D+1 UPPE propagation simulation (see Sec. 1.4.2) of the onset of filamentation of 100fs LG_{01} pulses of varying diameter and energy for constant initial peak fluence $F_0 = 0.21\, J/cm^2$. The LG_{01} pulses were initialized using a white noise amplitude mask with fluence standard deviation $0.01F_0$ to seed filament nucleation.

Figure 4.1(a) shows hydrodynamic simulations [54,57] of thermal diffusion for cases of $n_{fil} = 25$ and $n_{fil} = 15$ filament-induced density holes spread uniformly on a 4.5 mm diameter ring in air. The initial energy deposition for each filament is taken to be a Gaussian with $1/e$ radius $R_0 = 50$ μm, with temperature increase $T_h - T_0 = 100$ K, giving initial density hole depth $\Delta N_h^{max}/N_0 = 0.25$ (as discussed earlier). This matches typical filament conditions [57]. It is seen that by ~1 ms, the density holes have sufficiently merged to form a nearly continuous

cladding "moat" surrounding the unperturbed air core. Even out to delays of 10 ms, $|\Delta N_{cl}|/N_0 \sim 0.22\%$ indicates that reasonable guiding confinement could be expected based on the conservative estimate made earlier in this section. As will be seen, this is borne out in our guiding experiments. Owing to the much wider waveguides produced in the current experiment, their lifetime is expected to be considerably greater than the millisecond duration of the ~ 200 μm wide guides of our earlier work [54].

Figure 4.1(c) shows a sequence of 3D+1 (3 space dimensions plus time) UPPE simulations ([57,83]) of the filamentation of 100 fs LG_{01} pulses for several beam waists $w_0 = d_{ring}/\sqrt{2}$, with pulse energy scaled to maintain constant initial peak fluence F_0. In each case, the pulse was propagated to the onset of filamentation. The LG_{01} pulses were initialized with a white noise amplitude mask with a fluence standard deviation of 1% of F_0 to seed filamentation. It is seen that the LG_{01} ring self-focuses to a narrow shell before filaments nucleate. For each beam size, repeated simulations with different white noise masks of the same standard deviation show a similar number of filaments. For increasing d_{ring} with F_0 constant, the simulations show that $n_{fil} \propto \sqrt{\varepsilon_{LG}}$, in agreement with ref. [66] and Eq. (4.1). For $d_{ring} = 4.5$ mm, $n_{fil} = 15 - 20$, in reasonable agreement with the estimate based on Eq. (4.1).

To conclude this section, it is worth explaining why an LG_{0m} mode with $m = 1$, rather than $m > 1$, is preferred for generating a ring of filaments. Practically, a LG_{0m} mode is generated by passing a Gaussian beam of spot size w_0 through an m^{th} order spiral phase plate. For a given pulse energy ε_{LG}, the peak fluence in the

LG_{0m} ring is $F_0 = (2\varepsilon_{LG}/\pi w_0^2)g(m)$, where $g(m) = (m/e)^m/m!$ is a decreasing function of m: for example, $g(1)/g(5)\sim 2$. So an LG_{01} mode provides the highest ring fluence F_0 for a given laser energy. In addition, higher order vortex modes diverge faster: $\Delta\theta_{0m} = \sqrt{m}\,\Delta\theta_{01}$, where $\Delta\theta_{0m}$ is the angular divergence of the ring in an LG_{0m} mode.

4.3 Experimental Setup

Our air waveguide experiments were separated into medium range (< 8 m, in-lab) and longer range (< 50 m, in hallway outside lab) experiments depicted in Figs. 4.2(a) and 4.2(b). Filaments for the air waveguide were generated using a 10 Hz Ti:Sapphire laser system with λ_0 = 800 nm and pulsewidth $\tau = 45 - 300$ fs (FWHM), with the pulsewidth adjusted using the grating compressor. The air-waveguided probe was a λ_0 = 532 nm, $\tau \sim 7$ ns, 1 mJ pulse from a frequency-doubled Nd:YAG laser. Filaments were generated with post-compression energies up to 120 mJ (up to 2.7 TW peak power), controlled by a $\lambda/2$ waveplate and a thin film polarizer (TFP).

The key diagnostics for the in-lab experiments (Fig. 4.2(a)) were a translatable helium cell-based imaging system [26,79] and a microphone array [53]. Filaments from the air side of the helium cell were terminated over a $< \sim 4$ mm air-to-helium transition in the cell's slow-outflow nozzle (see Fig. 4.2(a)), owing to the $\sim 20\times$ lower nonlinear refractive index of helium compared to air [103]. This enabled direct in-flight linear imaging, through the helium cell, of LG_{01} beam filamentation and guided mode evolution along the 8 m propagation path. The microphone array,

consisting of 64 equally spaced, synchronized microphones spanning 126 cm, was used to map axial energy deposition profiles of the beams generating filament waveguides. The array measured 126 cm long single shot records of the filament energy deposition per unit length, which were concatenated over the full filament propagation path [53]. The local filament energy absorption drives the generation of air density holes, which form the air waveguide cladding.

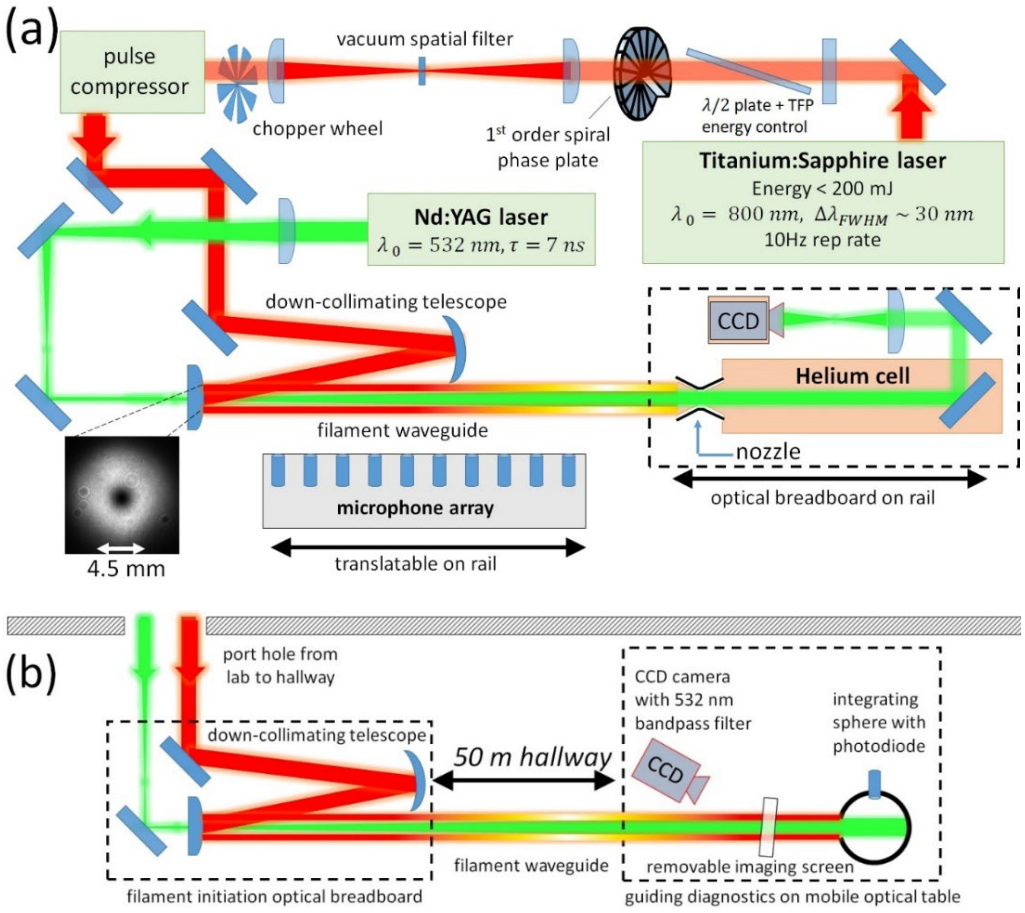

Figure 4.2 (a) Experimental setup for 8 m in-lab guiding experiments. **(b)** Setup for 50 m hallway guiding experiments. The alumina ceramic imaging screen was used for guided mode measurements for the λ = 532 nm, 7 ns, 1 mJ probe pulse (Fig. 4.8). The integrating sphere was used in guiding lifetime measurements using a CW λ = 532 nm probe beam (Fig. 4.9). The CCD camera and integrating sphere used 532 nm interference filters.

The high energy LG_{01} donut mode used to form air waveguides is generated by passing the pre-compressor laser pulse through a 16-step first order spiral phase plate (2π azimuthal phase shift around the beam) followed by a vacuum spatial filter to smooth the beam, removing high spatial frequency nonuniformities including those introduced by the phase plate steps. The destructive interference at the center of the phase spiral generates the amplitude null (or "hole") of the LG_{01} mode. Applying the spiral phase to the pre-compression beam eliminates nonlinear phase accumulation in the phase plate (Another method for high power vortex beam generation is to directly pass the compressed beam through a spiral phase plate provided the beam diameter is sufficiently large [104]). Additionally, the phase plate's chromatic dispersion is too insignificant to impact pulse compression. The resulting beam is then passed through the pulse compressor, followed by a $3\times$ down-collimating reflective telescope (used for both the lab and hallway experiments) to produce a high quality LG_{01} beam whose waist is located at the telescope output. The in-lab experiments used ring diameters of $d_{ring} = 4.5$ mm and 3 mm, giving $w_0 = d_{ring}/\sqrt{2} \simeq 3.2$ mm and 2.1 mm, where w_0 is the e^{-2} intensity radius of the corresponding lowest order LG mode. These corresponds to Rayleigh ranges $z_0 \sim \pi w_0^2/\lambda \sim 40$ m and 17 m. For the hallway, $d_{ring} = 5.6$ mm and $z_0 \sim 60$ m. The aim was to produce "natural" LG_{01} filamentation generated purely by nonlinear self-focusing and without the assistance of external focusing to maximize the beam's Rayleigh range and, therefore, the waveguide length. In both the in-lab and hallway experiments, the green probe laser pulse was injected through the second mirror of the down-collimating telescope and co-propagated

with the waveguide-forming LG_{01} beam. A lens is placed upstream of the telescope mirror in the probe beamline to form a telescope whose effect is a $\sim f/950$ defocus on the probe for injection into the waveguide.

4.4 Results and Discussion

4.4.1 Measurements of LG_{01} Filament Formation

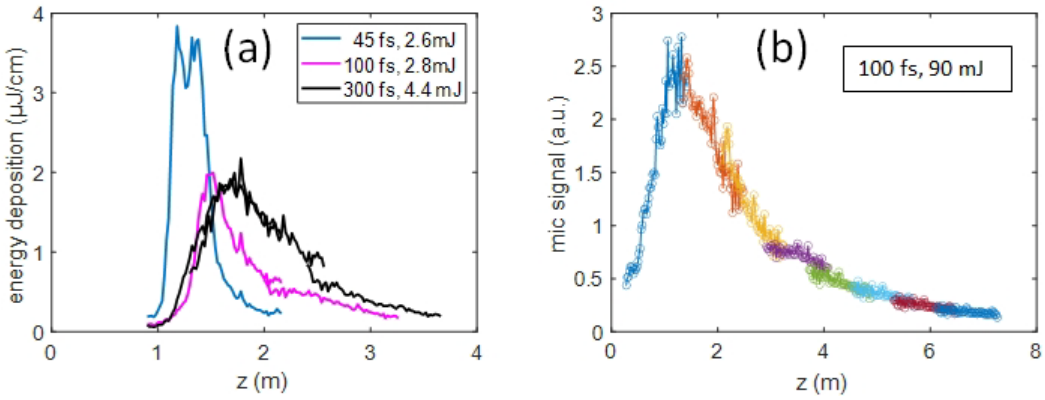

Figure 4.3 (a) Single filament energy absorbed per unit length vs. propagation distance measured by microphone array for laser pulsewidths 45 fs, 100 fs, and 300 fs. Pulse energies were chosen to keep peak power constant at $\sim 6P_{cr}$. Curves are concatenated 126cm longitudinal sections, averaged over 100 shots. The array was 3 mm from the beam axis. **(b)** Acoustic signal from filamentation of 100 fs, 90 mJ LG_{01} pulse. The microphone array was 5 mm from the beam axis. Concatenated and overlapped 126cm longitudinal sections, averaged over 100 shots, are plotted in different colours.

Experiments for air waveguides up to 8 m took place inside the lab with the configuration shown in Fig. 4.2(a). To determine the optimum laser pulsewidth for extended filament generation, we first employed the microphone array to measure the pulsewidth-dependent energy deposition profiles for single filaments generated with Gaussian LG_{00} pulses with $w_0 = 1$ mm ($z_0 = 4$ m). The results are shown in Fig. 4.3(a), where the curves are 100 shot averages of concatenated 1.26 m longitudinal sections. Here the peak pulse power was kept constant at $\sim 6P_{cr}$, accounting for pulsewidth-dependent $n_{2,eff}$ [77]. It is seen that while the peak

energy deposition is highest using shorter pulses, owing to more plasma generation from optical field ionization at the highest intensities, the axial extent of filamentation increases at longer pulsewidths. This originates from the increased contribution of molecular rotation of N_2 and O_2 to $n_{2,eff}$ of air as pulsewidths exceed ~50 fs [77], leading to extended filamentary propagation [105]. Based on these results, we chose 100 fs pulses for the in-lab experiments because their filaments extended ~8 m to the end of the available lab space. Pulse energies in the range 80-90 mJ generated the needed number of filaments (n_{fil}~20) for good azimuthal cladding coverage; filaments begin within 1 m of the down-collimating telescope. Figure 4.3(b) shows the composite microphone array signal from overlapping 1.26 m longitudinal sections over the propagation range of the filamenting LG_{01} pulse, where it is seen that filament energy is absorbed over a range > 7 m.

To capture the onset and formation of filaments in a LG_{01} beam, we used the in-lab translatable helium cell to interrupt propagation and directly image the beam cross-section. Figure 4.4(a) shows single shot beam images from a pulse energy scan at a fixed longitudinal location ($z = 1.5$ m from the down-collimating telescope), using a LG_{01} beam with $d_{ring} = 3.8$ mm to highlight the pre-filamentation phase of propagation. Already with 7.2 mJ, the beam's ring has narrowed, with the clear enhancement of slight beam nonuniformities. The ring width dramatically narrows further as pulse energy increases, with filaments nucleating at the local beam intensity maxima. For a 34 mJ, 45 fs, $d_{ring} = 4.5$ mm beam, Fig. 4.4(b) shows single shot images of increasing multi-filamentation with

propagation up to z~2.6 m, after which the total number of filaments stays roughly constant at n_{fil}~$15-20$, where both bright and fainter (incipient) filamentary hotspots are counted. This is consistent with the n_{fil} estimates made in Sec. 4.2 and the 3D+1 simulations of Fig. 4.1(b). While the filament locations on the ring change shot to shot, their azimuthal distribution remains relatively uniform: this illustrates the advantage of air waveguide generation by a smooth LG_{01} mode over a beam generated by a binary phase plate.

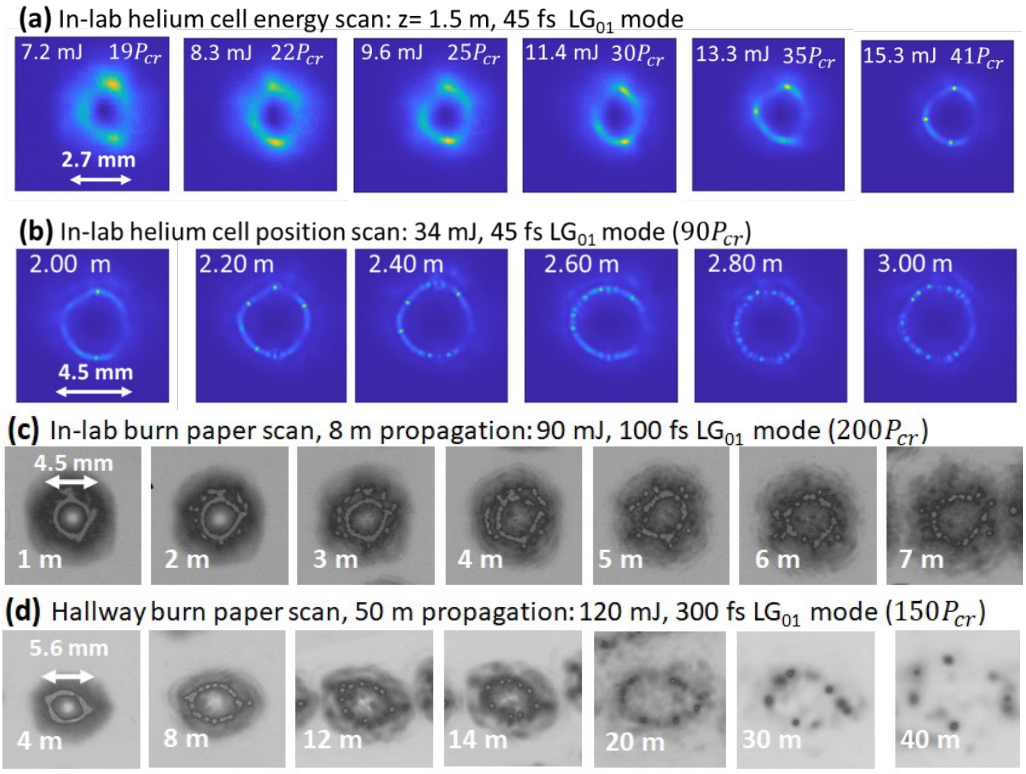

Figure 4.4 (a) Mode images from helium cell of pulse energy scan showing progressive narrowing of LG_{01} ring and nucleation of filaments. The peak pulse power in units of P_{cr} is shown in each image. **(b)** In-lab images from longitudinal scan of helium cell for an LG_{01} pulse with $P = 90P_{cr}$, showing nucleation of filaments and their progressive increase in number. **(c)** In-lab burn paper patterns taken for comparison with helium cell images. **(d)** Hallway burn patterns over length of propagation range.

Additional beam measurements were taken using burn paper, needed for the hallway experiments in the absence of the helium cell. To capture single shots, the

paper was quickly passed through the filamenting beam as it pulsed at the 10 Hz repetition rate of our laser system. To compare with the helium cell images, an in-lab burn paper scan vs. distance is shown in Fig. 4.4(c). The scan qualitatively shows (despite the paper saturation) good azimuthal filament coverage over the 8 m propagation range, consistent with the ≤ 3 m helium cell measurements in Fig. 4.4(b). The hallway burn patterns up to 42 m similarly show good azimuthal coverage, with the number of filaments decreasing at the longest distances owing to the beam intensity decrease from diffractive spreading.

4.4.2 8m Air Waveguiding Experiments

Having confirmed that both the longitudinal energy deposition profile and azimuthal filament coverage of filamenting LG_{01} beams are sufficient to generate very long air waveguides, we now present experimental demonstration of guiding, first over 8 m in the laboratory. Injection of the λ = 532 nm probe pulse into the air waveguide was delayed by 800 μs after LG_{01} multi-filament initiation to ensure that the individual density holes thermally diffused into a relatively continuous lower-density cladding moat. As discussed, the λ = 532 nm probe pulse was coupled into the guide in co-propagating geometry (unlike the counter-propagating geometry of ref. [54]) by passing it through a lens followed by the dielectric curved mirror of the 800 nm reflective telescope (see Fig. 4.2(a)), imposing a diverging phase curvature with Rayleigh length $z_{pr} \sim 60$ cm, equivalent to defocusing at $\sim f/950$.

Use of the diverging probe provided a more rigorous test of the waveguide than a collimated probe, enabling demonstration of guiding over $\sim 13 z_{pr}$ in the lab and

~$70z_{pr}$ in the hallway. For an air waveguide with an index contrast $|\Delta N_{cl}|/N_0 = |\delta n_{cl}|/(n_0 - 1) \sim 0.5\%$ (see prior discussion and Fig. 4.1(a)) and $d_{ring} = 4.5$ mm, $V = 44$ and the numerical aperture is $NA = \lambda V/\pi d_{ring} \sim 1.7 \times 10^{-3}$, supporting coupling f-numbers $f_{\#} = 0.5/NA \sim 300$ or larger. This guide will easily trap and guide our defocusing~$f/950$ probe pulse; such a guide is highly multimodal, trapping $\sim V^2/2 \sim 10^3$ modes [101].

As depicted in Fig. 4.2(a), the guided beam was directly imaged from the helium cell-scanned exit of the air waveguide onto a CMOS camera (through a 532 nm bandpass filter); the guided beam was effectively imaged *inside the waveguide* as a function of propagation distance. Co-propagating supercontinuum light generated by the multiple LG_{01} filaments was attenuated by a bandpass filter and linear polarizer in front of the camera. The camera exposure was temporally gated to eliminate any residual supercontinuum light.

Figure 4.5 shows optical guiding of the probe beam injected at 800 μs delay into an air waveguide formed by an 80 mJ, 100 fs LG_{01} pulse with $d_{ring} = 4.5$ mm, with Fig. 4.5(a) and (b) showing the probe maintaining a constant ~4 mm guided beam diameter over an effective Rayleigh range $\sim 13z_{pr}$. As predicted, these beams are highly multimodal. For the shorter z images in Fig. 4.5(a), one can clearly see the imprints of the circumferential array of density holes on the outside edge of the guided beam. Without the guide present, the probe rapidly diverges. The gap in measurements between $z = 5$ m and 8 m (Fig. 4.5(c)) is due to a gap in helium cell travel constrained by our optical table arrangement.

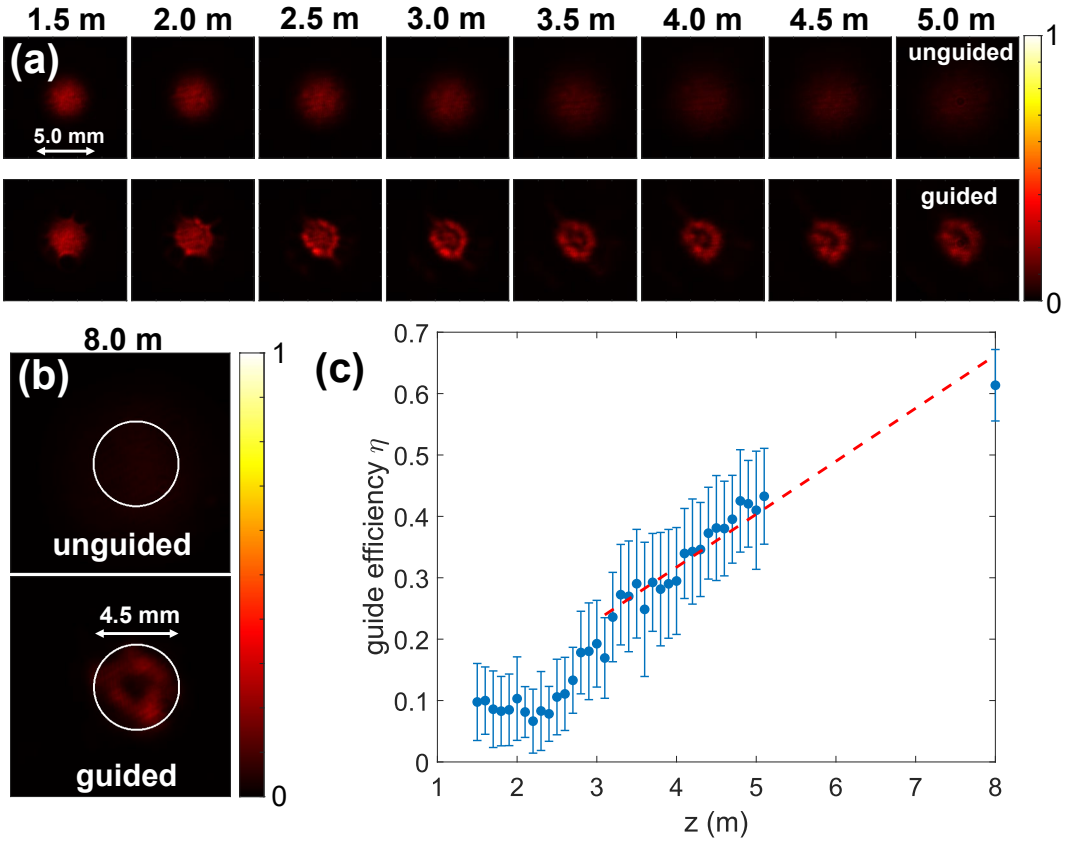

Figure 4.5 Optical guiding of a 1 mJ, 7 ns, λ = 532 nm probe pulse injected at 800 μs delay into an air waveguide formed by a 90 mJ, 100fs LG_{01} pulse with $d_{ring} = 4.5\ mm$. **(a)** 50 shot average images of unguided (top row) and guided (bottom row) mode vs. propagation distance with the same scale as Fig. 4.6(a). The guided mode diameter is a constant ~4 mm. **(b)** Images at $z = 8\ m$ of unguided and guided modes. The $d_{ring} = 4.5\ mm$ diameter circles contain the guided and unguided energy used in the definition of guiding efficiency. **(c)** Guiding efficiency $\eta = (E_g - E_{ug})/(E_{tot} - E_{ug})$ vs. propagation distance, measured with the helium cell. Each point is a 50 shot average, with the bars showing the ± standard deviation. The gap between points at $z = 5.3\ m$ and $z = 8\ m$ is due to helium cell travel constrained by our optical table arrangement. The dashed red line is a linear fit to the points > 3m to guide the eye.

To characterize guiding efficiency, a chopper wheel was inserted to block the waveguide-generating beam (see Fig. 4.2(a)) on every other shot in order to collect sequential guided and unguided probe laser images; 100 consecutive images were saved for every point in Fig. 4.5, and the average of 50 guided and 50 unguided laser shots is displayed. The 100 ms interval between shots is enough that the waveguide from a guided shot will have completely dissipated in time for the

following unguided shot. The guiding efficiency metric defined in our previous work [54] is

$$\eta = (E_g - E_{ug})/(E_{tot} - E_{ug}) \tag{4.2}$$

where E_g and E_{ug} are the guided and unguided energy within the central mode area (that is, with and without the waveguide), and E_{tot} is the total beam energy. The efficiency η ranges from 0 to 1 and gives the fraction of energy retained within the waveguide that would otherwise diffract from within the guided mode area (inside the circle in Fig. 4.5(b)).

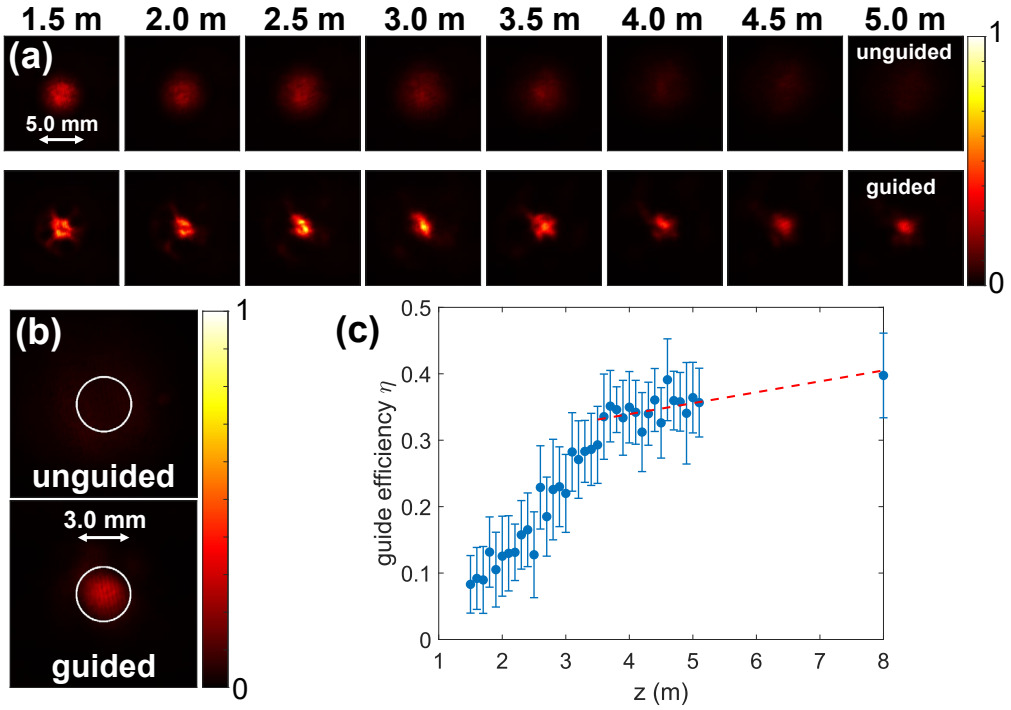

Figure 4.6 Optical guiding of a 1 mJ, 7 ns, λ = 532 nm probe pulse injected at 800 μs delay into an air waveguide formed by a 80 mJ, 100fs LG_{01} pulse with $d_{ring} = 3\ mm$. **(a)** 50 shot average images of unguided (top row) and guided (bottom row) mode vs. propagation distance with the same scale as Fig. 4.5(a). The guided mode diameter is $\sim 2\ mm$. **(b)** Images at $z = 8\ m$ of unguided and guided modes. The $d_{ring} = 3\ mm$ diameter circles contain the guided and unguided energy used in the definition of guiding efficiency. **(c)** Guiding efficiency $\eta = (E_g - E_{ug})/(E_{tot} - E_{ug})$ vs. propagation distance, measured with helium cell. Each point is a 50 shot average, with the bars showing the ± standard deviation. The gap between points at $z = 5.3\ m$ and $z = 8\ m$ is due to helium cell travel constrained by our optical table arrangement. The dashed red line is a linear fit to the points > 3.5 m to guide the eye.

Figure 4.5(c) plots the guiding efficiency η vs. propagation distance for the waveguide. The increase in η with distance results from its definition: as z increases, the unguided mode freely diffracts, decreasing the amount of energy in the central mode area with propagation, whereas the guided mode remains well-constrained within the central mode area. The maximum guiding efficiency of $\sim 60\%$ is comparable to that achieved over < 1 m of guiding in our previous work [54]. Each point is a 50-shot average with the vertical bars showing the ± standard deviation. The fluctuations are dominated by shot-to-shot fluctuations in probe beam energy—the guided mode profiles are very stable, and the 50 shot average images in Fig. 4.5(a) closely resemble those of individual shots.

Results from a smaller diameter air waveguide are shown in Fig. 4.6. Here the waveguide generator was a 70 mJ, 100 fs LG_{01} pulse with $d_{ring} = 3$ mm ($w_0 = 2.1$ mm). The smaller ~2.5 mm guided mode diameter is immediately apparent in Fig. 4.6(a). Because the probe laser geometry is the same as for Fig. 4.5, the guiding efficiency, plotted in Fig. 4.6(b) and peaking at $\sim 40\%$, is smaller consistent with the smaller waveguide numerical aperture.

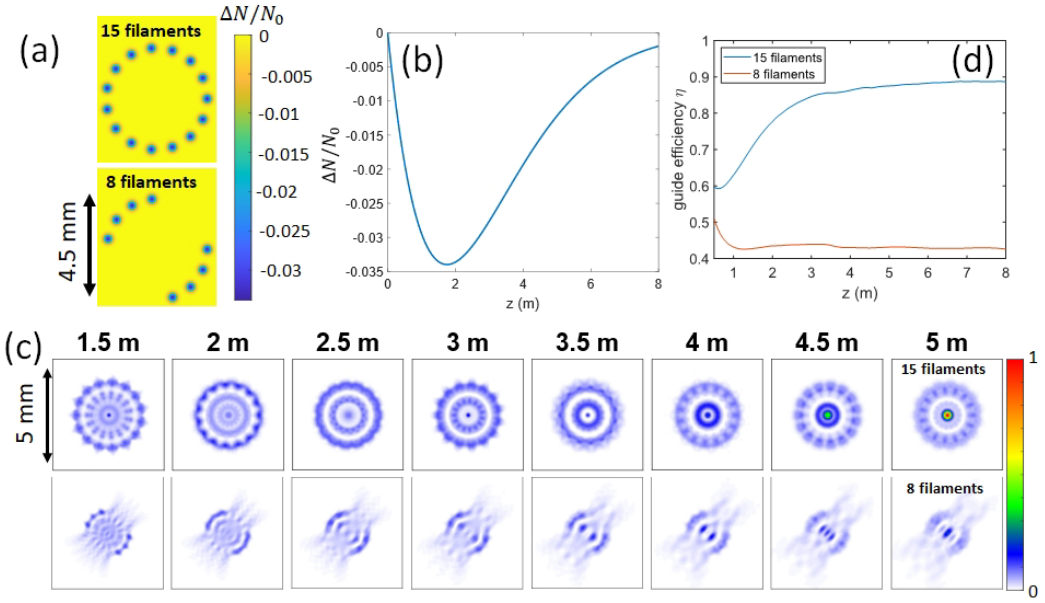

Figure 4.7 Beam propagation method (BPM) [106] simulation of linear λ = 532 nm probe injection and propagation in an 8 m long air waveguide formed by a ring of filament-induced density holes. **(a)** $d_{ring} = 4.5\ mm$ diameter density hole array at 800 μs delay. Peak hole depth is $|\Delta N|_{max}/N_0 = 0.034$. Top panel: 15 filaments. Bottom panel: 8 filaments **(b)** Peak hole depth vs. axial location in guide, scaled from measurements in Fig. 4.3(b). **(c)** Guided mode profile vs distance in waveguide for 15-filament and 8-filament guides. The 15-filament guide is highly multimodal, with $V^2/2 \sim 10^3$ modes. **(d)** Simulated guide efficiency η (Eq. (4.2)) for 15-filament guide and 8-filament guide.

Linear guiding of the diverging $f/950$ $\lambda = 532$ nm probe pulse in our 8 m, $d_{ring} = 4.5$ mm air waveguide is simulated using the beam propagation method (BPM) [106], which computes propagation assuming a time-independent laser field. This is appropriate for our very long-lived air waveguides. Figure 4.7(a) shows the cross sections of two air waveguides at 800 μs delay: one with 15 uniformly spaced density holes, and the other with 8 density holes and two azimuthal gaps. The peak hole depth variation along the guide is plotted in Fig. 4.7(b), scaled using the measurement of Fig. 4.3(b). The guided modes for the 15-hole case are shown in Fig. 4.7(c) (top row), and clearly resemble the experimental images of Fig. 4.5, with similar rings and azimuthal modulations indicative of

multimode guiding in an azimuthally modulated guide. Guided modes for the 8-hole case are shown in Fig. 4.7(c) (bottom row), with significant side leakage through the azimuthal gaps in filament coverage. The corresponding guiding efficiency η is plotted in Fig. 4.7(d) for the 15-hole and 8-hole guides. For each guide, the efficiency falls from $\eta = 1$ at z = 0 because the probe begins smaller than the guide core and therefore $E_{tot} = E_g$. The efficiency decreases as the probe beam diffracts until a significant fraction of beam energy reaches the guide cladding and is constrained. For the 15-hole guide, the efficiency quickly rises from a minimum of ~60% to ~90% and stays at that level, higher than our peak experimental efficiency of ~60% from Fig. 4.5(d). An explanation for this difference is nonuniform azimuthal filament coverage for some sections of the waveguide in the experiment. This is borne out by the simulations: for the nonuniform 8-hole case, the guiding efficiency is significantly reduced owing to the leakage seen in Fig. 4.7(c). Future experiments will be dedicated to optimizing guiding efficiency by improving the azimuthal uniformity of filament coverage.

4.4.3 50m Range Air Waveguiding Experiments

Based on the detailed in-lab investigation described in the prior section, we next demonstrated air waveguiding over ~ 50 m in the hallway adjacent to the lab, using the setup of Fig. 4.2(b). To extend LG_{01} filamentation over this longer range, we used $d_{ring} = 5.6$ mm ($z_0 \sim 60$ m), $E_{LG} = 120$ mJ (keeping the initial laser fluence F_0 nearly constant), and $\tau = 300$ fs (see Fig. 4.3(a) showing longer filaments with longer pulses). In the absence of the helium cell in the hallway, burn paper was used as a spatial profile diagnostic of the LG_{01} filaments. Figure 4.4(d) shows a

sequence of burns up to ~ 42 m, where reasonable azimuthal coverage is seen, with the number of filaments decreasing at the farthest positions owing to a decrease with propagation in the local fluence in the LG_{01} ring. As in the in-lab experiments, the injected probe was a diverging $f/950$, 1 mJ, λ = 532 nm pulse. Guided modes were imaged (through a 532 nm filter) from an alumina ceramic scattering screen variably placed along the propagation range. This method has lower fidelity than the direct imaging through the helium cell, but it allowed capture of the full beam without placing easily damaged optics in the path of the intense filaments.

Given the increased size of the LG_{01} ring and the expected longer waveguide formation timescale and lifetime, we first measured guide efficiency η (at $z = 42$ m) vs. probe pulse injection delay, as plotted in Fig. 4.8(a). An injection delay $\sim 2 - 5$ ms yields the maximum guiding efficiency $\eta \sim 15 - 20\%$. Efficiency vs propagation distance for a 5 ms injection delay is plotted in Fig. 4.8(b). The increase and then decrease of η with delay in Fig. 4.8(a) appears as increasing and then decreasing mode confinement, as shown in the sequence of guided beam images in Fig. 4.8(c), measured at $z = 42$ m. While there is still noticeable beam confinement up to 20 ms delay, by 30 ms the guided and unguided modes are almost indistinguishable owing to thermal dissipation of the guiding structure.

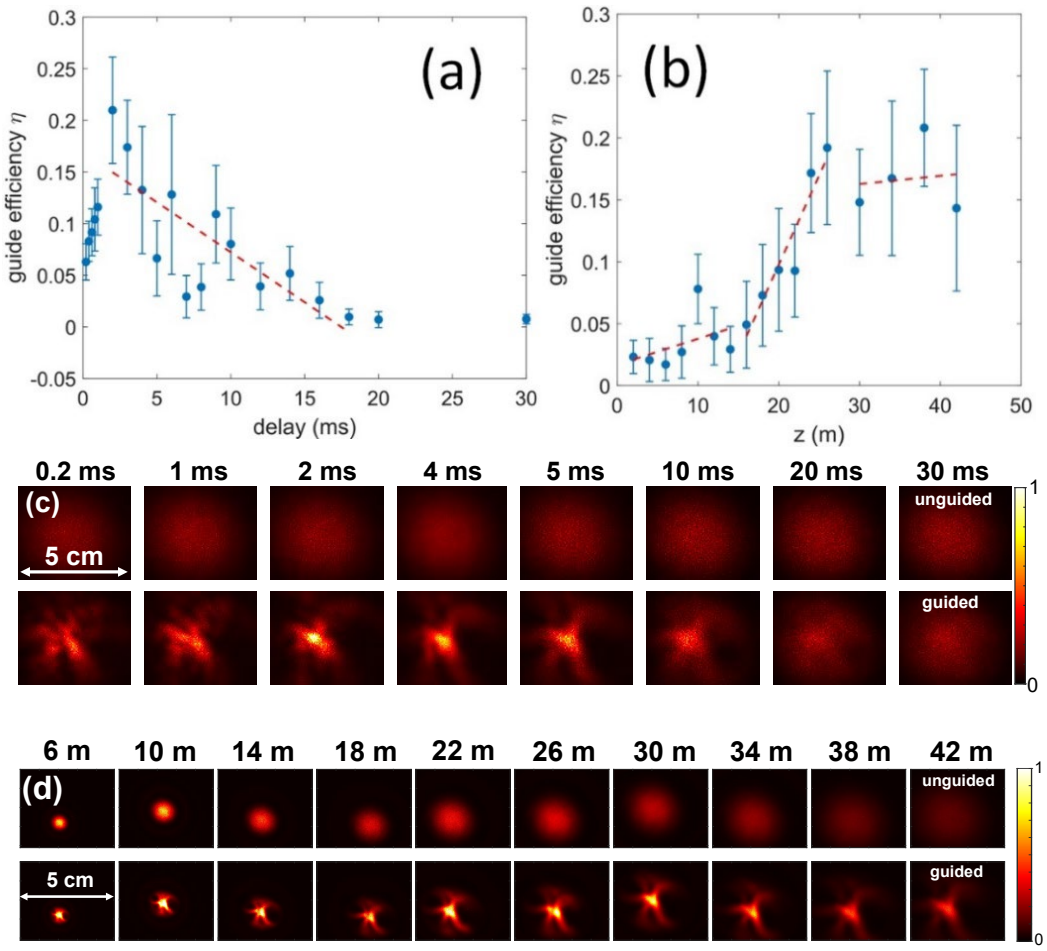

Figure 4.8 Results from air waveguiding in 50 m range. Optical guiding of a 1 mJ, 7 ns, λ = 532 nm probe pulse injected an air waveguide formed by a 120 mJ, 300fs LG_{01} pulse with $d_{ring} = 5.6\,mm$ ($z_0 = 60\,m$). **(a)** Guiding efficiency η vs. probe pulse injection delay, measured at $z = 42\,m$. **(b)** Guiding efficiency η vs. z along waveguide for 5 ms injection delay. Each point in (a) and (b) is a 100 shot average, and the error bars are the ± standard deviation. **(c)** Guided probe modes measured at $z = 42\,m$ vs. injection delay. **(d)** 100 shot average images of unguided (top row) and guided (bottom row) mode vs. propagation distance.

A comparison of guided and unguided modes as a function of longitudinal position is shown in Fig. 4.8(d). As in the in-lab experiments, this is a highly multimodal waveguide. BPM simulations predict efficiency η~50% at $z = 42$ m for a guide with 18 density holes at 5 ms delay on a ring of diameter $d_{ring} = 5.6$ mm, significantly higher than the experiment. As with the 8 m guide experiments and simulations, part of the discrepancy between simulated and

measured efficiency is attributable to nonuniform and sparser azimuthal density hole coverage. This is evidenced by the burn patterns at longer distances in Fig. 4.4(d) and the asymmetric imprint of the density holes on the guided beam edge in Fig. 4.8(d). An additional important factor, especially for the $\sim$50 m propagation experiments, is the probe beam pointing wander of ~200 mrad, primarily from thermal drift in the probe laser and air turbulence. Simulations show that ~200 mrad off-axis injection, into a guide with uniformly distributed density holes, decreases the efficiency to η~25%.

The fact that waveguide efficiency $\eta(z)$ in Fig. 4.8(b) trends to a constant level out to $z = 42$ m is evidence that the guide extends the full 42 m. This is supported by the BPM simulations in Fig. 4.9 of $\eta(z)$ for two lengths (30 m and 42 m) of the 18-density-hole waveguide mentioned above. Figure 4.9(a) shows the prescribed density hole depth vs. z (scaled to measurements of Fig. 4.3(b)) used in the simulations, and Fig. 4.9(b) plots $\eta(z)$ for the two guides. For the 30 m guide, the rapid drop in $\eta(z)$ for $z >$ 30 m stems from the rapid diffractive spreading as the confined mode exits the end of the guide; this spreading significantly exceeds that of the unguided beam. For the 42 m guide, it seen that $\eta(z)$ remains roughly constant for $z > 30$ m as expected and in qualitative agreement with the measurements.

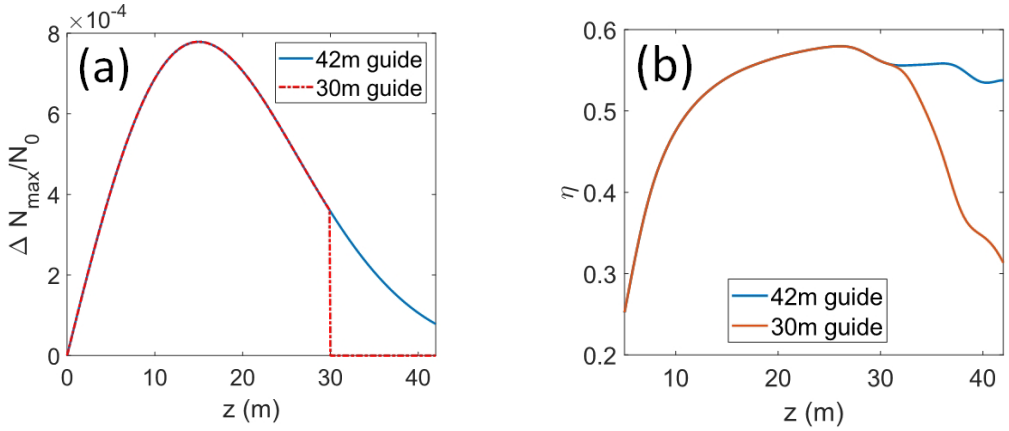

Figure 4.9 BPM simulation of guiding efficiency in 2 lengths of an 18-filament-induced waveguide. **(a)** Prescribed density hole depth vs. z (scaled and stretched in length from Fig. 4.3(b)). For the 30 m guide, the hole depth (and therefore the waveguide cladding depth) is set to zero for $z > 30$ m. **(b)** Guiding efficiency $\eta(z)$ for the two guide lengths.

Finally, as a striking demonstration of the potential quasi-steady-state operation of femtosecond filament-induced air waveguides, we injected a probe beam from a continuous wave (CW) 100 mW, λ = 532 nm laser diode into our long hallway waveguide. The waveguide parameters were the same as for Fig. 4.8. The probe beam was injected along the green beam path shown in Fig. 4.2(b) and was collected at $z = \sim 45$ m by integrating sphere, with a 1.3-cm entrance aperture slightly exceeding the mode size of Fig. 4.8. The goal was to directly measure the guiding lifetime of the waveguide.

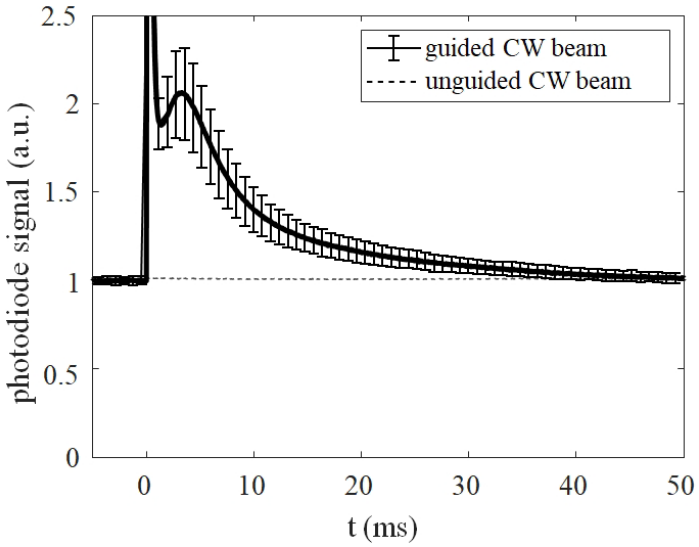

Figure 4.10 Measurement of guiding of a CW probe beam in a ~45 m waveguide. A 100 mW, λ = 532 nm laser diode was injected into the waveguide through the down-collimation telescope mirror (see Fig. 4.2(b)), into the waveguide, and then collected by an integrating sphere at $z = 45\ m$. The waveguide lifetime is directly read off the signal to be tens of milliseconds. Solid curve: 100 shot average. Error bars: ± standard deviation. The first peak is filament-generated supercontinuum collected by the integrating sphere and the second peak reflects maximum guiding efficiency at $\sim 3 - 5\ ms$ delay.

Figure 4.10 plots the average of 100 diode signal traces of the guided beam collected by the integrating sphere, with ± standard deviation bars overlaid on the curve. This shows that measurable guiding over 45 m persists to ~20 ms, declining to a negligible level at >30 ms owing to thermal diffusion of the waveguide. This is consistent with the ≥ 20 ms guided mode images of Fig. 4.8(c). The initial temporal spike in the diode signal is from LG_{01} filament-induced supercontinuum emission that transmits through the 532nm interference filter in front of the integrating sphere. The secondary peak at ~3-5 ms follows the maximum guiding efficiency, corresponding to optimal waveguide cladding performance from diffusive merging of density holes; this is consistent with the peak in Fig. 4.8(a). These results strongly suggest that for similar guide parameters as in Figs. 4.8 and

4.10, a $> \sim 100$ Hz filament-forming laser could maintain a quasi-continuous air waveguide.

4.5 Conclusions

We have demonstrated optical guiding of probe pulses up ~45 m, or 70 Rayleigh ranges, in air waveguides formed from the long-lived thermal response of air to filamenting ultrashort laser pulses. The guide lifetime is tens of milliseconds, showing that a quasi-steady-state air waveguide could be supported by a $> \sim 100$ Hz repetition rate filament-forming laser. The guides are generated using a new method: multi-filamentation of Laguerre-Gaussian LG_{01} "donut" modes, and are more than $60\times$ longer than the guides in our prior air waveguiding demonstration [54] which used a binary phase mask for filament formation. Our results pave the way for a wide range of applications requiring either projection or collection of optical signals in the atmosphere and represent an essential step towards kilometer-scale air waveguides.

The long propagation range experiments, performed in the hallway adjacent to our laser lab, were preceded by more detailed measurements of waveguiding over 8 m (~13 Rayleigh ranges) in the lab. The in-lab experiments verified our new method for waveguide generation: the development of a thin ring of filaments by the LG_{01} mode, which heat the air and form a cladding "moat" surrounding a core of unperturbed air. For the 8 m guides, maximum guiding efficiency was ~60%, and it was ~20% for the 45 m long waveguides. While lower than in the ideal case, these reduced efficiencies are likely due to nonuniform azimuthal coverage by the

ring of filaments. This is directly borne out by simulations, which provide a path for straightforward efficiency improvements in future experiments.

While guiding in this experiment was demonstrated using a relatively weak probe laser pulse, air waveguides can support high peak laser powers and are especially suited to high average powers, limited in the first case by self-focusing and in the second case by thermal blooming. Using the scaling developed in ref. [54], the peak intensity I_p limited by self-focusing is $I_p L_g < 2 \times 10^{14}$ W/cm, where L_g is the guide length. Taking $L_g = 100$ m gives $I_p < 20$ GW/cm^2. For a ~5 mm diameter waveguide and a 10 ns pulse, the guided energy can be 40 J.

For quasi-CW guided beams, thermal blooming can limit the average laser power guided by spoiling the air waveguide structure. However, this will occur only at very large powers when sufficient laser energy is absorbed that the relative on-axis air temperature increase, $\delta_T = \Delta T/T_0$, dominates the waveguide core-cladding density contrast $\Delta N/N_0$. The relative temperature increase for average guided power P_g over a duration Δt is given by $P_g \Delta t/A = 1.5\delta_T \alpha^{-1} p_0$, where p_0 is the ambient air pressure, α is the air absorption coefficient, and A is the waveguide core cross-sectional area. For the ~8 m and ~50 m waveguides of this chapter, a conservative estimate for the typical core-cladding density contrast is $\Delta N/N_0 \sim 0.01$, from inspection of Fig. 4.7(b). Using an absorption coefficient $\alpha = 2 \times 10^{-8}$ cm^{-1}, which accounts for molecular and aerosol contributions in realistic environments [83], a 5 mm waveguide core diameter, and a quasi-CW burst duration of 5 ms, gives an estimated thermal-blooming- limited guided energy of $P_g \Delta t \sim 15$ kJ and peak average power limit $P_g \sim 3$ MW.

For applications such as distant projection of high average powers or remote collection of optical signals [107], kilometer-length and longer air waveguides may be of interest. The laser requirements for their generation can be obtained from scaling the results of our experiments. Because filamentation occurs over approximately a Rayleigh range of the driving beam, an LG_{01} beam of diameter $d_{beam} \sim 2w_0 = 3.2$ cm and sufficient power will generate filaments over ~1 km. Each filament is much shorter than this, owing to the interaction of the filament with its local laser energy "reservoir", with some filaments decaying and others starting at multiple locations along the propagation path, but remaining, on average, uniformly spaced on the ring. Based on our ~ 50 m experiments, which used 120 mJ, 300 fs LG_{01} pulses with $d_{ring} = 0.56$ cm ($d_{beam} \sim 2w_0 = 0.79$ cm), a 1 km air waveguide using $d_{beam} = 3.2$ cm would need $\sim (3.2/0.79)^2 \sim 16\times$ more energy, or ~ 2 J, to maintain the fluence and keep the spacing between filaments on the ring approximately the same. Our prior measurements [28] have established average single filament energy deposition of $\sim 0.25 - 0.5$ μJ/cm in the extended propagation range of a filament. Therefore, for each density hole generated by filaments on the ring, an average $\sim 0.025 - 0.05$ J is needed over 1 km. A 2 J LG_{01} pulse could then support ring coverage of $\sim 40 - 80$ filaments to form a waveguide cladding over ~ 1 km.

Chapter 5 Quasi-steady-state Air Waveguiding

5.1 Introduction

While Chapter 4 focused on long-distance air waveguides at 10 Hz, this chapter turns to short distance guiding with a focus on generating air waveguides at higher repetition rates that do not dissipate. In Chapter 4, we demonstrated air waveguiding over ~50 m, with guide lifetimes of ~20-40 ms limited by thermal diffusion of the imprinted waveguide cladding [55]. A path to quasi-steady-state air waveguiding was thus provided by [54,55], made possible by the detailed understanding of gas dynamics induced by high-repetition-rate filamentation [28,47,57,75,108]. It was shown that high-repetition-rate filamentation can "build up" density holes to a steady state value limited by thermal diffusion, and that this long-timescale heating leads to buoyant effects, deflecting subsequent filaments with the resulting vertical density gradient. The density hole build up can lead to deeper density holes that never dissipate, a desirable effect for CW beam guiding. This chapter uses this effect to demonstrate quasi-steady-state air waveguiding using kHz repetition rate filamentation for generating and sustaining the waveguide.

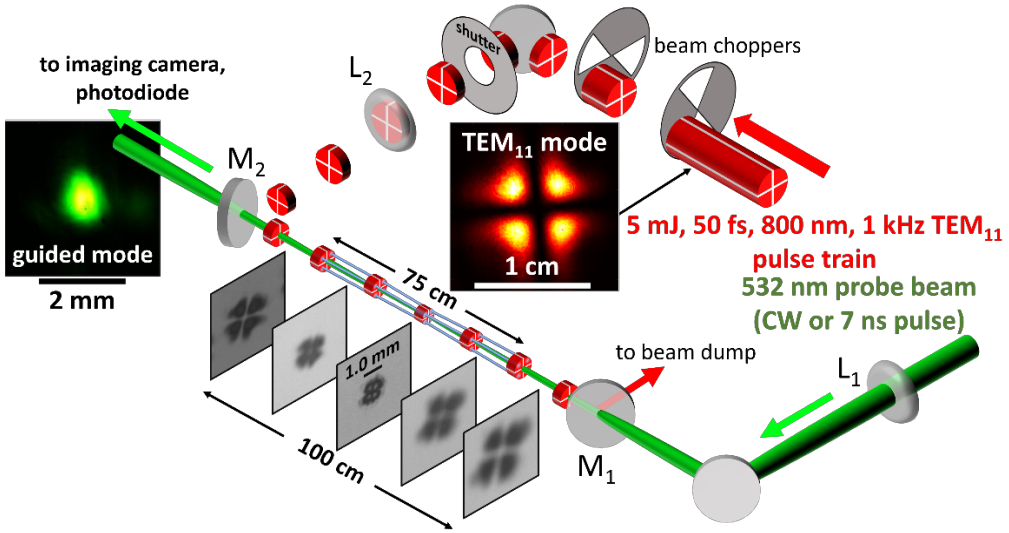

Figure 5.1 Air waveguiding experiment. M_1/M_2: dielectric mirrors to reflect 800nm and transmit 532nm. L_1: lens for f/200 injection of CW probe into guide. L_2: lens for f/250 focusing of the filamenting TEM_{11} beam.

The experimental setup is depicted in Fig. 5.1. The air waveguide is generated at repetition rates 10-1000 Hz by filamentation of Ti:Sapphire laser pulses in a (4-lobed) TEM_{11} mode, produced by passing a near-Gaussian beam through a four-segment binary phase plate, followed by a spatial filter. The pulses are focused by lens L_1 in air at f/250, forming ~75 cm long filaments, after which the $\lambda = 800$ nm light is removed from the beam path by dielectric mirror M1. The filament repetition rate is controlled by two chopper wheels in the path of the 1 kHz repetition rate laser, and a millisecond risetime shutter is used for burst mode experiments. Each lobe of the TEM_{11} mode is $\sim 3P_{cr}$ (critical power for self-focusing) in air [78]. Burn paper was used to monitor filamentation of the TEM_{11} pulse over its propagating path, with burn images shown in Fig. 5.1. The diagonal filament separation near the beam waist is ~500 μm, so that the waveguide core

diameter is ~200 μm after ~0.5 ms of thermal diffusion and merging of the four filament-induced density holes to form the cladding [54]. Optical guiding is measured by injecting at $f/200$ a counter-propagating, spatially filtered green ($\lambda = 532$ nm) laser beam into the air waveguide. Either a pulsed ($\tau \sim 7$ ns) 10 Hz Nd:YAG source is guided and imaged at the waveguide exit onto a CCD camera or a continuous wave diode (4.5 mW) is guided and directed into an integrating sphere with a photodiode. The integrating sphere entrance is apertured with an adjustable iris to maximize the ratio of guided (waveguide on) to unguided (waveguide off) beam signal at each filament repetition rate. This ensures that the waveguide-on signal originates from the waveguide core.

5.3.1 Guiding Efficiency and Repetition Rate

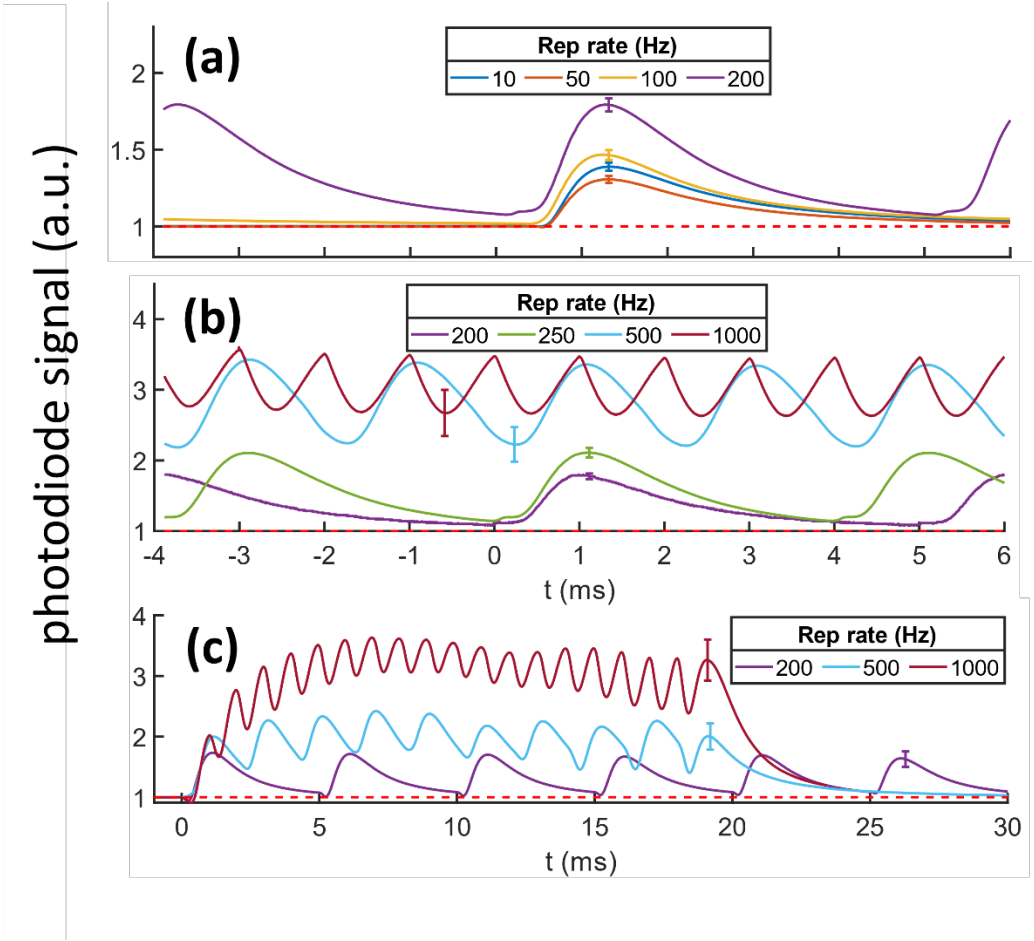

Figure 5.2 Integrating sphere photodiode traces of air-waveguided probe beam. All curves are 200 trace averages. Error bars shown are the standard deviation over individual traces. The dashed red line is the waveguide-off photodiode signal, normalized to unity. **(a)** Repetition rates 10-200 Hz **(b)** Transition to quasi-continuous operation over repetition rates 200-1000 Hz. **(c)** Probe signal showing air waveguide buildup from $t = 0$ in burst mode at 200 Hz, 500 Hz, and 1000 Hz.

The effect of filament repetition rate is shown in Fig. 5.2. For 10 Hz through 100 Hz, the guided signal decays over ~4 ms from its peaks to the waveguide-off level (red dashed line) before the next TEM_{11} pulse arrives. This decay time for ~200 µm core diameter guides is consistent with our previous measurements and calculation [54,55,57] of the decline of the core-cladding index contrast by thermal diffusion in air. Beyond 200 Hz, the guided beam signal is always higher than the

waveguide-off level, indicating the transition to a quasi-continuous air waveguide. As seen in Fig. 5.2(b), improved guiding is observed at higher repetition rates, with a large increase in guided signal between 200 Hz and 500 Hz. While the peak values of the 1 kHz signal are similar to those at 500 Hz, the dips between peaks are reduced at 1 kHz as the guide approaches steady state operation. The increase in guide efficiency is driven by the cumulative deepening of filament-induced density holes at high repetition rate, as first measured in ref. [57], resulting in a deeper cladding and a higher core-cladding index contrast. The effect of an abrupt turn-on at $t = 0$ of the waveguide-generating pulse train is shown in Fig. 5.2(c), where a ~ 1 ms risetime shutter is placed in the TEM_{11} beam. The rapid cumulative growth of waveguide efficiency is clearly demonstrated by the >200 Hz traces.

Figure 5.3(a) shows guided mode evolution for a 1 kHz waveguide during the interval between TEM_{11} pulses (here $t = 0$ corresponds to a peak in the 1 kHz trace in Fig. 5.2(b)). CCD camera images are taken using a 20 μs electronic shutter, much shorter than the thermal evolution of the waveguide, so the contribution of unguided light is negligible. The probe beam is well-confined for all delays, with slight changes in peak intensity and mode size with delay. These variations track well with the photodiode trace oscillations in Fig. 5.2(b) and the expected millisecond-scale thermal evolution of the waveguide core diameter. Based on our measured filament energy deposition and induced density hole depths for single filaments in air [28], we estimate a maximum core-cladding contrast of $\Delta N/N_0 \sim 0.015$ after 500 μs of thermal diffusion, where ΔN is the air density reduction at the cladding and N_0 is the ambient air density in the core. For a waveguide core radius of ~100

μm at 500 μs delay, this gives a V parameter [54,55] of $V\sim3$, indicating nearly monomode guiding, consistent with the Gaussian-like modes measured. Based on scaling in [55], the guided power thermal blooming limit for this 200μm core guide is ~5 kW.

Figure 5.3(b) shows the guided mode for several repetition rates at 500 μs delay. The guide confinement improves significantly with repetition rate, consistent with the increase in photodiode signal in Fig. 5.2. The guide efficiency [54,55] $\eta = (E_g - E_{ug})/(E_{tot} - E_{ug})$ at three delays (300 μs, 500 μs, and 700 μs) is plotted vs. repetition rate in Fig. 5.3(c), where E_g and E_{ug} are the integrated image signals corresponding to the guided and unguided beam (with and without the waveguide), and E_{tot} is the total beam signal. Efficiency increases with repetition rate, up to ~73% at 1 kHz at 500 μs and 700 μs delays. The difference between low repetition rates and high repetition rates is most prominent at 300 μs delay, where the high repetition rate waveguides build upon an already-present guiding structure. By later delays the difference in efficiency is less pronounced, although still present, due to the low-repetition-rate guides forming over those timescales. Fig. 5.2(b) shows a steadily increasing value of E_g/E_{ug} for all delays, however, which isn't shown as strongly in Fig. 5.3(c). This is due to the slightly changing waveguide core size with repetition rate; energy is more tightly confined at higher repetition rates (as seen in Fig. 5.3(b)) due to the presence of a larger, more diffuse, density depression from prior filamenting pulses. Since the core is effectively smaller, E_{ug} decreases, driving up E_g/E_{ug}. By contrast, η simply represents what fraction of energy is in

the waveguide core, whatever its size, so it does not depend on this core size variation across repetition rates.

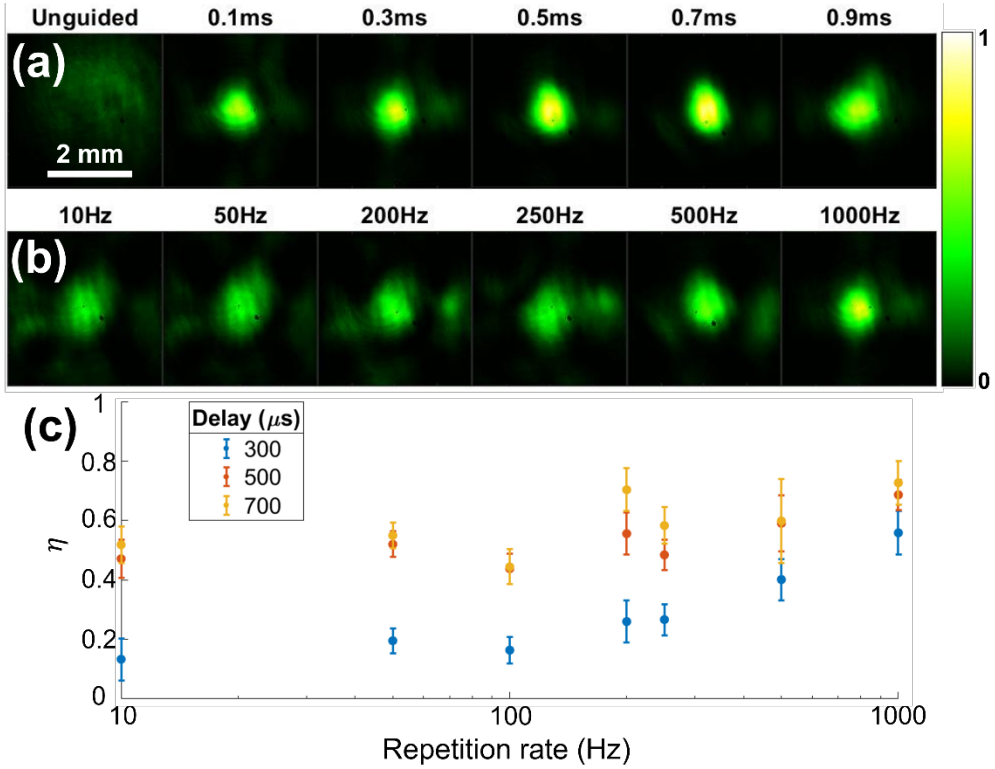

Figure 5.3 (a) Guided mode evolution in the interval between TEM_{11} pulses for a 1 kHz waveguide. **(b)** Guided mode vs. repetition rate at 500 μs delay. **(c)** Guide efficiency η vs. repetition rate for three delays: 300 μs, 500 μs, and 700 μs. Error bars correspond to standard deviations of η.

5.3.2 Waveguide Lifetime

One way to estimate air waveguide lifetime is to calculate how long it takes for the filament-induced density holes to diffuse such that the air density at the waveguide core center equals the air density at the cladding center. A simple way to calculate this is to determine when each density hole adds in the center of the waveguide to equal the depth of each individual density hole. Given thermal diffusion: $R_h(t) = \sqrt{R_0^2 + 4\alpha t}$ and $\Delta N_h(t) = \Delta N_0/(R_h(t)/R_0)^2 = \Delta N_0/(1 + 4\alpha t/R_0^2)$ are the density hole 1/e waist and depth, respectively. Assuming that

density holes are radially gaussian, $\Delta N_h(r,t) = \Delta N_h(t) e^{-\frac{r^2}{R_h^2(t)}} = \Delta N_0/(1 + \frac{4\alpha t}{R_0^2}) e^{-\frac{r^2}{R_0^2+4\alpha t}}$. From this, we can estimate the density at the center of the guide $\Delta N_{core}(t)$ by setting $r = a$, the waveguide radius, then multiplying by the number of filaments n_{fil}: $\Delta N_{core}(t) = n_{fil}\Delta N_0/(1 + \frac{4\alpha t}{R_0^2}) e^{-\left(R_0^2+4\alpha t\right)^{-1} a^2}$. The guide dissipates at $t = t_{simple}$ when the core density equals the density at one of the density holes, $\Delta N_{core}(t_{simple}) = \Delta N_h(0, t_{simple})$. Solving this equation:

$$t_{simple} = \frac{1}{4\alpha}\left(\frac{a^2}{\ln(n_{fil})} - R_0^2\right) \tag{5.1}$$

For the parameters for the 50 m waveguide in Chapter 4 [55], $a = 2.8$mm and $n_{fil} = 18$, $t_{simple} = 31$ ms. This is a slight underestimate of the waveguide lifetime estimate from Fig. 4.10, but the waveguide strength is extremely low by that time. For the parameters in this chapter, $a = 0.5$ mm at the entrance of the guide and $n_{fil} = 4$, $t_{simple} = 2$ ms. This also seems to be an underestimate of the estimated lifetime of 4 ms based on the pulse repetition rates necessary for quasi-steady-state guiding seen in Fig. 5.2. At the focus of the waveguide, $a = 0.25$ mm and $t_{simple} = 0.5$ ms, much less than the waveguide lifetime. This indicates that the waveguide lifetime corresponds to the lifetime of the air density structure at the entrance of strongly-focused waveguides, not at the focus.

To demonstrate the merging of density holes and the applicability of Eq. (5.1), interferometric measurements of density holes from a tightly-focused TEM_{11} mode (f/75) were performed, similar to experiments in [47,54], with results shown in Fig. 5.4(a). By tightly focusing the TEM_{11} structure, we avoid probe refractive distortion

and can extract phase interferometrically from an optical probe ($\lambda = 532$ nm, $\tau \sim 7$ ns) [28]. In this geometry, $a = 37.5$ μm and $R_0 \approx 17$ μm, with which Eq. (5.1) predicts a guiding structure lifetime $t_{guide} = 8$ μs. In the top row of Fig. 5.4(a), we see a guiding structure out to 9 μs which becomes one large density depression by 10 μs, close to the value calculated with Eq. (5.1). The first panel shows a high on-axis density from the four filament-induced acoustic waves colliding on-axis, which is consistent with acoustic waveguides demonstrated in past work [54]. The bottom row of Fig. 5.4(a) shows results from a thermal diffusion simulation which solved the 2D+1 diffusion equation $\alpha \nabla^2 T = \partial T / \partial t$ for temperature $T(x, y, t)$, with $\alpha = 0.217$ cm^2/s being the thermal diffusivity of air at 20ºC. The simulation initialized each density hole as a gaussian centered at (x_n, y_n), $T(x, y, 0) = T_0 \sum_{i=1}^{n_{fil}} e^{-((x-x_n)^2+(y-y_n)^2)/R_0^2}$ with parameters $T_0 = 15$ K and $R_0 = 17$ μm in agreement with experiment, and with $a = \sqrt{x_n^2 + y_n^2}$ for all n. The density holes are evenly spaced around a ring of radius a, seen best in the leftmost panel of the bottom row in Fig. 5.4(a). These simulations closely track with the experimental results in the top row of Fig. 5.4(a) and show guiding structure dissipation at 10 μs without the effect of the acoustic wave shown at $t = 0.1$ μs. Running equivalent simulations with the parameters in the quasi-steady-state guiding experiment in Sec. 5.3.1 and the 50m guiding experiment in Chapter 4 show guiding structure dissipation at 2.3 ms and 67 ms, respectively.

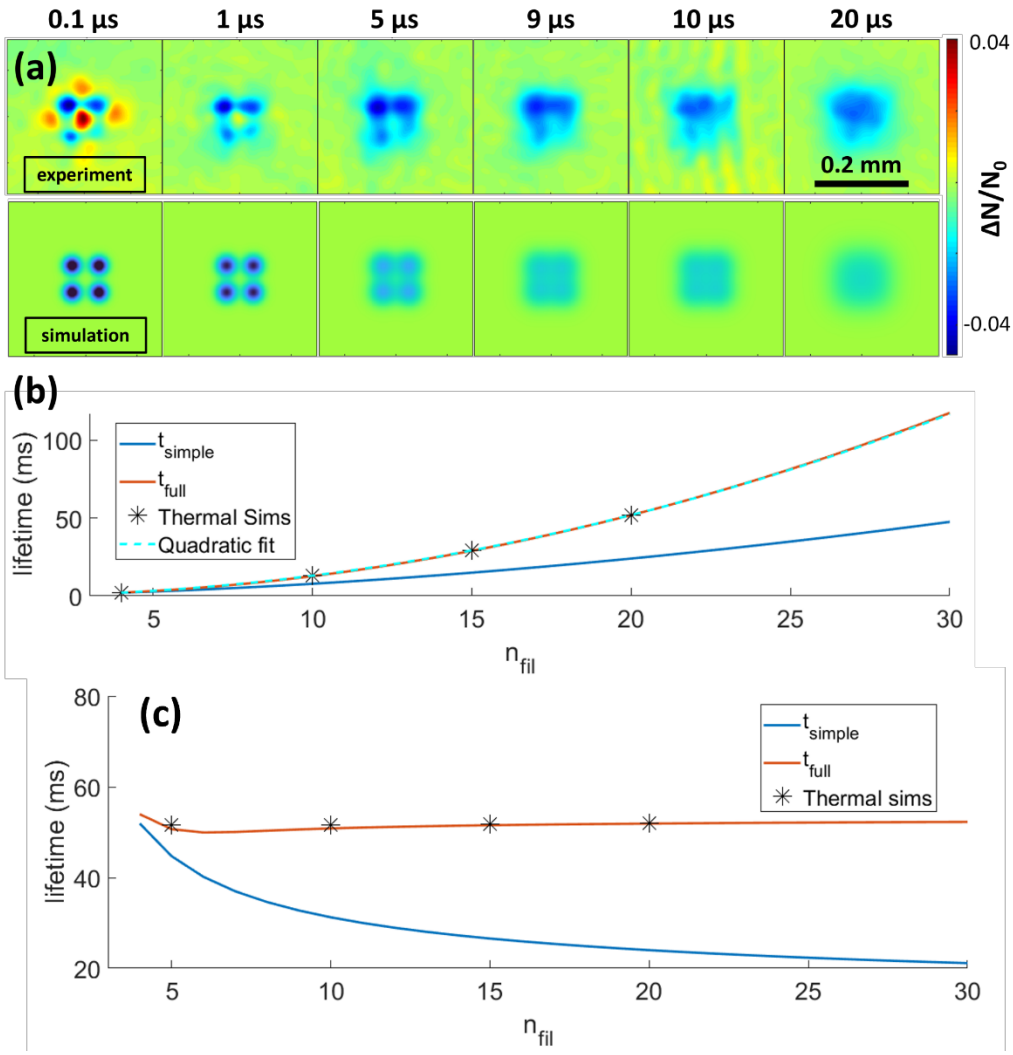

Figure 5.4 (a) *Top row:* Experimental density hole evolution from interferometric measurements. *Bottom row:* Simulated evolution of four density holes using a thermal diffusion model. **(b)** Comparison of thermal simulation results, t_{simple} (Eq. 5.1), t_{full} (Eq. 5.2), and a quadratic fit to t_{full}. **(c)** Plot of t_{simple} and t_{full} with fixed $a = 0.25$ cm and variable n_{fil}, with overlaid thermal simulation results. Plots (b) and (c) each assume the guide is supporting a $\lambda = 532$ nm beam.

In all cases, the experimental and simulated guide lifetimes are larger than those calculated with Eq. (5.1). This is due to Eq. (5.1) neglecting the contribution of neighboring density holes to the local density depression, which increases with time as each hole diffuses. Additionally, the waveguide must have a V-parameter $V = 2\pi a/\lambda\sqrt{n_{co}^2 - n_{cl}^2} > 2.405$ to support the fundamental mode, which requires that

the core-cladding index contrast be above a minimum value $\approx 0.073\lambda^2/a^2$. Including these effects gives Eq. (5.2) for waveguide lifetime (and assuming $n_{co} - 1 \ll 1$ and $n_{cl} - 1 \ll 1$):

$$n_{fil} e^{-\left(R_0^2+4\alpha t\right)^{-1} a^2} = \sum_{j=0}^{n_{fil}-1} e^{-\left(R_0^2+4\alpha t\right)^{-1} d_{j0}^2} - \frac{N_{atm}\left(1+\frac{4\alpha t}{R_0^2}\right)}{2\Delta N_0 \delta n_0}\left(\frac{2.405\lambda}{2\pi a}\right)^2 \quad (5.2)$$

Where $d_{j0} = 2a\left|\sin\left(j\pi/n_{fil}\right)\right|$ is the distance between a reference density hole and the jth density hole, ΔN_0 is the initial number density change at the center of each density hole, $N_{atm} \approx 2.5 \times 10^{19}$ cm^{-3} is the ambient atmospheric density, λ is the wavelength of the guided beam, and δn_0 is the increase in refractive index of air at ambient density ($\delta n_0 = 2.77 \times 10^{-4}$ at $\lambda = 532$ nm). Eq. (5.2) differs from (5.1) through the summation in the first term on the right-hand side, to include the impact of all density holes, and the wave effects in the second term on the right-hand side. Eq. (5.2) has no general closed-form solution (which we will call t_{full}), but it can be easily solved numerically.

For the parameters in Sec. 5.3.1, Eq. (5.2) is satisfied when $t_{full} = 2.3$ ms, larger than the value calculated with Eq. (5.1) by 15% and identical to the thermal simulation value. It still underestimates the estimate based on the quasi-steady-state transition, which implies that the entrance of the guide is earlier when the guide is larger, increasing the waveguide lifetime. For the tightly focused parameters in Fig. 5.4(a), this gives $t_{full} = 10$ µs, matching the measured guide lifetime. When used to calculate the lifetime for the 50 m waveguide in Chapter 4, $t_{full} \approx 67$ ms, which is much closer to the simulated value due to the neighboring density holes

contributing more to local density over time. However, it appears to be an overestimate of the experimental value in Sec. 4.4.3.

The values of t_{simple} and t_{full} for variable n_{fil} with filaments at a fixed spacing in Eq. (5.2) are plotted in Fig. 5.4(b). To keep filaments at a fixed spacing, the waveguide radius a increases proportionally with n_{fil} from $a = 0.5$ mm for $n_{fil} = 4$ to $a = 3.75$ mm for $n_{fil} = 30$, which is consistent with how waveguides are engineered to maintain high efficiency in Chapter 4. For large values of n_{fil}, t_{simple} vastly underestimates t_{full}, but it is close for smaller values n_{fil} where neighboring density holes cannot contribute as strongly to local density before filling in the core. While $t_{simple} \sim n_{fil}^2 / \ln(n_{fil})$, $t_{full} \sim n_{fil}^2$ due to the contribution from nearby density holes with waveguide size. This is demonstrated by including a quadratic best-fit over the plot for t_{full}, which matches exceptionally well (~0.01 ms root mean squared error).

Additionally, we compute waveguide lifetime with a fixed waveguide size ($a = 0.25$ cm) and variable n_{fil} in Fig. 5.4(c). This shows that, past low values of n_{fil} where there are essentially no nearby density holes, filament number does not impact waveguide lifetime. Physically, this occurs due to the additional filaments filling in the waveguide core more substantially, even as they contribute to deepening the guide cladding.

In each of the plots in Fig. 5.4, the guided beam has wavelength $\lambda = 532$ nm, which is easily supported by even weak core-cladding index contrasts down to $\sim 10^{-9}$. However, Eq. (5.2) implies that waveguide lifetime is a function of the guided beam wavelength in addition to the physical characteristics of the air

waveguide. If the term proportional to λ in Eq. (5.2) becomes substantial, then the core-cladding index must be large to guide the beam. This effectively decreases the waveguide lifetime for MIR and LWIR beams. In Fig. 5.5(a), t_{full} is again calculated, replicating Fig. 5.4(b), but with several wavelengths chosen to demonstrate this effect, including a "geometric" trace which considers the limit of $\lambda \to 0$. The 532 nm beam that was guided in Chapters 4 and 5 is close to the geometric case, but MIR (3900 nm) and LWIR (10000 nm) beams have a much shorter lifetime, down to ~2 ms for $n_{fil} = 20$ at $\lambda = 10000$ nm. This indicates that quasi-steady-state guiding is still possible in these regimes, but much faster repetition rates are necessary than when guiding visible and NIR beams.

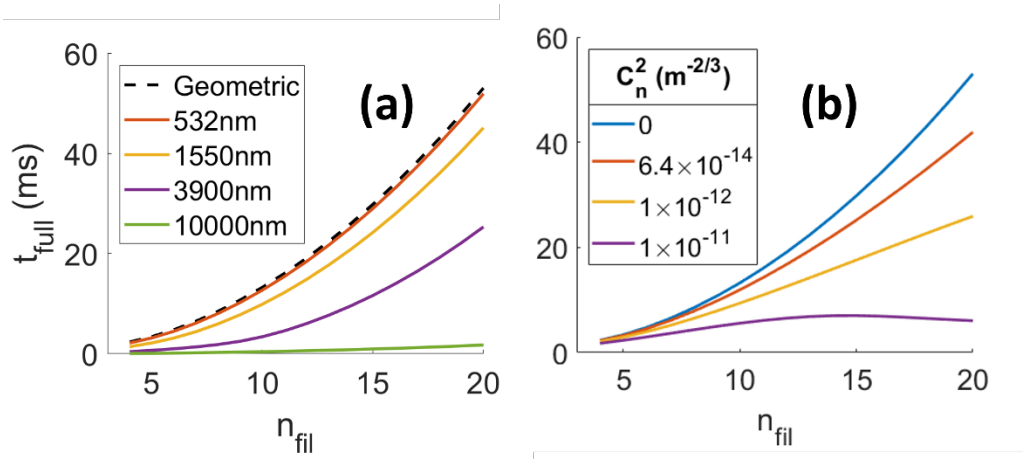

Figure 5.5 (a) Plot of waveguide lifetime (t_{full}) when guiding different wavelengths. "Geometric" refers to the guide lifetime in the limit of $\lambda \to 0$. **(b)** Guide lifetime (t_{full}) for a $\lambda =$ 532 nm beam in different turbulent environments, characterized by C_n^2.

One atmospheric effect that must be accounted for is turbulence, which requires a minimum index contrast to maintain a guiding structure, as described in Sec. 4.2. This will primarily impact larger guides that persist long enough for the core-cladding index contrast to drop below turbulent index variations. For instance, the

simulated index contrast just before the guide breaks down for $n_{fil} = 20$ and $a = 2.5$ cm is $n_{core} - n_{clad} = 4 \times 10^{-9}$. The average turbulence-induced index variation given $C_n^2 = 6.4 \times 10^{-14}$ m$^{-2/3}$ [53] is $\sim 4 \times 10^{-8}$, larger than the simulated index contrast and therefore destroying the guiding structure. In Fig. 5.5(b), t_{turb} is plotted, which is the time for the index contrast to be equal to or less than the average index variation over the guide size due to turbulence, $\delta n_{turb} = \sqrt{C_n^2 (2a)^{2/3}}$. For weak to medium strength turbulence ($C_n^2 = 6.4 \times 10^{-14}$ m$^{-2/3}$), waveguide lifetime only slightly decreases to ~40 ms for $n_{fil} = 20$. For strong turbulence ($C_n^2 = 10^{-12} - 10^{-11}$ m$^{-2/3}$) the lifetime decreases more drastically, with a maximum lifetime for $C_n^2 = 10^{-11}$ m$^{-2/3}$ around $n_{fil} = 15$ appearing due to the increase in δn_{turb} with waveguide size. The $n_{fil} = 20$ lifetime decreases from 53 ms with no turbulence to 6 ms with $C_n^2 = 10^{-11}$ m$^{-2/3}$. Turbulence can explain the overestimate of guide lifetime for the 50m waveguide, as for $C_n^2 = 2 \times 10^{-13}$ m$^{-2/3}$, a reasonable value outside of the lab, the guide lifetime decreases to roughly 42 ms. This is very close to the experimental lifetime. Therefore, the turbulent operating conditions of the waveguide must be considered when choosing repetition rate for a quasi-steady-state waveguide.

5.4 Conclusions

Based on these results, we expect to extend quasi-steady-state air waveguiding to much longer air waveguides driven by wider and higher energy filamenting beams. For such guides, thermal diffusion timescales can be tens of milliseconds [55], and the calculated waveguide lifetimes based on Eq. (5.1) and

Eq. (5.2) are also tens of milliseconds. Since the transition to quasi-steady-state guiding occurs when a new guide is generated before the prior one dissipates, this will reduce the required repetition rate well below 1 kHz for quasi-steady-state operation and will be around 20-50 Hz. This also means that a 1 kHz repetition rate in this regime will more closely approximate a true steady-state guide, like how the 1 kHz trace in Fig. 5.2 is closer to true steady-state than quasi-steady-state waveguides at lower repetition rates. Such a steady-state guide would be optimal for guiding continuous-wave beams, particularly at high powers. Additionally, if guiding is needed in a highly turbulent environment or for long wavelength beams, higher repetition rates are necessary to achieve quasi-steady-state guiding even with a large waveguide.

Chapter 6 Future Work

6.1 Long-distance Quasi-steady-state Air Waveguiding

Given the studies in Chapters 2, 4, and 5, one can reasonably plan an experiment for a long-distance quasi-steady-state air waveguide. Commercial Yb:YAG 1 kHz lasers can produce 600 ps FWHM pulses, which from Chapter 2 will produce 1.4 × longer filaments than the 300 fs pulses used in Chapter 4. However, the longer 1030 nm wavelength has a shorter Rayleigh length, which will also lead to ~0.6× shorter filaments. Scaling based on the 50 m guide in Sec. 4.4.3, a ~7 mm diameter ring is needed to produce a 50 m guide which only requires ~30 Hz for quasi-steady-state guiding ignoring wavelength and turbulence effects. For the same number of filaments in the ring, a 600 fs Yb:YAG pulse will require ~480 mJ due to the longer pulse duration decreasing peak power and longer wavelength increasing P_{crit}. There are commercial kHz Yb:YAG lasers that meet this criteria (see the TRUMPF Dira 1000-1), as do proven high-energy 1 kHz Yb:YAG systems elsewhere [109,110] and 100 Hz >1 J systems, which would still generate quasi-steady-state guides [111].

One way to relax this high energy requirement is to frequency double the 1030 nm Yb:YAG pulse. The shorter wavelength means a 2 × smaller ring will provide the same filament length. Because the lower wavelength also decreases P_{crit} by 4 ×, the necessary power to maintain the same filament density on the ring decreases by 8 ×. This reduces the energy limit from ~480 mJ to ~60 mJ. If the second harmonic generation scheme is more than 12.5% efficient, larger

waveguides are possible and the waveguide length will increase, and SHG schemes for 1030 nm pulses have been as high as ~80% efficient in other work [112]. For standard commercial thin disk YAG lasers, 80% SHG efficiency would generate up to >160 mJ of energy at 515 nm, making this a plausible way to get around stiff energy requirements for long-distance quasi-steady-state guiding.

6.2 High-average-power Waveguiding

Back-of-the-envelope calculations from Chapter 4 suggest that air waveguides can support extremely high powers, up to several megawatts. However, these calculations were not performed with quasi-steady-state air waveguides in mind and assumed a 5 ms high-power pulse duration. For CW guiding, the heating in the core will approach a steady-state core density related to the beam power, guide size, and the thermal diffusion rate of air. For these scientific reasons, in addition to the need to demonstrate the ability of air waveguides to guide high powers, a further experiment is necessary to study the impact of guiding high-power beams on waveguide performance.

MW-class lasers are not commercially available; however, one can use a lower power laser in a smaller waveguide to achieve the same effect. The short-distance waveguide in Chapter 5 has a minimum size of ~0.5 mm diameter, ~11 × smaller than the size used in the original calculation in Chapter 4. Since the necessary power to dissipate the waveguide, as calculated in Sec. 5.5, scales with guide diameter, only 50 kW would be required.

To test this, a 2 kW CW Yb:YAG single-mode fiber laser will be guided with a small, short-distance waveguide to test the guide efficiency and how it varies with

guided beam power. Although the beam power is less than 50 kW, this can test the role of laser duty cycle, and how much removing the assumption of 5 ms guiding time reduces the power limit. Additionally, by seeding the air with aerosols, it is possible to increase the linear absorption of the region and, therefore, increase the CW heating rate and similarly decrease the power limit. This experiment will be used to find the real power limit of air waveguides.

6.3 Guiding Through Turbulent and Foggy Atmosphere

Most guiding experiments thus far have occurred in laboratory environments. However, air waveguides would be useful in unfavorable environments, such as fog-laden or highly turbulent air. Fog clearing from filamentation was demonstrated in Chapter 3 to be due to optical shattering in the filament core and reservoir. Patterned filamentation used for air waveguides can therefore be used to clear a ring of fog in a similar manner, while not clearing the core of the guide. However, it is possible that the buoyancy associated with high-repetition-rate filamentation [57] can be used to lift fog droplets out of the waveguide core, increasing guide efficiency even further. This would need to be studied both by demonstrating guiding through a fog chamber and measuring droplet movement with different repetition rates, the latter similar to the experiment carried out in Chapter 3 to measure droplet displacement.

The impact of turbulence on air waveguides was partially analyzed in Section 3.2 by comparing the average variation of index with a given turbulence strength (C_n^2) to the core-cladding index contrast in the guide. The calculation in Section 4.2 concludes that standard air waveguides ($\Delta N/N_0 \approx 0.04$) will continue to guide in

strong turbulence up to $C_n^2 \approx 4 \times 10^{-11}$ m$^{-2/3}$. It is also expected that turbulence will impact waveguide lifetime, since the core-cladding index contrast will approach the turbulence index variance with time as discussed in Sec. 5.3.2. Additionally, turbulence will impact filament propagation itself, although since filaments are smaller than the inner scale of turbulence $l_0 \sim 1$ mm [113], it is expected to cause shot-to-shot deflection of filaments rather than filament break-up [114]. Turbulence can, however, induce strong multifilamentation due to phase perturbations localizing energy [115] and impact filament collapse location [53]. The heater tape in [53] was used to generate turbulence strength up to $C_n^2 \approx 10^{-11}$ m$^{-2/3}$, close to the turbulence limit $C_n^2 \approx 4 \times 10^{-11}$ m$^{-2/3}$ and therefore making it an effective tool to waveguide strength in turbulence.

Appendices

A.1 Microphone Calibration with Helium Cell Measurements

To calibrate the microphone array, we directly measured the total energy deposition from a filament by measuring the phase delay of a probe pulse from the filament-induced density depression interferometrically, a technique utilized before in [28]. By using a Helium cell [26,79], it is possible to measure the phase of the probe throughout the filament, since we can use the Helium cell to capture the filament mid-flight without damaging any optics. Additionally, the Helium cell was placed on a rail to allow measurement at several axial locations along the filament to ensure calibration accuracy. Fig. A1(a) shows the calibration setup, where a Nd:YAG ($\lambda_0 = 532$ nm, $\tau \sim 7$ ns) probe co-propagated with the filament and was imaged through a folding wavefront interferometer after exiting the Helium cell.

In Fig. A1(b), we show the measured density hole from a filament and in Fig. A1(c) the calculated total energy deposition from that density hole as a function of propagation distance z. The total energy deposition is also the integral of the longitudinally-resolved microphone trace, where each measured microphone voltage corresponds to a value for energy deposition per unit length. By fitting the integrated microphone signal to the measured deposition, we calculated the conversion between the microphone voltage signal and $\partial_z \varepsilon_{dep}$ in units of J/cm.

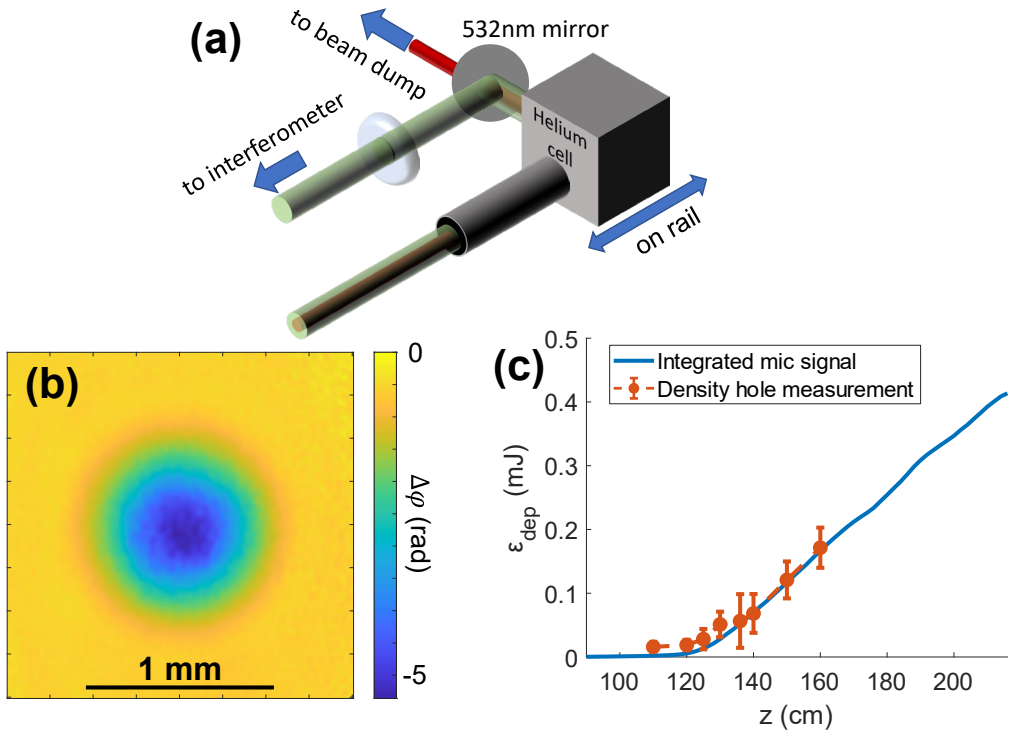

Figure A1 (a) Diagram showing probe co-propagation with filament into the Helium cell for interferometric deposition measurement. **(b)** Total accumulated phase from a density hole generated by a $\tau = 500$ fs filament at $z = 160$ cm, with a 1 ms delay. **(c)** Integrated microphone signal after calibration plotted over measured total energy deposition with distance for $\tau = 500$ fs, $\varepsilon_{pulse} = 7.1 - 7.2$ mJ ($P = 5.46P_{crit} - 5.53P_{crit}$), with a best-fit calibration of 1V = 14.3 μJ/cm.

A.2 UPPE Simulations and Energy Deposition

UPPE simulations were performed throughout this thesis using an in-house MATLAB implementation of Eqs. 1.29 and 1.30 called 'YAPPE' (Yet Another Pulse Propagation Effort). The ionization rate used to calculate N_e is the "strong field" rate best suited for our Keldysh parameter $\gamma = \omega(2m_e U_I)^{\frac{1}{2}}/(eE) \sim 1$ [14] including a Drude avalanche ionization model for > 1 ps FWHM pulses [23]. The electron density therefore evolves as follows:

$$\frac{dN_e}{d\xi} = \frac{\sigma}{U_I} N_e I(\xi) + N_g \Gamma_{PI}\{I(\xi)\} \qquad (A2.1)$$

Where σ is the Drude collision cross-section, U_I is the effective ionization energy of air, $N_g = 2.5 \times 10^{19}$ cm^{-3} is the number density of air, $\xi = t - z/v_g$ is time in the local frame of the pulse, and $\Gamma_{PI}\{I(\xi)\}$ is the photoionization rate as a function of pulse intensity.

Energy deposition is computed from the calculated fields by three mechanisms: photoionization losses, molecular rotational losses, and electron-neutral collisional losses (or inverse Bremsstrahlung). We calculate it with the following equation:

$$\partial_z \varepsilon_{dep} = 2\pi \iint \left(\left[\frac{\partial N_e^{N_2}}{\partial \xi} U_I^{N_2} + \frac{\partial N_e^{O_2}}{\partial \xi} U_I^{O_2} \right] + \frac{2\pi}{c} \frac{\partial \chi_{rot}}{\partial \xi} I + \frac{\partial N_e}{\partial \xi} U_p + \nu_{en} N_e U_p \right) r dr d\xi \quad (A2.2)$$

Where N_e^X is the electron density in the filament from air species X, U_I^X is the ionization energy of air species X, χ_{rot} is the time-dependent susceptibility from molecular rotations, $I = \frac{c}{8\pi} E^2$ is the laser field intensity, $\nu_{en} = 2.86$ ps^{-1} is the electron-neutral collision rate [23], and $U_p = (2\pi e^2 / c m_e \omega_0^2) I$ is the ponderomotive energy of a free electron in the plasma. In Eq. (A2.2), the first term in the integrand corresponds to deposition into photoionization, the second term deposition into molecular rotations, the third term is deposition through the ponderomotive energy imparted on newly freed electrons, and the fourth term is deposition through electron-neutral collisions in the filament plasma.

A.3 Ionization and Periodic Refocusing

In our simulations, there exists a discrepancy in oscillation period where the simulations demonstrate a period of around 27 cm, whereas experimentally we see a period of around 22 cm (best seen in Fig. 5.2(a)). Uncertainty in our modelling can potentially explain this discrepancy. To demonstrate this, we have run a simulation using an ADK ionization model [15] to compare it with the standard strong field ionization model used throughout our UPPE simulations [14]. In Fig. A2(a) we plot the simulated energy deposition at $\tau = 400$ fs with strong field ionization against one stitched microphone trace. In this case, the peak energy deposition is marginally higher (~14%) and the oscillation period is noticeably slower. Fig. A2(b) plots the same experimental trace against a simulated trace using ADK to model ionization instead of strong field. In this case, the oscillation period is closer to experimental, around 21 cm, but the simulated peak deposition is nearly 50% lower than the experimental. This shows a strong dependence on ionization modelling even with the same physical parameters for both peak energy deposition and longitudinal oscillation period. Given that ADK loses accuracy for Keldysh parameters above 0.5 and our simulated Keldysh parameter is around unity, strong field ionization is still considered more appropriate for our modelling, although this result highlights the ionization model sensitivity.

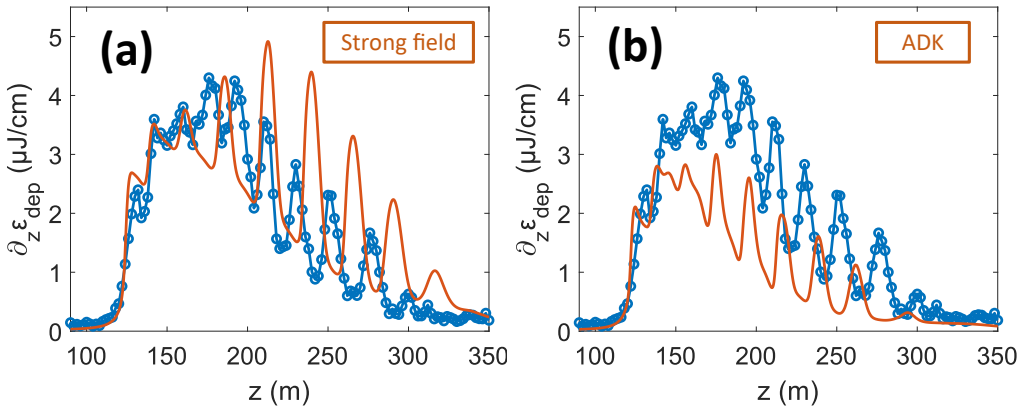

Figure A2 (a) Plot of simulated deposition with "strong field" ionization [14] against experiment, $\tau = 400$ fs. **(b)** Plot of simulated deposition with ADK ionization [15] against experiment, $\tau = 400$ fs.

Publications by the candidate

1. S.W. Hancock, S. Zahedpour, **A.Goffin**, and H.M. Milchberg, "Free-space propagation of spatiotemporal optical vortices", Optica **6**, 1547 (2019).
2. I. Larkin, J. Griff-McMahon, A. Schweinsberg, **A. Goffin**, A. Valenzuela, and H.M. Milchberg, "Full path single-shot imaging of femtosecond pulse collapse in air turbulence", Optics Letters **45**, 2518 (2020).
3. B. Miao, L. Feder, J.E. Schrock, **A. Goffin**, and H.M. Milchberg, "Optical guiding in meter-scale plasma waveguides", Phys. Rev. Lett. **125**, 074801 (2020).
4. E.W. Rosenthal, I. Larkin, **A. Goffin**, T. Produit, M.C. Schroeder, J.-P. Wolf, and H.M. Milchberg, "Dynamics of the femtosecond laser-triggered spark gap", Optics Express **28**, 24599 (2020).
5. D. Woodbury, **A. Goffin**, R.M. Schwartz, J. Isaacs, and H.M. Milchberg, "Self-guiding of long-wave infrared laser pulses mediated by avalanche ionization", Phys. Rev. Lett. **125**, 133201 (2020).
6. L. Feder, B. Miao, J.E. Schrock, **A. Goffin**, and H.M. Milchberg, "Self-waveguiding of relativistic laser pulses in neutral gas channel", Phys. Rev. Research **2**, 043173 (2020).
7. A. Higginson, Y. Wang, H. Chi, **A. Goffin**, I. Larkin, H.M. Milchberg, and J.J. Rocca, "Wake Dynamics of air filaments generated by high-energy picosecond laser pulses at 1 kHz repetition rate", Optics Letters **46**, 5449 (2021).
8. **A. Goffin**, J. Griff-McMahon, I. Larkin, and H.M. Milchberg, "Atmospheric aerosol clearing by femtosecond filaments", Phys. Rev. Applied **18**, 014017 (2022).

9. **A. Goffin**, I. Larkin, A. Tartaro, A. Schweinsberg, A. Valenzuela, E.W. Rosenthal, and H.M. Milchberg, "Optical guiding in 50-meter-scale air waveguides", Phys. Rev. X **13**(1), 011006 (2023).
10. **A. Goffin**, A. Tartaro, and H.M. Milchberg, "Quasi-steady-state air waveguide", Optica **10**, 505-506 (2023).
11. **S**.W. Hancock, S. Zahedpour, **A. Goffin**, and H.M. Milchberg, "Spatiotemporal torquing of light", Phys. Rev. X **14**(1), 011031 (2024).

Bibliography

1. J. D. Jackson, *Classical Electrodynamics* (Wiley, 1999).
2. D. Casasent, "Spatial light modulators," Proc. IEEE **65**, 143–157 (1977).
3. J. A. Armstrong, N. Bloembergen, J. Ducuing, and P. S. Pershan, "Interactions between Light Waves in a Nonlinear Dielectric," Phys. Rev. **127**, 1918–1939 (1962).
4. A. E. Siegman, *Lasers* (University Science Books, 1986).
5. L. Allen, M. W. Beijersbergen, R. J. C. Spreeuw, and J. P. Woerdman, "Orbital angular momentum of light and the transformation of Laguerre-Gaussian laser modes," (1992).
6. R. W. Boyd, *Nonlinear Optics* (Academic Press, 2008).
7. P. B. Corkum, C. Rolland, and T. Srinivasan-Rao, "Supercontinuum Generation in Gases," Phys. Rev. Lett. **57**, 2268–2271 (1986).
8. G. Stibenz, N. Zhavoronkov, and G. Steinmeyer, "Self-compression of millijoule pulses to 7.8 fs duration in a white-light filament," (2006).
9. J. P. Palastro, T. M. Antonsen, and H. M. Milchberg, "Compression, spectral broadening, and collimation in multiple, femtosecond pulse filamentation in atmosphere," Physical Review A **86**, (2012).
10. S. Zahedpour, J. K. Wahlstrand, and H. M. Milchberg, "Quantum Control of Molecular Gas Hydrodynamics," Physical Review Letters **112**, (2014).
11. S. Varma, Y.-H. Chen, and H. M. Milchberg, "Quantum molecular lensing of femtosecond laser optical/plasma filamentsa…," Phys. Plasmas **16**, 056702 (2009).
12. S. Varma, Y.-H. Chen, and H. M. Milchberg, "Trapping and Destruction of Long-Range High-Intensity Optical Filaments by Molecular Quantum Wakes in Air," Physical Review Letters **101**, (2008).
13. L. V. Keldysh, "Ionization in the field of a strong electromagnetic wave," (1965).
14. S. V. Popruzhenko, V. D. Mur, V. S. Popov, and D. Bauer, "Strong Field Ionization Rate for Arbitrary Laser Frequencies," Physical Review Letters **101**, (2008).
15. V. S. Popov, "Tunnel and multiphoton ionization of atoms and ions in a strong laser field (Keldysh theory)," Phys.-Usp. **47**, 855–885 (2004).
16. D. Woodbury, R. M. Schwartz, E. Rockafellow, J. K. Wahlstrand, and H. M. Milchberg, "Absolute Measurement of Laser Ionization Yield in Atmospheric Pressure Range Gases over 14 Decades," Physical Review Letters **124**, (2020).
17. A. Schmitt-Sody, H. G. Kurz, L. Bergé, S. Skupin, and P. Polynkin, "Picosecond laser filamentation in air," New J. Phys. **18**, 093005 (2016).
18. Y. Itikawa, "Cross Sections for Electron Collisions with Oxygen Molecules," Journal of Physical and Chemical Reference Data **38**, 1–20 (2009).
19. Y. Itikawa, "Cross Sections for Electron Collisions with Nitrogen Molecules," Journal of Physical and Chemical Reference Data **35**, 31–53 (2006).
20. P. Panagiotopoulos, P. Whalen, M. Kolesik, and J. V. Moloney, "Carrier field shock formation of long-wavelength femtosecond pulses in single-crystal

diamond and air," Journal of the Optical Society of America B **32**, 1718 (2015).
21. P. Panagiotopoulos, K. Schuh, M. Kolesik, and J. V. Moloney, "Simulations of 10 μm filaments in a realistically modeled atmosphere," Journal of the Optical Society of America B **33**, 2154 (2016).
22. J. K. Ranka, R. W. Schirmer, and A. L. Gaeta, "Observation of Pulse Splitting in Nonlinear Dispersive Media," Phys. Rev. Lett. **77**, 3783–3786 (1996).
23. A. Couairon and A. Mysyrowicz, "Femtosecond filamentation in transparent media," Physics Reports **441**, 47–189 (2007).
24. S. Zahedpour, J. K. Wahlstrand, and H. M. Milchberg, "Measurement of the nonlinear refractive index of air constituents at mid-infrared wavelengths," Opt. Lett. **40**, 5794 (2015).
25. S. Zahedpour, S. W. Hancock, and H. M. Milchberg, "Ultrashort infrared 25–11 μm pulses: spatiotemporal profiles and absolute nonlinear response of air constituents," Opt. Lett. **44**, 843 (2019).
26. N. Jhajj, I. Larkin, E. W. Rosenthal, S. Zahedpour, J. K. Wahlstrand, and H. M. Milchberg, "Spatiotemporal Optical Vortices," Physical Review X **6**, (2016).
27. W. Liu, J.-F. Gravel, F. Théberge, A. Becker, and S. L. Chin, "Background reservoir: its crucial role for long-distance propagation of femtosecond laser pulses in air," Applied Physics B **80**, 857–860 (2005).
28. E. W. Rosenthal, N. Jhajj, I. Larkin, S. Zahedpour, J. K. Wahlstrand, and H. M. Milchberg, "Energy deposition of single femtosecond filaments in the atmosphere," Optics Letters **41**, 3908 (2016).
29. M. Rodriguez, R. Bourayou, G. Méjean, J. Kasparian, J. Yu, E. Salmon, A. Scholz, B. Stecklum, J. Eislöffel, U. Laux, A. P. Hatzes, R. Sauerbrey, L. Wöste, and J.-P. Wolf, "Kilometer-range nonlinear propagation of femtosecond laser pulses," Physical Review E **69**, (2004).
30. M. Durand, A. Houard, B. Prade, A. Mysyrowicz, A. Durécu, B. Moreau, D. Fleury, O. Vasseur, H. Borchert, K. Diener, R. Schmitt, F. Théberge, M. Chateauneuf, J.-F. Daigle, and J. Dubois, "Kilometer range filamentation," Optics Express **21**, 26836 (2013).
31. M. Kolesik and J. V. Moloney, "Self-healing femtosecond light filaments," Optics Letters **29**, 590 (2004).
32. S. Skupin, L. Bergé, U. Peschel, and F. Lederer, "Interaction of Femtosecond Light Filaments with Obscurants in Aerosols," Physical Review Letters **93**, (2004).
33. M. Mlejnek, E. M. Wright, and J. V. Moloney, "Dynamic spatial replenishment of femtosecond pulses propagating in air," Optics Letters **23**, 382–384 (1997).
34. M. S. Le, G. A. Hine, A. Goffin, J. P. Palastro, and H. M. Milchberg, "Self-focused pulse propagation is mediated by spatiotemporal optical vortices," arXiv:2403.04669 (2024).
35. J. Kasparian, M. Rodriguez, G. Méjean, J. Yu, H. Wille, R. Bourayou, S. Frey, Y.-B. André, A. Mysyrowicz, R. Sauerbrey, J.-P. Wolf, and L. Wöste, "White-Light Filaments for Atmospheric Analysis," Science **301**, 61–64 (2003).

36. A. Englesbe, J. Elle, R. Schwartz, T. Garrett, D. Woodbury, D. Jang, K.-Y. Kim, H. Milchberg, R. Reid, A. Lucero, D. Gordon, R. Phillips, S. Kalmykov, and A. Schmitt-Sody, "Ultrabroadband microwave radiation from near- and mid-infrared laser-produced plasmas in air," Phys. Rev. A **104**, 013107 (2021).
37. K. Y. Kim, A. J. Taylor, J. H. Glownia, and G. Rodriguez, "Coherent control of terahertz supercontinuum generation in ultrafast laser–gas interactions," Nature Photonics **2**, 605–609 (2008).
38. A. Mysyrowicz, R. Danylo, A. Houard, V. Tikhonchuk, X. Zhang, Z. Fan, Q. Liang, S. Zhuang, L. Yuan, and Y. Liu, "Lasing without population inversion in N2+," APL Photonics **4**, 110807 (2019).
39. R. Danylo, G. Lambert, Y. Liu, V. Tikhonchuk, A. Houard, and A. Mysyrowicz, "Quantum erasing of laser emission in N2+," Opt. Lett. **45**, 4670 (2020).
40. J. Yao, B. Zeng, H. Xu, G. Li, W. Chu, J. Ni, H. Zhang, S. L. Chin, Y. Cheng, and Z. Xu, "High-brightness switchable multiwavelength remote laser in air," Phys. Rev. A **84**, 051802 (2011).
41. P. Rohwetter, J. Kasparian, K. Stelmaszczyk, Z. Hao, S. Henin, N. Lascoux, W. M. Nakaema, Y. Petit, M. Queißer, R. Salamé, E. Salmon, L. Wöste, and J.-P. Wolf, "Laser-induced water condensation in air," Nature Photon **4**, 451–456 (2010).
42. K. Stelmaszczyk, P. Rohwetter, G. Méjean, J. Yu, E. Salmon, J. Kasparian, R. Ackermann, J.-P. Wolf, and L. Wöste, "Long-distance remote laser-induced breakdown spectroscopy using filamentation in air," Applied Physics Letters **85**, 3977–3979 (2004).
43. T. A. Labutin, V. N. Lednev, A. A. Ilyin, and A. M. Popov, "Femtosecond laser-induced breakdown spectroscopy," J. Anal. At. Spectrom. **31**, 90–118 (2016).
44. Y. Shima and H. Yatom, "Inverse bremsstrahlung energy absorption rate," Phys. Rev. A **12**, 2106–2117 (1975).
45. E. W. Rosenthal, J. P. Palastro, N. Jhajj, S. Zahedpour, J. K. Wahlstrand, and H. M. Milchberg, "Sensitivity of propagation and energy deposition in femtosecond filamentation to the nonlinear refractive index," Journal of Physics B: Atomic, Molecular and Optical Physics (2015).
46. Y.-H. Chen, S. Varma, A. York, and H. M. Milchberg, "Single-shot, space- and time-resolved measurement of rotational wavepacket revivals in H2, D2, N2, O2, and N2O," Opt. Express **15**, 11341 (2007).
47. J. K. Wahlstrand, N. Jhajj, E. W. Rosenthal, S. Zahedpour, and H. M. Milchberg, "Direct imaging of the acoustic waves generated by femtosecond filaments in air," Optics Letters **39**, 1290 (2014).
48. E. W. Rosenthal, I. Larkin, A. Goffin, T. Produit, M. C. Schroeder, J.-P. Wolf, and H. M. Milchberg, "Dynamics of the femtosecond laser-triggered spark gap," Optics Express **28**, 24599 (2020).
49. A. Houard, P. Walch, T. Produit, V. Moreno, B. Mahieu, A. Sunjerga, C. Herkommer, A. Mostajabi, U. Andral, Y.-B. André, M. Lozano, L. Bizet, M. C. Schroeder, G. Schimmel, M. Moret, M. Stanley, W. A. Rison, O. Maurice, B. Esmiller, K. Michel, W. Haas, T. Metzger, M. Rubinstein, F. Rachidi, V.

Cooray, A. Mysyrowicz, J. Kasparian, and J.-P. Wolf, "Laser-guided lightning," Nat. Photon. **17**, 231–235 (2023).
50. A. Goffin, J. Griff-McMahon, I. Larkin, and H. M. Milchberg, "Atmospheric Aerosol Clearing by Femtosecond Filaments," Phys. Rev. Applied **18**, 014017 (2022).
51. L. de la Cruz, E. Schubert, D. Mongin, S. Klingebiel, M. Schultze, T. Metzger, K. Michel, J. Kasparian, and J.-P. Wolf, "High repetition rate ultrashort laser cuts a path through fog," Applied Physics Letters **109**, 251105 (2016).
52. G. Schimmel, T. Produit, D. Mongin, J. Kasparian, and J.-P. Wolf, "Free space laser telecommunication through fog," Optica **5**, 1338 (2018).
53. I. Larkin, J. Griff-McMahon, A. Schweinsberg, A. Goffin, A. Valenzuela, and H. M. Milchberg, "Full path single-shot imaging of femtosecond pulse collapse in air turbulence," Optics Letters **45**, 2518 (2020).
54. N. Jhajj, E. W. Rosenthal, R. Birnbaum, J. K. Wahlstrand, and H. M. Milchberg, "Demonstration of Long-Lived High-Power Optical Waveguides in Air," Physical Review X **4**, (2014).
55. A. Goffin, I. Larkin, A. Tartaro, A. Schweinsberg, A. Valenzuela, E. W. Rosenthal, and H. M. Milchberg, "Optical Guiding in 50-Meter-Scale Air Waveguides," Phys. Rev. X **13**, 011006 (2023).
56. A. Goffin, A. Tartaro, and H. M. Milchberg, "Quasi-steady-state air waveguide," Optica **10**, 505 (2023).
57. Y.-H. Cheng, J. K. Wahlstrand, N. Jhajj, and H. M. Milchberg, "The effect of long timescale gas dynamics on femtosecond filamentation," Optics Express **21**, (2013).
58. J. Isaacs, B. Hafizi, L. A. Johnson, E. W. Rosenthal, L. Mrini, and J. Peñano, "Modeling the propagation of a high-average-power train of ultrashort laser pulses," Opt. Express **30**, 22306 (2022).
59. F. Vidal and T. W. Johnston, "Electromagnetic Beam Breakup: Multiple Filaments, Single Beam Equilibria, and Radiation," Phys. Rev. Lett. **77**, 1282–1285 (1996).
60. M. Mlejnek, M. Kolesik, J. V. Moloney, and E. M. Wright, "Optically Turbulent Femtosecond Light Guide in Air," Physical Review Letters **83**, 2938–2941 (1999).
61. A. J. Campillo, S. L. Shapiro, and B. R. Suydam, "Relationship of self-focusing to spatial instability modes," Applied Physics Letters **24**, 178–180 (1974).
62. A. J. Campillo, S. L. Shapiro, and B. R. Suydam, "Periodic breakup of optical beams due to self-focusing," Applied Physics Letters **23**, 628–630 (1973).
63. E. Mitina, D. Uryupina, N. Zhidovtsev, R. Volkov, O. Kosareva, and A. Savel'ev, "Long-range robust multifilament arrays from terawatt femtosecond beam," Laser Phys. Lett. **19**, 015201 (2022).
64. D. Pushkarev, D. Shipilo, A. Lar'kin, E. Mitina, N. Panov, D. Uryupina, A. Ushakov, R. Volkov, S. Karpeev, S. Khonina, O. Kosareva, and A. Savel'ev, "Effect of phase front modulation on the merging of multiple regularized femtosecond filaments," Laser Physics Letters **15**, 045402 (2018).

65. A. Vinçotte and L. Bergé, "Femtosecond Optical Vortices in Air," Physical Review Letters **95**, (2005).
66. L. T. Vuong, T. D. Grow, A. Ishaaya, A. L. Gaeta, G. W. 't Hooft, E. R. Eliel, and G. Fibich, "Collapse of Optical Vortices," Physical Review Letters **96**, (2006).
67. Miroslav Kolesik and Jerome V Moloney, "Nonlinear optical pulse propagation simulation: from Maxwell's to unidirectional equations.," Physical Review E (2004).
68. J. V. Moloney, M. Kolesik, M. Mlejnek, and E. M. Wright, "Femtosecond self-guided atmospheric light strings," Chaos: An Interdisciplinary Journal of Nonlinear Science **10**, 559–569 (2000).
69. S. Tzortzakis, L. Bergé, A. Couairon, M. Franco, B. Prade, and A. Mysyrowicz, "Breakup and Fusion of Self-Guided Femtosecond Light Pulses in Air," Phys. Rev. Lett. **86**, 5470–5473 (2001).
70. R. Piessens, "The Hankel Transform," in *The Transforms and Applications Handbook* (CRC Press, 2000).
71. A. Couairon, "Filamentation length of powerful laser pulses," Applied Physics B **76**, 789–792 (2003).
72. A. A. Ionin, L. V. Seleznev, and E. S. Sunchugasheva, "Formation of plasma channels in air under filamentation of focused ultrashort laser pulses," Laser Physics **25**, 033001 (2015).
73. J. Kawanaka, K. Yamakawa, H. Nishioka, and K. Ueda, "30-mJ, diode-pumped, chirped-pulse Yb:YLF regenerative amplifier," Opt. Lett. **28**, 2121 (2003).
74. M. Pergament, M. Kellert, U. Demirbas, J. Thesinga, S. Reuter, Y. Liu, Y. Hua, M. Kilinc, A. Yakovlev, and F. X. Kärtner, "100-mJ, 100-W cryogenically cooled Yb:YLF laser," Opt. Lett. **48**, 2833 (2023).
75. A. Higginson, Y. Wang, H. Chi, A. Goffin, I. Larkin, H. M. Milchberg, and J. J. Rocca, "Wake dynamics of air filaments generated by high-energy picosecond laser pulses at 1 kHz repetition rate," Opt. Lett. **46**, 5449 (2021).
76. B. Shang, P. Qi, J. Guo, Z. Zhang, L. Guo, C. Chu, J. Liu, O. G. Kosareva, N. Zhang, L. Lin, and W. Liu, "Manipulation of Long-Distance femtosecond laser Filamentation: From physical model to acoustic diagnosis," Optics & Laser Technology **157**, 108636 (2023).
77. J. K. Wahlstrand, Y.-H. Cheng, and H. M. Milchberg, "Absolute measurement of the transient optical nonlinearity in N2 , O2 , N2O, and Ar," Phys. Rev. A **85**, 043820 (2012).
78. G. Fibich and A. L. Gaeta, "Critical power for self-focusing in bulk media and in hollow waveguides," Opt. Lett. **25**, 335 (2000).
79. A. Ting, D. F. Gordon, E. Briscoe, J. R. Peñano, and P. Sprangle, "Direct characterization of self-guided femtosecond laser filaments in air," Applied Optics **44**, 1474 (2005).
80. I. Alexeev, A. Ting, D. F. Gordon, E. Briscoe, J. R. Penano, R. F. Hubbard, and P. Sprangle, "Longitudinal compression of short laser pulses in air," Applied Physics Letters **84**, 4080–4082 (2004).

81. M. Nurhuda and E. van Groesen, "Effects of delayed Kerr nonlinearity and ionization on the filamentary ultrashort laser pulses in air," Phys. Rev. E **71**, 066502 (2005).
82. M. C. Schroeder, I. Larkin, T. Produit, E. W. Rosenthal, H. Milchberg, and J.-P. Wolf, "Molecular quantum wakes for clearing fog," Optics Express **28**, 11463 (2020).
83. P. Sprangle, J. Peñano, and B. Hafizi, "Optimum Wavelength and Power for Efficient Laser Propagation in Various Atmospheric Environments," Journal of Directed Energy **2**, (2006).
84. B. A. Kunkel, "Fog Drop-Size Distributions Measured with a Laser Hologram Camera," Journal of Applied Meteorology **10**, 482–486 (1971).
85. National Aeronautics and Space Administration, "Progress of NASA research on warm fog properties and modification concepts," in (1969).
86. A. Rudenko, P. Rosenow, V. Hasson, and J. V. Moloney, "Plasma-free water droplet shattering by long-wave infrared ultrashort pulses for efficient fog clearing," Optica **7**, 115 (2020).
87. C. Zhang, M. Tang, H. Zhang, and J. Lu, "Optical breakdown during femtosecond laser propagation in water cloud," Optics Express **27**, 8456 (2019).
88. D. Woodbury, A. Goffin, R. M. Schwartz, J. Isaacs, and H. M. Milchberg, "Self-Guiding of Long-Wave Infrared Laser Pulses Mediated by Avalanche Ionization," Physical Review Letters **125**, (2020).
89. J. Noack and A. Vogel, "Laser-induced plasma formation in water at nanosecond to femtosecond time scales: calculation of thresholds, absorption coefficients, and energy density," IEEE J. Quantum Electron. **35**, 1156–1167 (1999).
90. G. S. K. Wong and T. F. W. Embleton, "Variation of specific heats and of specific heat ratio in air with humidity," The Journal of the Acoustical Society of America **76**, 555–559 (1984).
91. F. E. Jones, "The air density equation and the transfer of the mass unit," Journal of Research of the National Bureau of Standards **83**, 419–428 (1978).
92. P. E. Ciddor, "Refractive index of air: new equations for the visible and near infrared," Appl. Opt. **35**, 1566 (1996).
93. E. F. Toro, "High–Order and TVD Methods for Scalar Equations," in *Riemann Solvers and Numerical Methods for Fluid Dynamics: A Practical Introduction*, E. F. Toro, ed. (Springer, 2009), pp. 413–492.
94. B. R. Munson, D. F. Young, T. H. Okiishi, and W. W. Huebsch, *Fundamentals of Fluid Mechanics* (Wiley, 2009).
95. S. R. Gonzalez Avila and C.-D. Ohl, "Fragmentation of acoustically levitating droplets by laser-induced cavitation bubbles," Journal of Fluid Mechanics **805**, 551–576 (2016).
96. S. Tochitsky, E. Welch, M. Polyanskiy, I. Pogorelsky, P. Panagiotopoulos, M. Kolesik, E. M. Wright, S. W. Koch, J. V. Moloney, J. Pigeon, and C. Joshi, "Megafilament in air formed by self-guided terawatt long-wavelength infrared laser," Nature Photonics **13**, 41–46 (2019).

97. C. Jeon, D. Harper, K. Lim, M. Durand, M. Chini, M. Baudelet, and M. Richardson, "Interaction of a single laser filament with a single water droplet," Journal of Optics **17**, 055502 (2015).
98. P. Polynkin, C. Ament, and J. V. Moloney, "Self-Focusing of Ultraintense Femtosecond Optical Vortices in Air," Physical Review Letters **111**, (2013).
99. D. V. Pushkarev, A. S. Lar'kin, E. V. Mitina, N. A. Zhidovtsev, D. S. Uryupina, R. V. Volkov, S. V. Karpeev, S. N. Khonina, A. A. Karabutov, Yu. E. Geints, O. G. Kosareva, and A. B. Savel'ev, "Robust multifilament arrays in air by Dammann grating," Opt. Express **29**, 34189 (2021).
100. G. Fibich and N. Gavish, "Critical power of collapsing vortices," Phys. Rev. A **77**, 045803 (2008).
101. A. W. Snyder and J. D. Love, *Optical Waveguide Theory* (Chapman and Hall, 1991).
102. L. Feder, B. Miao, J. E. Shrock, A. Goffin, and H. M. Milchberg, "Self-waveguiding of relativistic laser pulses in neutral gas channels," Phys. Rev. Research **2**, 043173 (2020).
103. J. K. Wahlstrand, Y.-H. Cheng, and H. M. Milchberg, "High Field Optical Nonlinearity and the Kramers-Kronig Relations," Physical Review Letters **109**, (2012).
104. C. Ament, L. Johnson, A. Schmitt-Sody, A. Lucero, T. Milster, and P. Polynkin, "Generation of multiterawatt vortex laser beams," Appl. Opt. **53**, 3355 (2014).
105. Y.-H. Chen, S. Varma, T. M. Antonsen, and H. M. Milchberg, "Direct Measurement of the Electron Density of Extended Femtosecond Laser Pulse-Induced Filaments," Phys. Rev. Lett. **105**, 215005 (2010).
106. M. D. Feit and J. A. Fleck, "Light propagation in graded-index optical fibers," Appl. Opt. **17**, 3990 (1978).
107. E. W. Rosenthal, N. Jhajj, J. K. Wahlstrand, and H. M. Milchberg, "Collection of remote optical signals by air waveguides," Optica **1**, 5 (2014).
108. N. Jhajj, Y.-H. Cheng, J. K. Wahlstrand, and H. M. Milchberg, "Optical beam dynamics in a gas repetitively heated by femtosecond filaments," Opt. Express **21**, 28980 (2013).
109. Y. Wang, K. Dehne, A. Higginson, H. Chi, V. Chvykov, A. Davenport, C. S. Menoni, and J. J. Rocca, "Advances in ultrafast kilowatt average power cryogenically cooled Yb:YAG lasers and applications at Colorado State University," in *Ultrafast Optics 2023 - UFOXIII* (Optica Publishing Group, 2023), p. Tu2.2.
110. C. Herkommer, P. Krötz, R. Jung, S. Klingebiel, C. Wandt, R. Bessing, P. Walch, T. Produit, K. Michel, D. Bauer, R. Kienberger, and T. Metzger, "Ultrafast thin-disk multipass amplifier with 720 mJ operating at kilohertz repetition rate for applications in atmospheric research," Opt. Express **28**, 30164 (2020).
111. R. Jung, J. Tümmler, T. Nubbemeyer, and I. Will, "Two-Channel Thin-Disk Laser for High Pulse Energy," in *Advanced Solid State Lasers* (OSA, 2015), p. AW3A.7.

112. M. Duda, O. Novák, M. Chyla, M. Smrž, and T. Mocek, "Balancing the conversion efficiency and beam quality of second harmonic generation of a two-picosecond Yb:YAG thin-disk laser," Laser Phys. **30**, 025405 (2020).
113. V. I. Tatarskii, *The Effects of Turbulent Atmosphere on Wave Propagation* (National Technical Information Service, US Department of Commerce, 1971).
114. S. L. Chin, A. Talebpour, J. Yang, S. Petit, V. P. Kandidov, O. G. Kosareva, and M. P. Tamarov, "Filamentation of femtosecond laser pulses in turbulent air," Appl Phys B **74**, 67–76 (2002).
115. E. P. Silaeva, S. A. Shlenov, and V. P. Kandidov, "Multifilamentation of high-power femtosecond laser pulse in turbulent atmosphere with aerosol," Applied Physics B **101**, 393–401 (2010).